TRIUMF

Document-109442

Design Note TRI-DN-14-06
ARIEL High Resolution Separator

Document Type: **Design Note**

Release: **3** **Release Date:** **2015/07/07**

Author(s): **Jim A. Maloney**
Marco Marchetto

	Name:	Signature:	Date:
Author:	Jim A. Maloney	APPROVED	6/16/2015
Author:	Marco Marchetto		June 16, 2015
Author:	Rick Baartman	APPROVED	
Reviewed By:	George Clark		June 17, 2015
Reviewed By:	Thomas Planche	APPROVED	2015/06/19
Approved By:	Reiner Kruecken	APPROVED	2015-06-19

Note: Before using a copy (electronic or printed) of this document you must ensure that your copy is identical to the released document, which is stored on TRIUMF's document server.

History of Changes

Release Number	Date	Description of Changes	Author(s)
#1	2014-04-29	Initial Release	J.A. Maloney & Marco Marchetto
#2	2015-04-13	Update for final design review	J.A. Maloney & Marco Marchetto
#3	2015-07-07	Updated paragraph 9.9 with new curvature. Add paragraph 10 with engineering features	J.A. Maloney & Marco Marchetto

Keywords:

ARIEL, ARIEL-II, P0310, CANREB, Design Note, Design, Beam Dynamics, Separator, Spectrometer, HRS, High Resolution.

Distribution list:

Friedhelm Ames

Erig Guetre

Asita Perera

CONFIDENTIAL

Contents

CONFIDENTIAL

1 Abstract

This design note will set out the optical layout of the CANREB HRS Mass Spectrometer and element design for the dipole magnets and electrostatic elements in the system.

2 Introduction

2.1 Purpose

The purpose of this design note is to provide basic information detailing the design and functioning of the CANREB HRS and its component elements. This detail will serve as a basis for future manufacturing specification concerning the HRS magnets and correctors, construction of the HRS itself, and the intended operation of the HRS.

2.2 Scope

The scope of this design note is to identify and specify the characteristics of the CANREB HRS and its constituent elements.

Release 1 will present conceptual design of higher order corrections for the HRS optical layout and optimization of magnetic fields inside magnet (edge to edge and within the poles)

Optimization of the fringe field regions from magnetic view will be addressed in Release 2

Release 2 will present the basic optical layout and overview of the electrostatic elements of the HRS. An optimized design for electrostatic elements will be addressed in a separate design note.

2.3 Definitions and Abbreviations

The CANREB HRS is defined by all optical components from and including the entrance (object) slit and the exit (image) slit.

The following acronyms are used in this note:

1. HRS: High resolution spectrometer (or separator)
2. COSY: Beam simulation code COSY Infinity Version 9.1 updated January 2013 [1].

CONFIDENTIAL

3 Optical Layout Considerations

Several potential first order layouts for the HRS were initially considered, including several first order layouts discussed in TRIUMF Design Note TRI-DN-13-07, TRIUMF Document-74265 [2]. The overriding goals of the HRS design are to provide consistent and maintainable beams at the required resolution. This is assessed by several considerations:

1) The resolution achievable by the HRS for the specified beam
2) The stability of the beam (i.e., how long can performance at the desired resolution be maintained
3) The rate of transmission (i.e., how much of the potential beam in lost in the HRS)
4) The ease of operation (i.e., can a desired beam be tuned in a reasonable time frame)

The particular requirements have been set out in TRIUMF Document-74319 [3].

4 Optical Layout Studies

To develop the more flexible design, it is helpful to understand certain intrinsic limitations of a mass separator like the one being developed for ARIEL.

Mass separation is generated by creating dispersion using bending elements in the separator. Greater dispersion yields greater separation for isotopes with the same net charge but different mass. Dispersion is a function of the bending radius and angle of the dipoles in the separator. The ARIEL HRS will use 2 magnetic dipoles, discussed subsequently in this note, with a bending radius of 1.2 m and a bending angle of 90 degrees. The spacing between the dipole is fixed at 1.6 m. This system results in dispersion of approximately 2.4 m. Multiplying the fractional difference in mass for a particle from some reference mass ($\text{Mass-Mass}_{ref}/\text{Mass}_{ref}$) by 2.4 m will indicate the horizontal shift for that particle at the exit to the HRS relative to a particle with the reference mass. (i.e., a particle with a fractional difference of 1/20000 would shift its horizontal position due to dispersion by approximately 120 μm from the final position of a particle with the reference mass). Resolving power for the HRS specifies the inverse of the fraction mass difference than can be separated.

$$\text{Resolving Power} = \text{Mass}/\Delta\text{Mass}$$

The dispersion (D) and resolving power (R) for a separator determine the maximum slit (2s) width that can be used to limit the incoming horizontal beam size to the separator. Slits at the entrance and exit of the separator are used to collimate the beam and select the desired mass, excluding contaminants with slightly different masses.

$$\text{Full slit width} \leq \text{Dispersion/Resolving Power} \qquad (2s = D/R)$$

CONFIDENTIAL

Resolution, however, cannot be considered in isolation. Limiting the slit width used for the incoming beam will increase resolution, but this has the drawback of cutting off a greater portion of the beam, and reducing the scientific usefulness of the separator. For this reason, any reference to a separator's resolution should always specify the accepted beam emittance. The beam's emittance (ε) is defined as the product of the initial half width of the beam (s) and its maximum angular deviation (θ_i).

For example, for a separator with 2.4 m of dispersion and a resolving power target of 20,000, the full width of the initial slit is limited to no greater than 120 μm. This would accept an initial beam with a 60 μm half-width. This beam size and an angular deviation of up to +/- 50 mrads would constitute an emittance of 3 pi μm.

A pure separator can be simulated using the known parameters of the HRS. Placing a drift of 0.8 m meters outside of each dipole, the angle of the entrance and exit edges for each dipole is adjusted to achieve imaging in the horizontal plane. To maximize symmetry within the separator, the same edge angle is used for the entrance and exit edges of both dipoles. The fit criterion achieves point to point/parallel to parallel focusing in horizontal phase space by minimization of the sum of the squares of the (x|a) and (a|x) coefficients in the transfer matrix from the beginning to the end of the system. An electrostatic multipole was placed in the center of the separator, but not used for the first order fit. It will be used for correcting aberrations at second order and higher. This model was generated using COSY's DI magnetic bending element (a homogeneous dipole which allows for parameterization of the angles and curvature of the dipole's entrance and exit edges) and FR 2 modeling of the dipole fringe fields. Figure 1 shows the horizontal motion of particles in this pure separator.

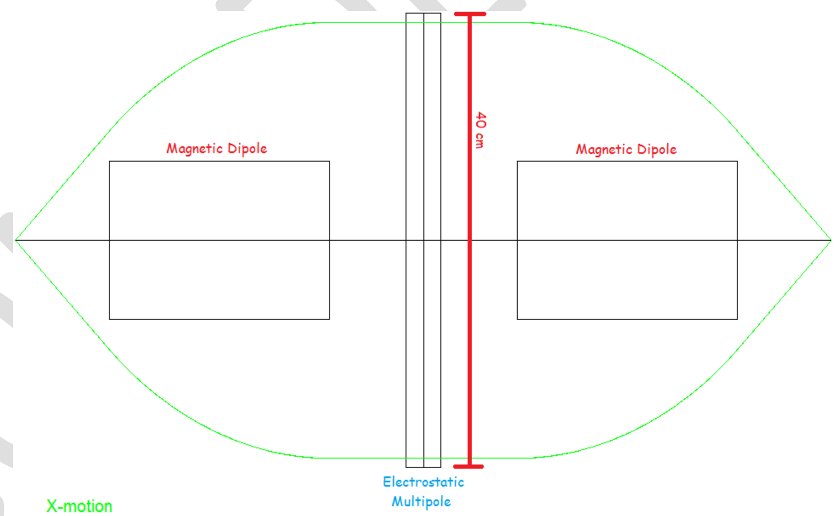

Figure 1: First order horizontal ray trace for the pure separator design using COSY.

The first order transfer matrix for the pure separator design generated from a COSY simulation with an edge angle of approximately 26.5 degrees is given in Table 1. COSY defines a particle using 6 coordinates (x, a, y, b, t, d). X and y represent the difference (in meters) in horizontal and vertical position transverse to the beam's reference trajectory. The particle's angle is expressed using the coordinates a (p_x/p_{ref}) in the horizontal and b (p_y/p_{ref}) in the vertical plane. The other 2 coordinates are canonical conjugates to z and p_z; t is based on a scaled path length variation from the reference trajectory, and d if the fractional difference in kinetic energy from the reference particle ($K - K_{ref}/K_{ref}$). The transfer map represents the change in a particle's final coordinates (r_{final}) at the end of the system as a function of the particle's initial coordinates ($r_{initial}$). In the linear case, the transfer map can be represented as a 6 x 6 matrix (M).

$$r_{final} = M \cdot r_{initial}$$

As an example, using the 2x2 portion of the transfer matrix representing horizontal phase space and the evolution of the final horizontal coordinates based on their initial values, the transfer map lets us express the final horizontal position (x_{final}) as a function of a particle's initial horizontal phase space coordinates ($x_{initial}, a_{initial}$).

$$\begin{matrix} x_{final} \\ a_{final} \end{matrix} = \begin{Bmatrix} x|x & x|a \\ a|x & a|a \end{Bmatrix} \cdot \begin{matrix} x_{initial} \\ a_{initial} \end{matrix}$$

$$x_{final} = (x|x)x_{initial} + (x|a)a_{initial}$$

The nonlinear effects on the beam can similarly be expressed as a function of initial particle coordinates through a Taylor series (N) which can be truncated at a given order.

$$r_{final} = M \cdot r_{initial} + N(r_{initial})$$

For instance, we can add the second order nonlinear terms from this Taylor series based on the initial horizontal coordinates to our previous example:

$$x_{final} = (x|x)x_{initial} + (x|a)a_{initial} + (x|xx){x_{initial}}^2 + (x|xa)x_{initial}a_{initial} + (x|aa){a_{initial}}^2$$

COSY calculates and outputs the coefficients for both the linear matrix and nonlinear map ordered by column. The first column in Table 1 represents the coefficients that effect x_{final}. The other columns give the coefficients for a_{final}, y_{final}, b_{final} and t_{final}. No column is included for d_{final} since this all coefficients are zero or one if energy is conserved. The rightmost column show which of the 6 initial parameters relates to that row's coefficients. In the first row (100000) are coefficients based on the first power of $x_{initial}$.

Table 1: COSY Linear Transfer Map for the Pure Separator Design

-1.000000	0.2246896E-09	0.0000000E+00	0.0000000E+00	-0.4957264E-07	100000
-0.2740520E-09	-1.000000	0.0000000E+00	0.0000000E+00	-2.399095	010000
0.0000000E+00	0.0000000E+00	-0.9554200	0.1484753	0.0000000E+00	001000
0.0000000E+00	0.0000000E+00	-0.5871196	-0.9554198	0.0000000E+00	000100
0.0000000E+00	0.0000000E+00	0.0000000E+00	0.0000000E+00	1.000000	000010
2.399095	-0.5011170E-07	0.0000000E+00	0.0000000E+00	-0.4000196	000001

CONFIDENTIAL

This model, as previously noted, includes a dipole edge angle and a model of the fringe field outside the magnets and has a dispersion coefficient of 2.399095 meters. To study to geometric limitations on acceptance for these dipoles, the largest nonlinearities in the beam up to 3rd order were corrected by introducing a curvature to the entrance and exit edges of the dipole magnets and powering the sextupole and octupole modes of the multipole. Other nonlinearities up to 8th order were included in the simulation and left uncorrected. The resulting transfer map from COSY was used to generate the final phase space plots, show in Figure 2(a) and (b), for an ensemble of particles with a wide range of initial horizontal angular deviation from the reference trajectory (all other coordinates were held constant within the ensemble). This study demonstrates the geometric limitations on angular acceptance within the HRS.

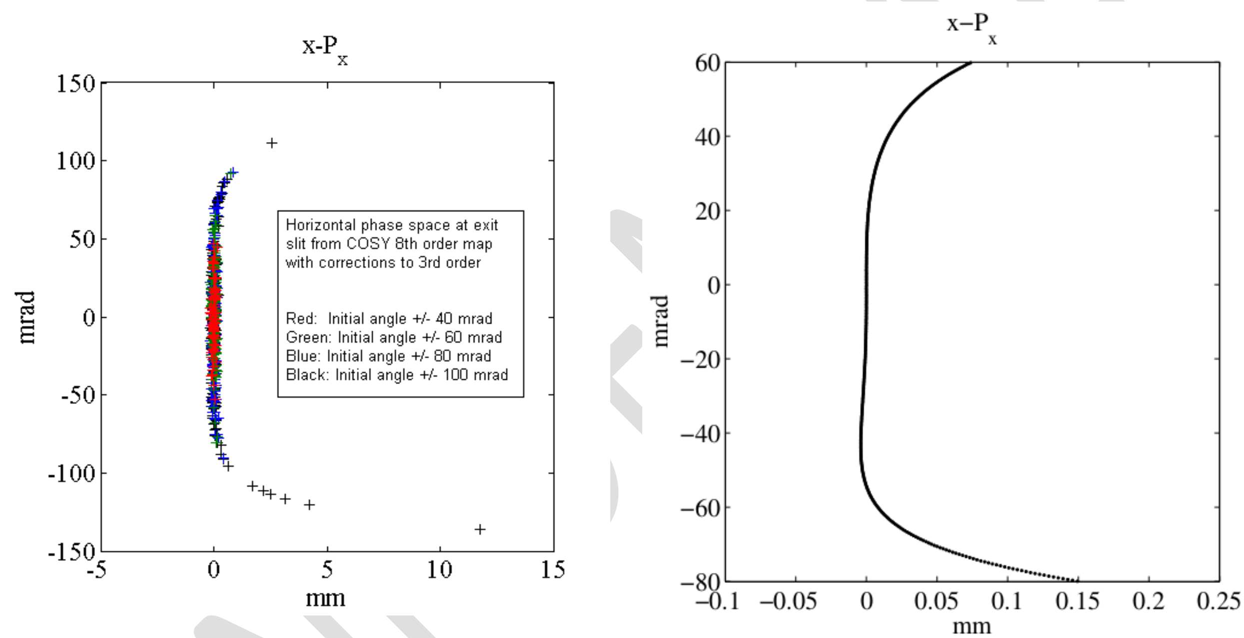

Figure 2 (a) and (b): Angular acceptance for the pure separator HRS model: (a) the final phase space for several distributions of particles is plotted at the exit slit, and the display is color-coded to represent the initial angular spread of the distribution; and (b) zoom in for angular deviation from +60 mrad to -80 mrad.

As shown, particles with an initial angle greater than 80 mrad will not be useful since their final horizontal position would shift by more than the maximum slit aperture. For high resolution, where the slit aperture is less than +/- 0.12 mm from reference, angular acceptance is reduced to < 60 mrad. Knowing the maximum angular acceptance also allow us to determine the minimum slit size needed to contain a desired emittance. If angular acceptance is limited to initial angles of +/- 60 mrad from reference, then a full width slit of at least 100 μm is needed for a 3 pi μm emittance.

The horizontal envelope of the beam within the HRS is set primarily by particles with the largest initial angles. Figure 3 was generated with TRANSOPTR, and shows the envelope for a beam of particles with an initial angular deviation of up to 80 mrad. The maximum horizontal envelope is approximately +/- 160 mm from the reference trajectory. Calculations of the beam envelopes for the target mass are detailed in

CONFIDENTIAL

Appendix L for a beam with 3 µm horizontal emittance (+/- .05 mm x 60 mrad) and 6 µm vertical emittance (+/- 2 mm x 3 mrad). The reduced angular spread coupled with shorter drifts in the HRS optical design vs. the pure separator simulated in Figure 3, reduce the envelope for the target mass by about 28%.

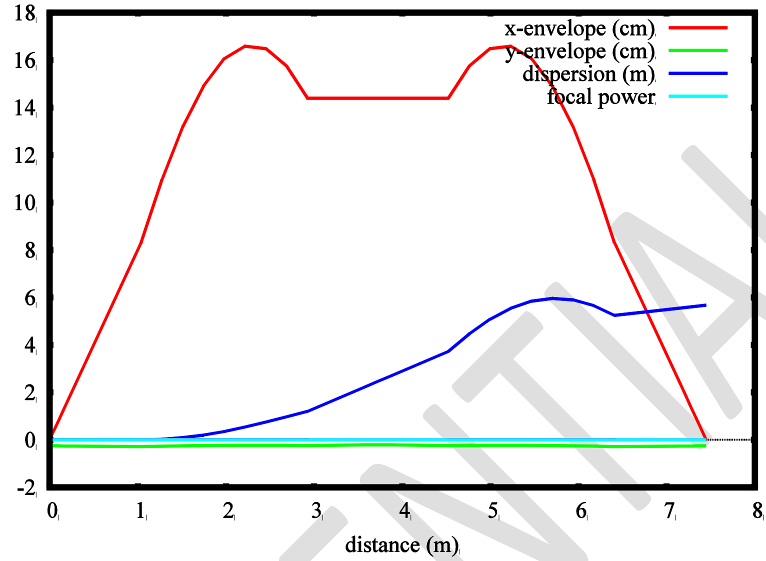

Figure 3: TRANSOPTR plot for the beam envelopes slit to slit for the pure HRS separator. The dispersion is also plotted as a function of momentum (twice mass based dispersion).

For a beam with no energy spread and a 3 pi µm emittance, the resulting horizontal phase space at the exit for the pure separator is shown in Figure 4(a) for a beam half width of 37.5 µm and angular spread of +/- 80 mrad, and in Figure 4(b) for a beam half width of 50 µm and angular spread of +/- 60 mrad. In the former case, collimation of the beam would be requires for separation due to the tails created at large angles. This would result in some loss of transmission to obtain the desired resolution.

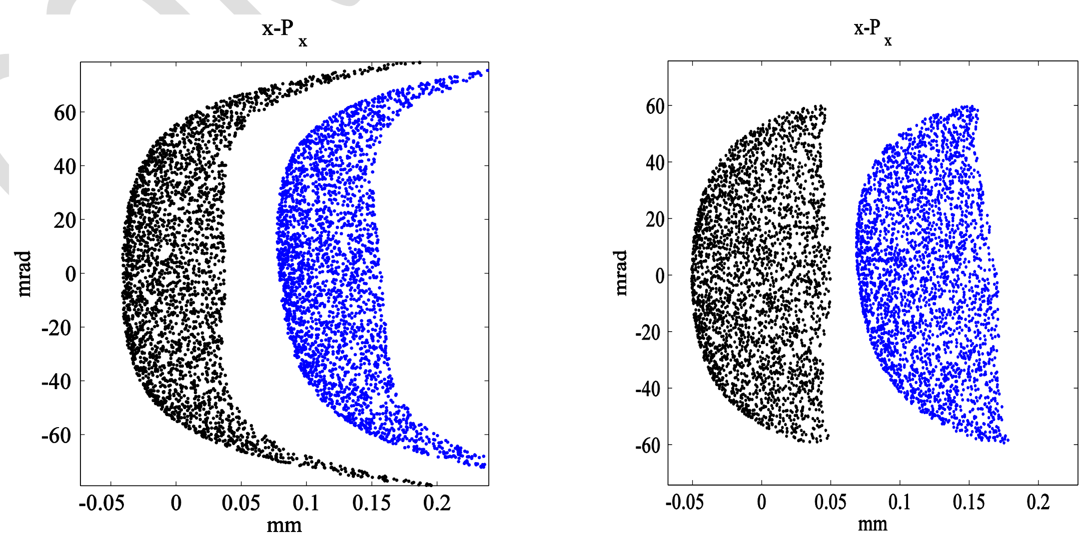

CONFIDENTIAL

Figure 4 (a) and (b): Final phase space for two masses differing by 1/20000 at exit slit for pure HRS separator with a horizontal emittance of 3 pi µm and an initial angular deviation of up to (a) +/- 80 mrad, and (b) +/- 60 mrad.

Achieving resolution of 20,000 for a transmitted beam with a 3 pi µm emittance and an initial horizontal angular spread of up to +/- 60 mrad requires 100 µm full aperture entrance and exit slits. This, however, does not include the effects of either energy spread in the beam or higher order aberrations in the HRS. If the energy in the beam varies by up to 1 eV (σ_E= .25), the effect on separation for a beam with 3 pi µm emittance and an initial horizontal angular spread of up to +/- 60 mrads is shown in Figure 5(a). Even in this case, clean mass resolution would require cutting some additional part of the beam with the slit aperture. For example, in Figure 5(b) a clean 20000 resolution is achieved by reducing the initial horizontal aperture by half. This reduces the transmitted emittance to 1.5 pi mm.

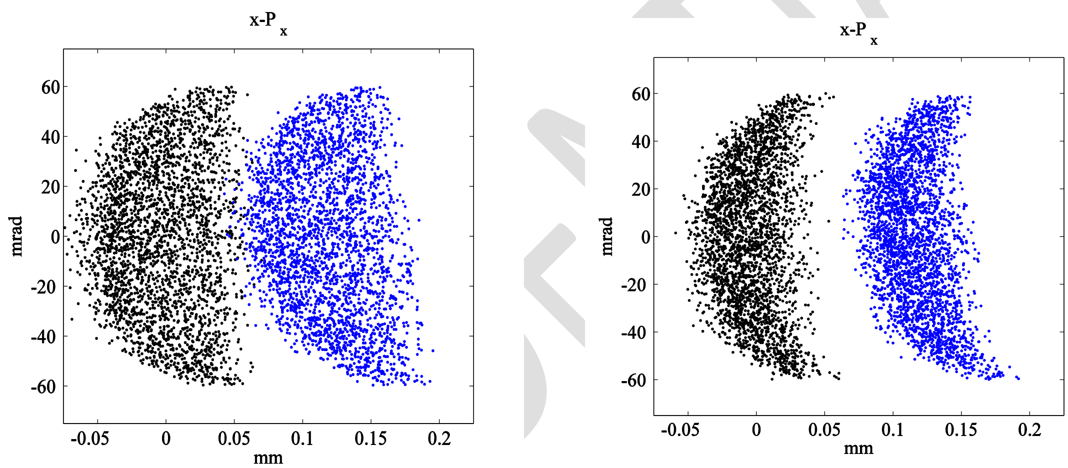

Figure 5 (a) and (b): Final phase space for two masses differing by 1/20000 at exit slit for pure HRS separator with an initial angular deviation of up to +/- 60 mrad and ΔE of 1 eV and a horizontal emittance of (a) 3 pi µm and (b) 1.5 pi µm.

The ARIEL HRS requirements designate an energy spread (ΔE) of 1 eV (σ_E= .25). For this beam the resolution requirement is 20000 for a 3 pi µm horizontal emittance, and 10000 for a 6 pi µm horizontal emittance. In both cases, the vertical emittance would be designed to accept up to 6 pi µm. These specifications assume a hard cut for energies above and below this limit. For actual beams, the distribution will have some tail contaminating nearby masses after separation.

The relationship between beam energy spread and resolution can also be analytically understood. Final horizontal offset in position of a particle relative to the reference particle can be determined in the linear approximation from the transfer matrix and the particle's initial coordinates (x_i a_i y_i b_i t_i d_i) using the equation:

$$x_f = (x|x)x_i + (x|a)a_i + (x|d)d_i$$

CONFIDENTIAL

where d_i will be variation from reference in kinetic energy ($K\text{-}K_{ref}/K_{ref}$) and/or mass variation ($M\text{-}M_{ref}/M_{ref}$). From our imaging criteria, the equation simplifies to:

$$x_f = x_i + (x|d)\ [(M\text{-}M_{ref}/M_{ref}) + (K\text{-}K_{ref}/K_{ref})]$$

For our HRS design specifications, the parameters for the ranges in mass and energy are

$$K\text{-}\ K_{ref} = \Delta K = 1\ \text{eV}, \quad K_{ref} = 60\ \text{keV}, \quad (M\text{-}M_{ref}/M_{ref}) = 1/20000$$

Assuming a static distribution in particles at the entrance slit with full width of Δx, the condition for separation in the linear model can be approximated as:

$$(x|\delta)\ [(M\text{-}M_{ref}/M_{ref}) - (K\text{-}K_{ref}/K_{ref})] > \Delta x$$

An alternative way to consider the same relationship is to look at the reduction in designed resolution as a function of changes in the horizontal emittance and energy spread of the input beam. For example, if the HRS were designed to achieve a target resolution of 20,000 for a beam with horizontal emittance of 3 μm and energy spread of 1 eV, then the effective resolution will change for a different input emittance and energy spread based on approximately this relationship:

$$R_{effective} = \frac{20000}{\frac{\epsilon_x}{3.75\ \mu m} + \frac{\Delta E}{3\ eV}} = \frac{20000}{\frac{\epsilon_x}{3.75\ \mu m} + \frac{\sigma_E}{0.75\ eV}}$$

Minimizing energy variation within the beam reduces this effect. An alternative tradeoff is to sacrifice transmission for improved resolution. This relation highlights the importance of minimizing energy spread within the beam. A proposed DC RFQ cooler could be added to reduce the emittance of the beam from the source, allowing great transmission within the same emittance range, but at the possible expense of increased energy spread within the beam. In many cases it would be advisable to avoid this increase in energy spread when high resolution is the beam delivery priority.

A study done by Dr. Rick Baartman also identified 3 other types of limitations that must be considered:

- Mechanical Limits – entrance and exit slits are used to collimate the beam to the desired width. There will be a limit on the precision with which this gap can be set. Additionally, the slit will be expected to suffer from erosion after extended periods of operation.
- Electrical Limits – variations in peak to peak voltage on the HV and grounding will affect beam energy.
- Magnetic Limits – variations peak to peak of the magnetic field in the good field region, power supply ripple, and machining tolerance for the steel in the magnets' poles.

CONFIDENTIAL

These limits are primarily set by engineering and cost concerns. Estimating these limits, the effect of resolution for the pure separator is plotted for beam energy spread vs. emittance in Figure 6.

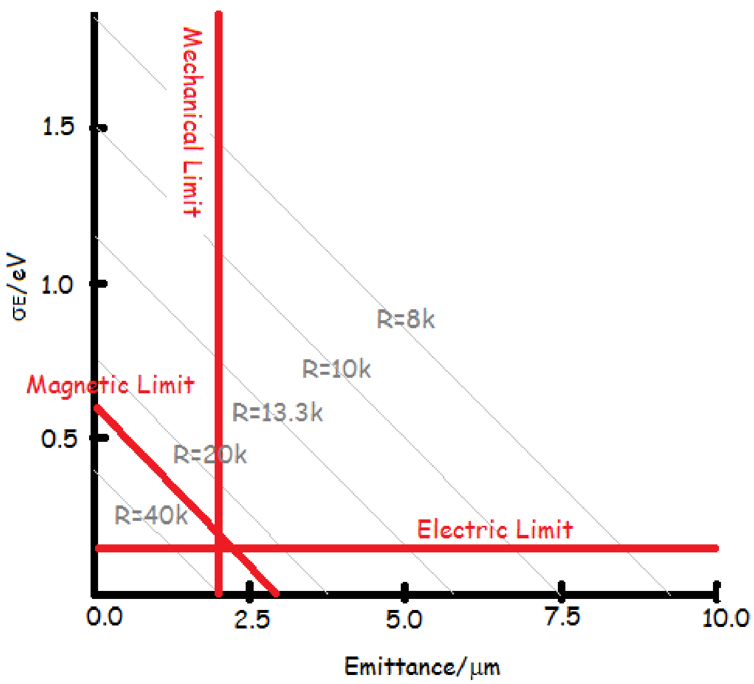

Figure 6: Schematic of the compromises between energy spread and emittance for various separator resolutions.

5 Pole Width Optimization

Studies of the pure separator allowed us to determine the limits of geometric angular acceptance for the magnetic dipoles. This lets us define the slit aperture width for a given horizontal emittance, and track the envelope for a beam of particles within this range of initial positions and angles. This envelope defines the "good field region" where variations in the magnetic field felt by particles need to be minimized to achieve the resolution goals of the HRS.

An additional concern is how wide the poles of these dipole magnets need to be. If the poles are sufficiently wide, particles travelling in the good field region will "feel" a smooth field similar to that of an infinitely wide pole. As the pole width is narrowed, variations in field due to the drop off at the transverse edge of the pole will be felt by particles in the beam. This will result in variations in the local and integrated magnetic field felt by particles travelling through the dipole magnets.

To estimate the effects of varying the transverse pole width, a model, shown in Figure 7, was developed using Mathematica that simulates an inverse tangent drop-off of the scaled magnetic field (B/B_0) as a function of radial distance from the dipole's center of curvature. Figure 8 shows a three dimensional representation of the field near and around the pole (a 2 parameter ENGE function was used for the longitudinal field drop-off).

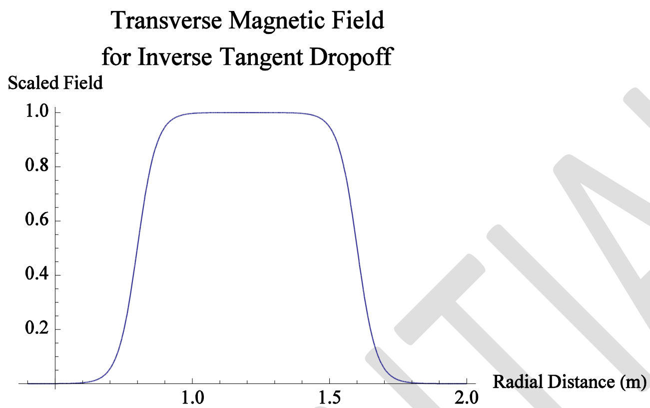

Figure 7: Scaled magnetic field (B/B_0) as a function of radial position from the center of a 1.2 radius of curvature.

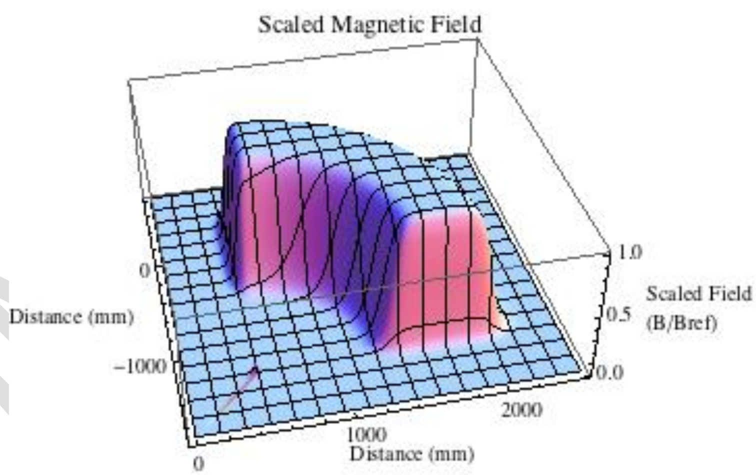

Figure 8: 3D Mathematica model of dipole field falloff near pole edges.

In this model, the transverse scaled magnetic field is determined via the following equation:

$$\frac{B}{B_0} = \frac{1}{\left(1+e^{\left(a_1 - {(w-r_0+r)}/{d}\right)}\right)\left(1+e^{\left(a_1 - {(w+r_0-r)}/{d}\right)}\right)} \tag{2}$$

CONFIDENTIAL

where a_1 scales the dropoff, r_0 is the dipole bending radius, d is the vertical halfgap, w is the halfwidth of the pole, centered along the bending radius, r is the radial coordinate distance from the center of curvature for the dipole. This same methodology was used to model the transverse dropoff in the current OPERA model of the dipole magnet discussed later in this note. This model, shown in Figure 9, required a more complicated 4 coefficient ENGE function to fit the data rather than a simple inverse tangent function.

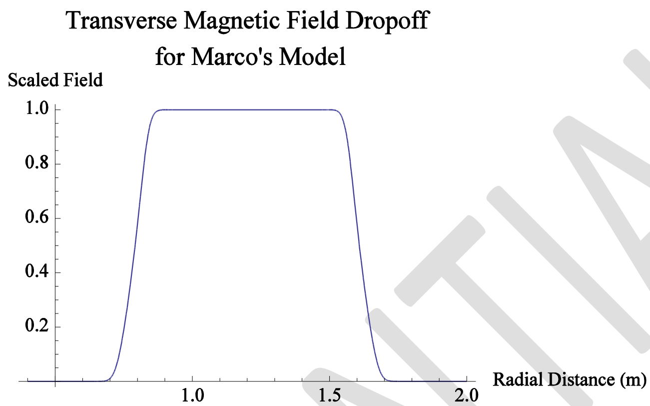

Figure 9: Scaled magnetic field as a function of radial position for Marco's OPERA model of the HRS dipole magnets.

Figure 10 plots the scaled field using the analytic equation at a radial distance of 1.4 m, 20 cm beyond the bending radius, as a function of various pole half-widths. This position was chosen because it lays a few cm beyond the good field region (+/- 16 cm from the reference orbit defined by the bending radius). Naively, one could claim from this plot that reducing the pole half width to approximately 32 cm would be acceptable to maintain 1/20000 field uniformity.

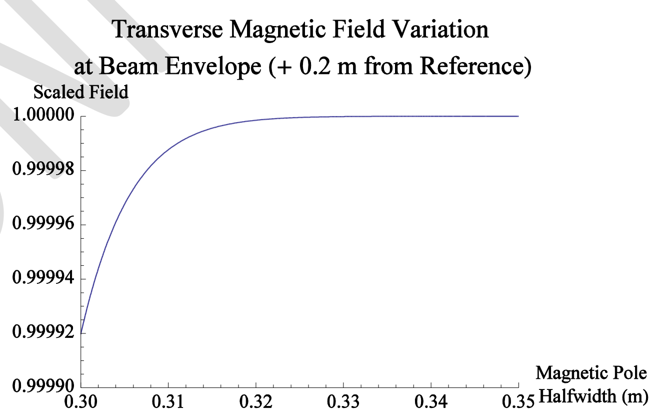

Figure 10: Scaled magnetic field at a radial distance of 1.4 m position from the center of a 1.2 radius of curvature as a function of varying pole half-width.

The field variation, however, includes linear and 2nd order components that will be corrected via shaping of the entrance and exit edges of the magnet poles. Using Mathematica, the exponential parts of the function was expanded using a Taylor series, keeping the terms to 10th order. The difference in scaled field variation due to only the 3rd order and higher terms are plotted in Figure 11.

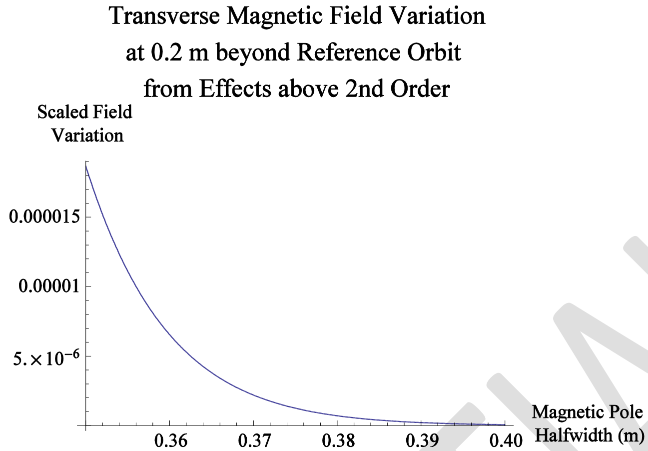

Figure 11: The difference in scaled magnetic field as a function of varying pole half-width due to 3rd order and higher terms.

Thus, the higher order effects (which will be integrated as particles pass through the magnet) appear to have an effect on the order of 1×10^{-5} if the pole half width is reduced beyond approximately 36 cm. This methodology relies on an assumption that the integrated field felt by a particle near the beam envelope will be on a geometric arc along a particular radius from the magnet's center of curvature. Particles will see different effects as they actually follow a more parabolic trajectory, but this model does serve to estimate a minimum pole width needed to minimize these higher order effects from the transverse edges of the poles. There are also nonlinearities due to longitudinal edge shaping of the pole not considered in this mode. This study [4] serves only to provide a coarse estimate of the minimum pole width needed to reduce nonlinearities from the transverse edges of the poles. Additional simulation and testing to study the nonlinear optics has been done using a variety of more sophisticated codes, and is detailed later in this note.

6 General Optical Layout

The HRS layout, depicted below in Figure 13, consists of the following elements:

- Entrance (or object) and exit (or image) slits
- Two 90 degree magnetic dipoles to create mass separation
- Two electrostatic quadrupoles for beam focusing
- An electrostatic multipole corrector to correct beam optical aberrations
- Two diagnostic boxes with additional "waist aperture" slits located between the entrance/exit slits and the magnetic dipoles.

CONFIDENTIAL

In the prior design of the HRS optics, electrostatic quadrupoles were used to shape the phase space between the slits and the magnets. In this model, shown in Figure 12 the 3 pi mm beam at the entrance slit was collimated to a half width of +/- .125 mm with the slit aperture and the horizontal angular deviation was up to +- 24 mrad. The electrostatic quadrupoles also allowed imaging from the entrance to exit slits to be achieved in both the horizontal and vertical plane simultaneously.

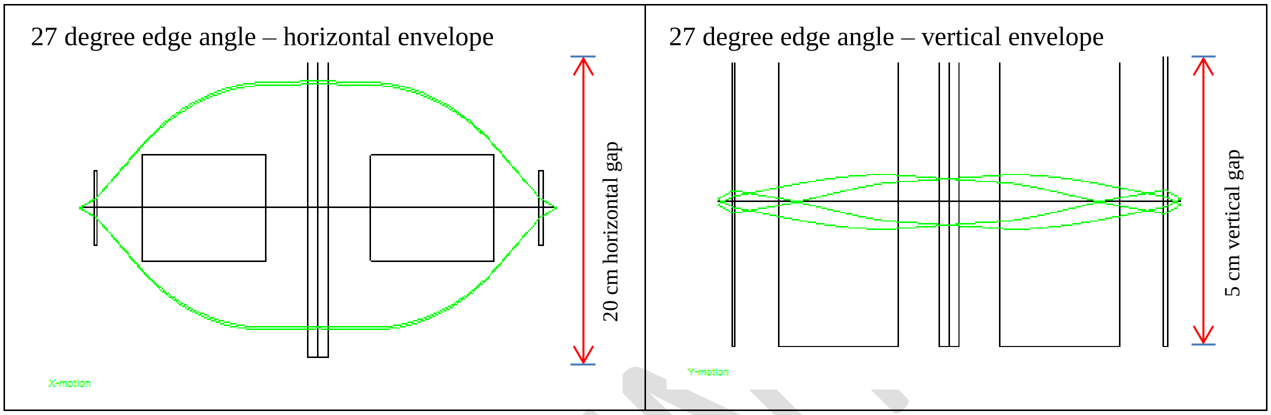

Figure 12: Simulation of beam (a) horizontal and (b) vertical beam motion for HRS fit with 27 degree magnetic dipole entrance and exit edge angle.

The current optical design uses magnification sections (discussed later in this note) to match a beam with much larger horizontal width and smaller angular spread into small waists with conditions similar to pure separator case previously discussed. In the pure separator case, accepting angles up to +/- 60 mrad requires the half width of the entrance and exit slits to be reduced to .05 mm or less. Accurately maintaining such a slit aperture during prolonged experiments is not practical. Instead, matching/magnification sections are used to create waist at these positions. Slit apertures at these waists can then be used as a diagnostic to setup and condition the beam. These "waist aperture slits" are specified to operate from fully closed, and opening in 5 µm steps. During normal operation, these slits would be retracted. Additional diagnostics to measure the beam's emittance and phase space profile could be substituted in at these locations to help with beam setup.

A separate pair of entrance and exit slits would also be located outside the matching/magnification section to collimate the beam in horizontal phase space and select a particular mass resolution at a location where the beam is wider and the angular divergence is reduced. These mass selection slits are specified to be able to maintain a controlled gap size in the range of 50 to 100 µm.

The electrostatic quadrupoles located between the waist aperture slits and the dipole magnets are intended to correct minor 1st order beam focusing errors due, for example, to a slight variation from design in the dipole edge angles.

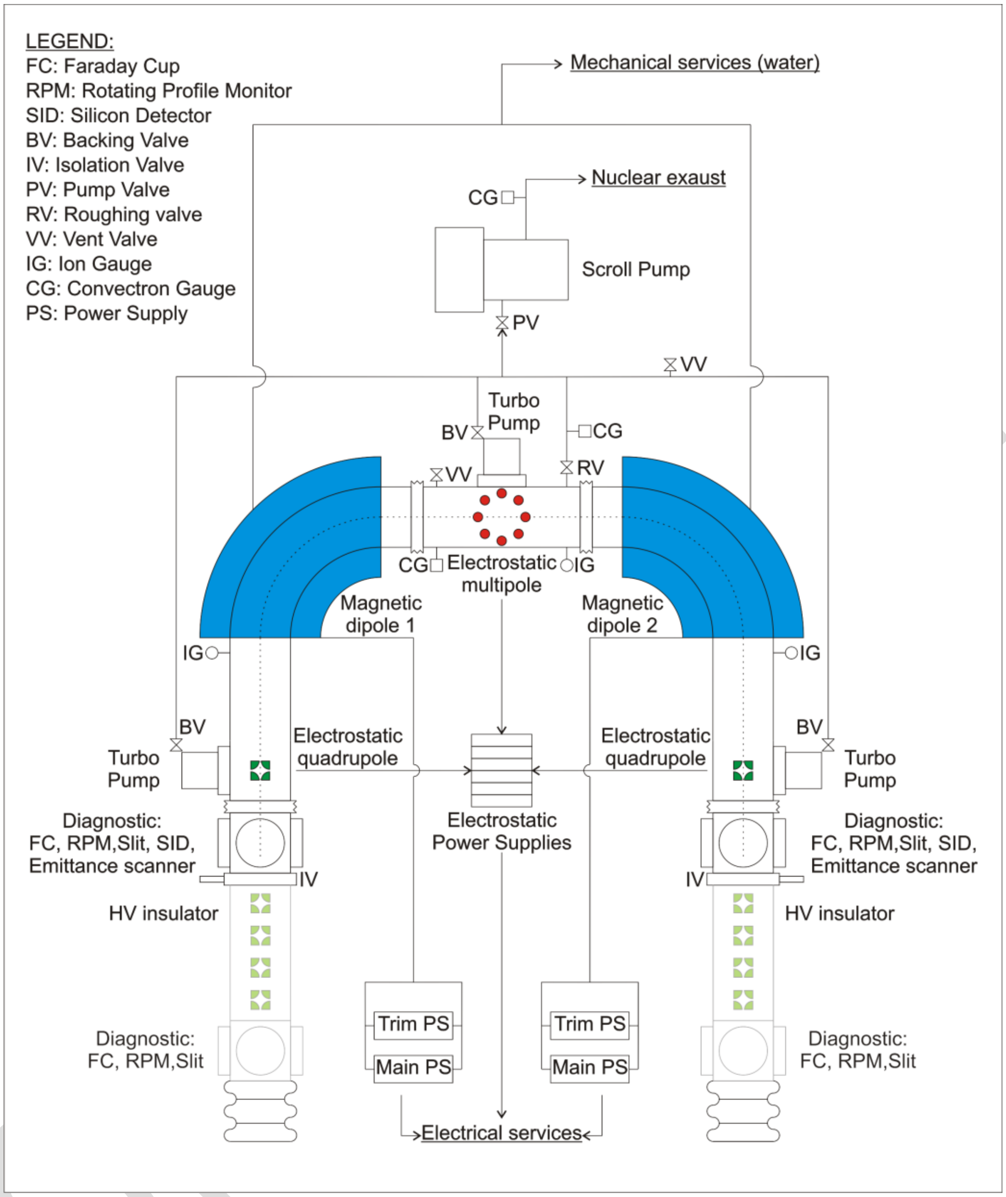

Figure 13: Schematic of HRS.

There are also a number of diagnostic elements:

- Faraday cups will be used to measure high intensity beam currents at the entrance and exit slits and between the dipoles. Scintillator detectors will be used for measuring low intensity beam currents.
- Rotating beam profile monitors will be used to measure the beam profile at the entrance and exit slits
- CEM emittance scanners will measure the transverse beam emittance at the entrance and exit slits and between the dipoles.
- Additional diagnostics to measure the beam emittance and phase space profile are recommended in the waist aperture diagnostic box.

The current optical design was determined from simulations using COSY and TRANSOPTR. The initial constraints placed on the optimization were:

- A fixed bending radius of 1.2 meters for the two 90 degree magnet dipoles, and spacing between the dipoles of 1.6 meters. The bending radius is the largest that can be accommodated given the space available for the HRS. The spacing between the magnetic dipoles was fixed at 1.6 m and chosen to align with the locations of incoming and outgoing beamlines.
- A single electrostatic multipole corrector was used between the magnetic dipoles to correct non-linear effects in the beam and improve transmission and resolution.
- Mirror symmetry in the HRS was maintained around the middle of the electrostatic multipole corrector.
- Both magnetic dipoles are identical in design.
- Fringe fields were included in all simulations using COSY internal modelling defaults.

The shape of entrance and exit shapes of the dipoles and the drift length between the dipoles and the waist slits from the pure separator were adjusted so that imaging was also achieved in the horizontal plane. Since the optics do not image in the vertical plane, studies were done to verify that there were no deleterious effects due to coupling for the desired vertical beam emittance. Corrections for aberrations up to 3rd order were made by introducing an edge curvature to the dipole entrance and exit edges, and by using the sextupole and octupole fields from the electrostatic multipole corrector. The horizontal and vertical beam motion between the waist aperture slits is shown in Figure 14(a) and (b).

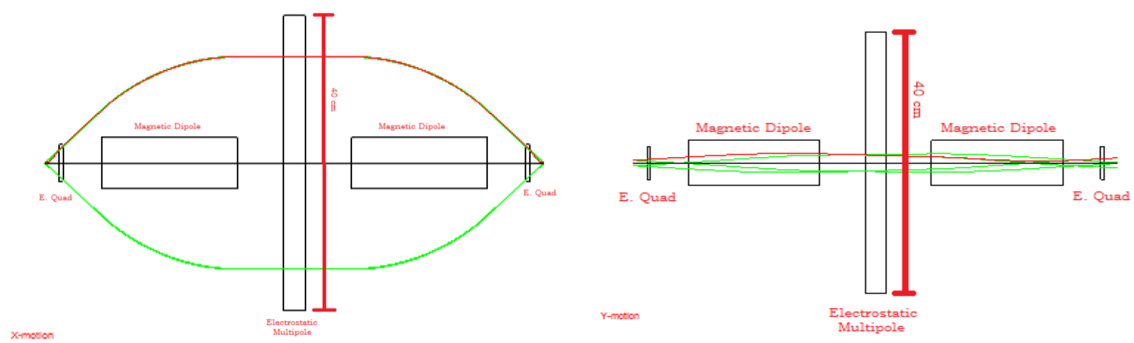

Figure 14(a) and (b): Simulation of beam (a) horizontal and (b) vertical beam motion for the pure separator portion of the HRS.

As previously mentioned, the electrostatic quadrupoles located inside the HRS (between the mass selection slits) system will be used to correct any minor perturbations resulting from variance in the dipole edge angle from the magnet design. Otherwise, the system is expected to operate similarly to the "pure" spectrometer previously discussed in this note. The electrostatic multipole is also capable of generating a quadrupole field is needed to setup the linear optics of the HRS.

The parameters for this new design (excluding the matching/magnification section discussed in the next section of this note) are listed in Table 2.

Table 2: Parameters for the Pure Separator Portion of the HRS

Parameter	Value
Drift length to E. quad	0.200 m
E. quad length	0.050 m
Drift length from E quad to Dipole	0.5997 m
Dipole Edge Angle	26.56 degrees
Dipole Edge Radius of Curvature	2.2379 m
Dipole Vertical full aperture	0.070 m
Drift length between Dipole and Multipole	0.650 m
Multipole length	0.300 m
Multipole half aperture	0.200 m

The pure separator section of the HRS has also been simulated in two other beam simulation codes, GIOS and Zgoubi. These simulations yielded consistent results to the COSY and TRANSOPTR models. Figure 15 shows the final spot size for 3 masses differing by 1:20000 using GIOS.

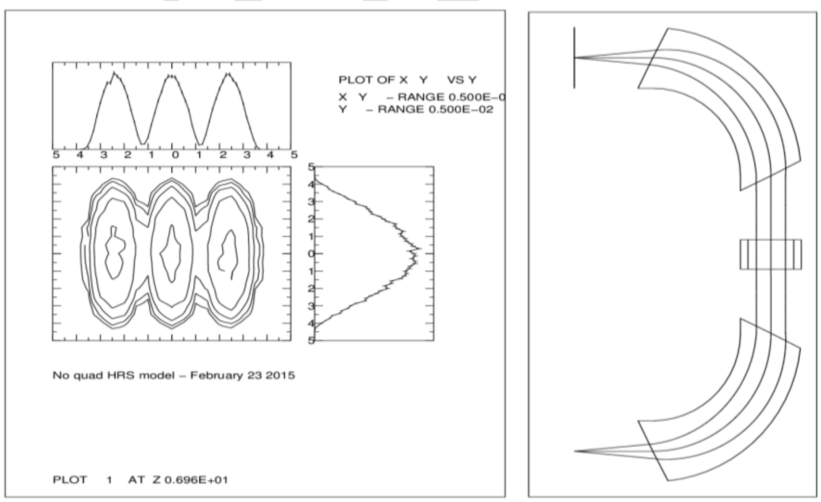

Figure 15: GIOS simulation of (a) Final spot size for the pure separator portion of the HRS and (b) Top view of the pure separator modelled using GIOS.

7 Matching/Magnification Sections

As previously mentioned, the present HRS design incorporates matching/magnification sections. In the design presented in the initial release of this document and at the first review in 2014, two electrostatic quadrupoles were used to accept a beam with a larger horizontal position spread and smaller angular deviation into the HRS. In the present design, the electrostatic quadrupole located nearest to each dipole will only be used to make nominal corrections to the linear design.

Since the "pure separator" case for our target emittance and angular spread would require a horizontal beam size smaller than could be practically maintained with mechanical slits, magnification sections are added before and after the pure separator portion of the HRS that match the same emittance with a wider horizontal aperture and reduced initial angular spread. These same sections will also act as a matching section to the periodic sections of the beam line.

Figure 16 shows a simulation using COSY of the horizontal motion through the HRS from entrance to exit slit with the matching/magnification sections:

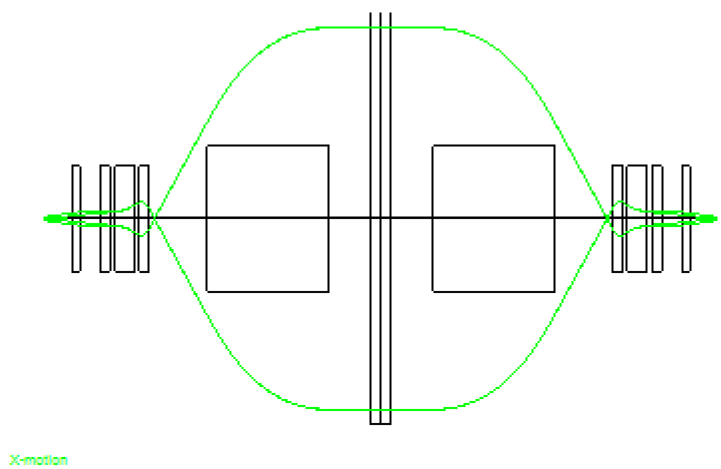

Figure 16: Simulation of beam horizontal beam motion for the HRS.

Figure 18 shows the horizontal beam motion for the matching section as generated with TRANSOPTR. The horizontal and vertical motion of the beam in just the matching/magnification sections is shown in Figure 17(a) and (b). The parameters for the matching/magnification section used in this simulation are given in Table 3. Although there are 4 electrostatic quadrupoles in the matching/magnification section, as shown in Figure 16, only 3 are used to match into the pure separator portion of the HRS in this example. The 4th is available as an additional corrector to make the optics more robust. Additional studies are ongoing to further optimize this matching/magnification section.

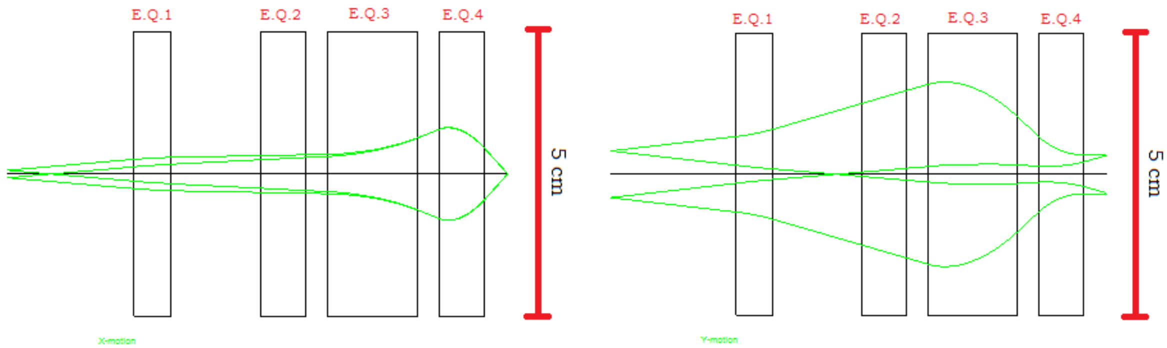

Figure 17(a) and (b): Simulation of beam (a) horizontal and (b) vertical beam motion for the matching/magnification sections of the HRS.

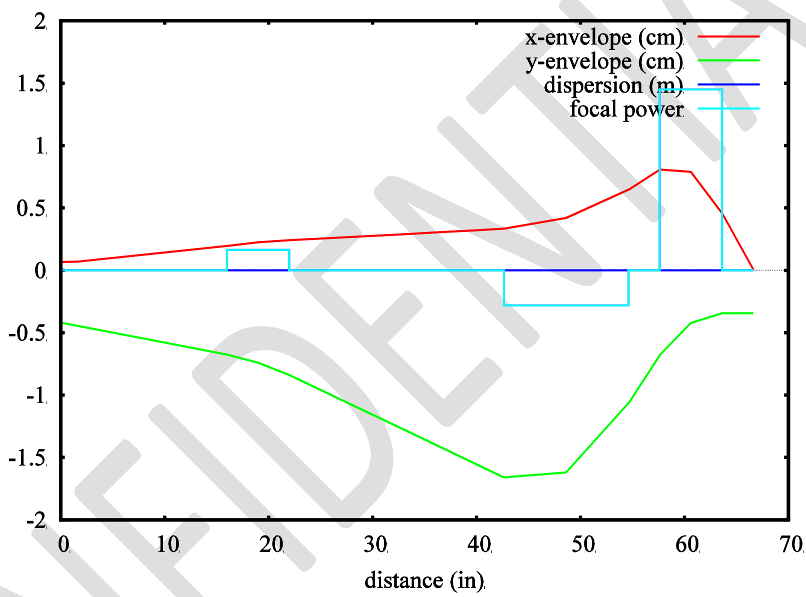

Figure 18: TRANSOPTR plot for the beam envelopes slit to slit for the pure HRS separator. The dispersion is also plotted as a function of momentum (twice mass based dispersion).

CONFIDENTIAL

Table 3: Parameters for the Matching/magnification Section of the HRS

Parameter for Matching/Magnification Section	
Drift length to 1st E. quad	0.4064 m
1st E. quad length on 0.1524 m and poletip voltage of 0.3784 kV	
Drift length to 2nd E. quad	0.29558 m
2nd E. quad length 0.1524 m and poletip voltage of 0.00 kV	
Drift length to 3rd E. quad	0.0762 m
3rd E. quad length 0.3048 m and poletip voltage of -0.5415 kV	
Drift length to 4th E. quad	0.0762 m
4th E. quad length of 0.1524 m and poletip voltage of 2.7227 kV	
Drift length to pure separator	0.0762 m

Figure 19 is a phase-space plot showing separation for adjacent masses using this design at the exit of the final matching section.

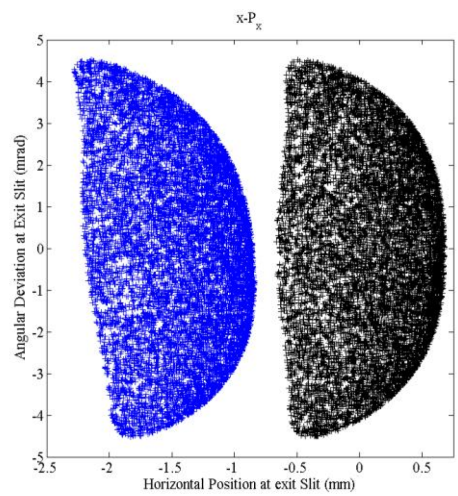

Figure 19: 5th order simulation of horizontal phase space at the end of the matching/magnification section for 3 pi µm beam with DE = 1 eV.

8 Aberration Correction in the HRS

Nonlinear effects (i.e. optical aberrations) in the HRS can substantially limit the resolution of the system. These effects occur naturally from the geometry of the magnets as well as the falloff fringe field from both the magnetic and electrostatic elements. Beyond the first order calculation, resolution can be adjusted to account for these aberrations in the beam optics. To accomplish this, COSY is used to determine the dependency of the final beam width Δx_{actual} on the initial parameters of the beam:

$$\Delta x_{actual} = (2|(x|x)d_i| + |(x|x^2)|d_i^2 + |(x|xa)d_i a_i| + \cdots)$$

where $(x|x^2)$ and $(x|xa)$ are 2nd order coefficients from the transfer map of the HRS determined by COSY, and d_i and a_i represent the half width and the initial angular spread $\left(p_x/p_{ref}\right)$ of the beam at the entrance (source) slit. Then the actual resolution can then be expressed as:

$$R_{actual} = \frac{|(x|\delta)|}{\Delta x_{actual}}$$

CONFIDENTIAL

Simulations of the pure separator portion of the HRS model in COSY identify the largest nonlinear effects. Because horizontal angular deviation within the beam is large, aberrations that depend on the initial value of angular deviation (ex. (x|aa), (x|aaa)) are among the largest.

Table 4: Largest Aberrations in the HRS Optical Design Affecting Final Horizontal Beam Position

Aberration coefficient [ex. x|aa is the is variation of horizontal position (x) due to the square of initial angular spread in the beam (aa)]	**Variation in final horizontal position at exit slit (meters) before corrections**	**Variation in final horizontal position at exit slit (meters) after 5th order corrections**
x|aa	-8.597 E-3	9.247 E-7
x|yy	-2.953 E-7	-2.922 E-7
x|bb	-2.551 E-4	1.518 E-5
x|aaa	1.812 E-6	-7.723 E-11

The second order aberrations effecting horizontal beam width can be corrected by introducing curvature to the dipole entrance and exit edges and introduction of a sextupole field with the multipole corrector. The multipole corrector is also used to correct the largest 3rd order aberration to final horizontal position via introduction of octupole fields. Additional corrections of the largest 4th and 5th order aberrations could be accomplished by introducing decapole and duodecapole fields in the corrector. For example, Table 2 summarizes the voltages used and changes to R_{actual} as a result of these corrections using radius of 1.47 m. The final column shows reduction in the horizontal aperture need to reach R_{actual} of 20,000.

Table 5: Parameters for Electrostatic Multipole Corrector and Resolution Effect for 3 pi µm Emittance with 1 eV Total Energy Spread

Highest Multipole Order of Aberration Correction	**Voltage at Poletip (kV) for 20 cm radius aperture**	**R_{actual} based on simulation in COSY to 5th order**	**Horizontal waist aperture half-width needed for R=20000**
Uncorrected		272	Unachievable
2nd (Sextupole)	0. 32290	4488	Unachievable
3rd (Octupole)	0. 03765	14516	28 µm
4th (Decapole)	0. 00482	16397	37 µm
5th (Duodecapole)	-0. 00131	16918	39 µm

CONFIDENTIAL

Aberration corrections to 3rd order are obviously the most critical to the performance of the HRS. Correction of 4th and higher order terms, while possible, is likely impractical due to the small voltages that would be needed and limitations in beam diagnostics to resolve these higher order effects. Simulations with aberrations through 8th order have also been done to verify convergence in the Taylor series represented in COSY's transfer map.

Two alternative methods were considered for correction of aberrations. In the first case, a dipole edge curvature for a radius of 2.2379 m was used to minimize the 2nd order aberration based on the square of initial horizontal angle. An octupole with poletip voltage of 0.000155 kV (for a 20 cm radial aperture) was used to minimize the largest 3rd order aberration. Figure 20(a) and (b) show the final horizontal phase space at the exit of the separator for a beam with 3 pi μm and 6 pi μm vertical emittances. In this simulation, the spot size of the ribbon beam entering the HRS has a 1:10 horizontal to vertical aspect ratio (+/- .05 mm x .5 mm). The dramatic difference is due to a 2nd order aberration based on the square of initial vertical angular deviation (x|bb). Although this option has the advantage of requiring only minor use of the multiple corrector, it means throwing away half of the beam produces by a 6 pi μm source due to limited vertical acceptance. Further studies demonstrate that this acceptance issue can be corrected increasing the position spread for the vertical emittance to +/- 2 mm or greater. For a 6 pi μm vertical emittance, this reduces the angular spread to only +/- 3 mrad.

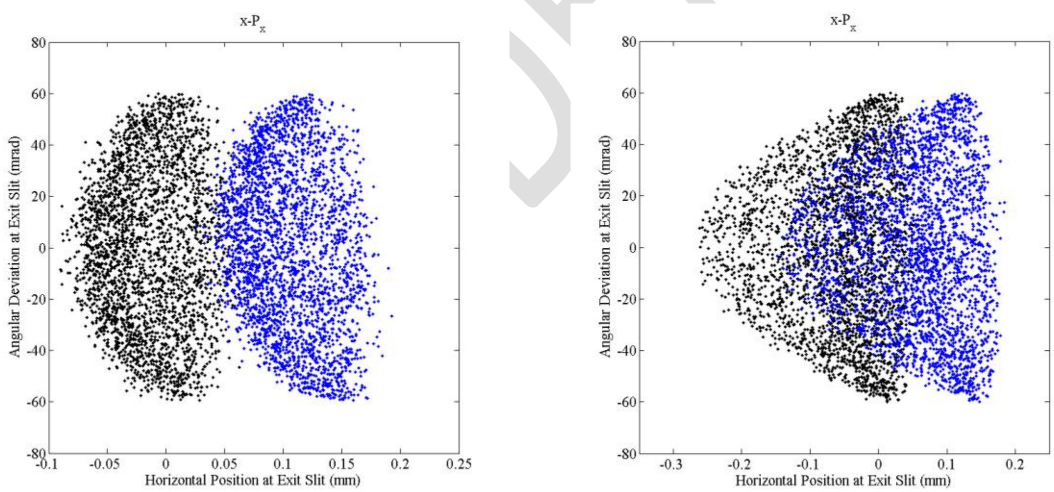

Figure 20(a) and (b): Final phase space for two masses differing by 1/20000 at exit slit for pure HRS separator with a horizontal emittance of 3 pi μm and vertical emittance of (a) 3 pi μm and (b) 6 pi μm.

Another option was to use a sharper edge curvature of 1.47 m radius, with both a sextupole and octupole multipole correction. This option allow acceptance of the full 6 pi mm vertical emittance, as shown in Figure 21. This is accomplished by overcorrecting the horizontal nonlinearities with the edge curvature, which allows reduction of the (x|bb) aberration. A sextupole component of the multipole corrector is then used to recover correction of the horizontal second order aberrations. This option also requires a stronger octupole from the multipole corrector.

Simulations have also verified that solutions exist to correct these aberrations for curvatures between these two cases. Solutions closer to former option require smaller voltages for the correction sextupole and octupole, but require a reduced vertical angular spread to avoid limited vertical acceptance while solutions closer to the latter option using stronger multipole fields and allow greater vertical acceptance. A decision has been to proceed with the initial option (using the larger radius of curvature for the dipole edge and nominal use of a sextupole field from the multipole corrector). Simulations have shown that the multipole corrector can compensate for machining edges in the dipole edge curvature of up to 1 mm.

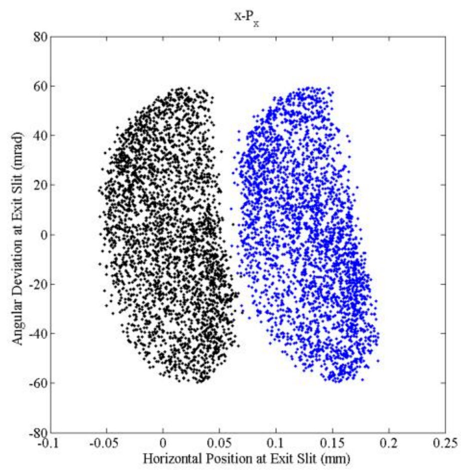

Figure 21: Final phase space for two masses differing by 1/20000 at exit slit for pure HRS separator with a horizontal emittance of 3 pi µm and vertical emittance of 6 pi µm.

It is understood that the complete model for the HRS magnetic dipoles being developed with OPERA (and discussed in detail in the next section) will differ substantially from the homogeneous dipole model in COSY. The magnetic field data for the magnet and fringe field regions from the OPERA model have been used to update the COSY simulations. In these studies, field map data was generated for a grid of points in OPERA. OPERA computes the magnetic field values consistent with Maxwell's equations at vertices create from a mesh of the model. In between these vertices, the field values are interpolated. Adjusting the mess size reduces the range over which this interpolation in applied. The OPERA model for the HRS dipoles forces vertices to be drawn at locations in the midplane that are used for generating the field map data. This is intended to minimize nonphysical errors that could occur from interpolated data.

The imported field maps include both the physical space taken up by the magnet, but also the fringe field region traversed by the beam. Figure 22 shows an example of the separation of 2 masses (reference and +1:20000) in the pure separator portion of the HRS based on the OPERA field map data. This case uses a model with the more extreme 1.47 m dipole edge radius of curvature. The multipole has been used to correct residual 2nd and 3rd order aberrations. As can be seen from the comparison in Table 6, the OPERA model results are very consistent with the simulations using COSY's homogeneous dipole model.

CONFIDENTIAL

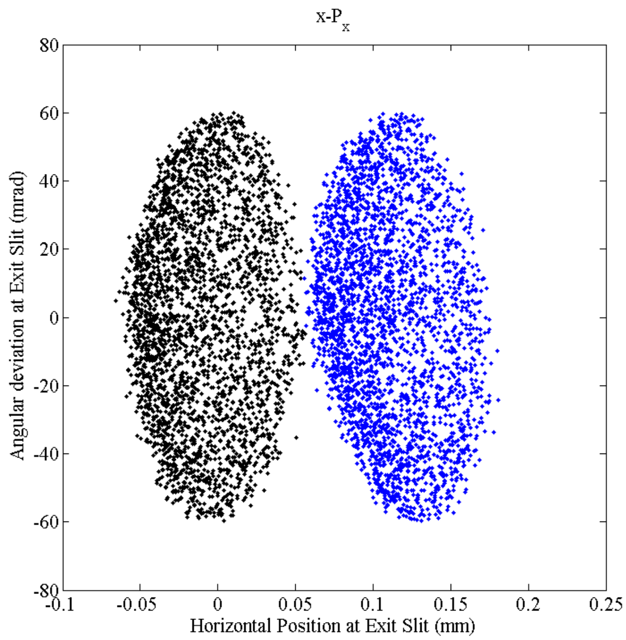

Figure 22: Final phase space for two masses differing by 1/20000 at exit slit for pure HRS separator based on OPERA field map data.

Table 6: Comparison of Parameters for the Electrostatic Multipole Used to Correct of Aberrations in the HRS for Homogenous and OPERA Model Dipoles

Highest Multipole Order of Aberration Correction	Voltage at Poletip (kV) for 20 cm radius aperture in COSY with DI dipole model	Voltage at Poletip (kV) for 20 cm radius aperture in COSY with OPERA field map model
2nd (Sextupole)	0. 32290	0.34030
3rd (Octupole)	0. 03765	0.05728

CONFIDENTIAL

9 Optimization of the Magnetic Dipole Fields

The magnetic dipole design and relative field are calculated respectively with the 3D-modeller® and the TOSCA® solver of the OPERA-3D® software[1]. The magnet iron, coils and surrounding air volumes coordinates are parameterized meaning they are calculated as a function characteristic dimensions of the magnet (reference radius of curvature, angle of entrance and exit face, pole gap, etc.). Figure 23 shows some of the iron coordinates. The parameterized coordinates are inserted in a geometry generator file (standard OPERA COMI file).

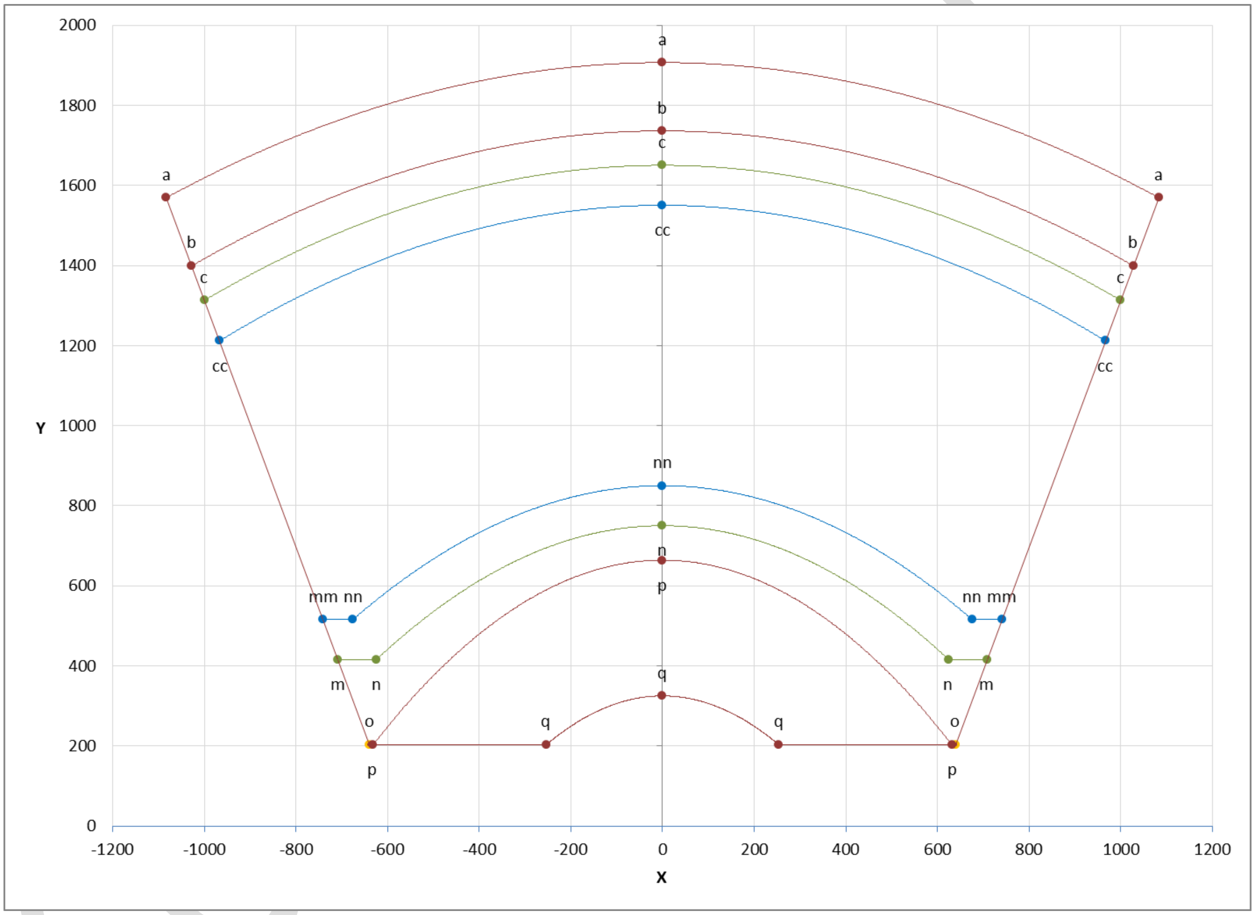

Figure 23: Example of parameterized coordinates of the HRS dipole.

Figure 24 shows a rendering of one of the basic dipole configuration; we refer to this as the reference geometry (HRS-ACSI-12-Cq2) generated with the COMI file. The reference geometry is the starting point of the optimization. Its dimensions are based on practical knowledge given the pole gap dimension[2].

[1] All the magnet renderings presented in this chapter are an output of OPERA-3D® software.
[2] George Clark private communication.

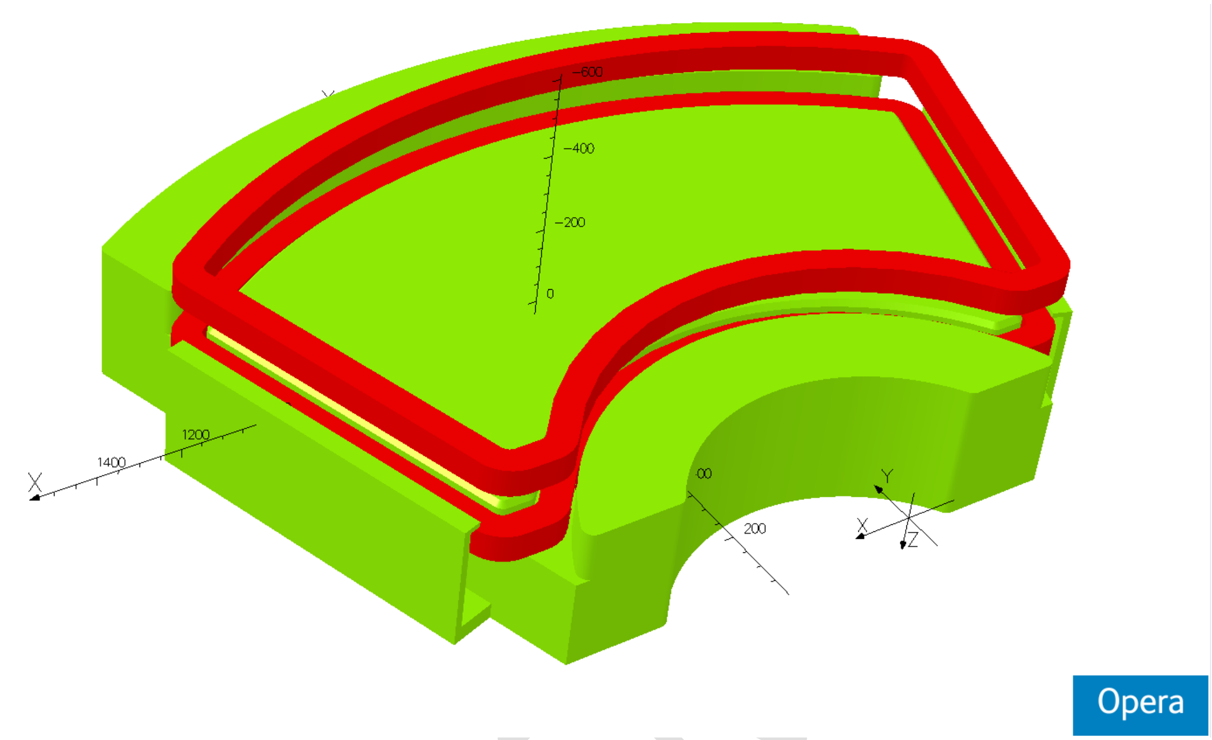

Figure 24: Rendering of the reference geometry (HRS-ACSI-12Cq2).

We define the reference geometric trajectory as the path follow by the reference particle travelling through a hard-edge dipole magnet. The latter is a simplified magnet in which the field goes from zero to a value B_0 at the entrance of the magnet and vice-versa at the exit, maintaining B_0 everywhere inside the dipole. The reference geometric trajectory is the red path represented in Figure 25; this is composed of an arc[3] inside the hard edge boundaries connected on the outside to two straight paths tangential to the arc. Other geometric trajectories are composed by an arc concentric to the reference one that stops at the hard edge boundaries and two straights parallel to the reference straight paths.

We define field flatness as follow:

$$field\ flatness = \frac{B_z}{B_0} - 1$$

where B_0 is the vertical component (z direction) of the magnetic field at the center of the realistic magnet (from OPERA); this center has coordinates (0,1200), see Figure 23.

[3] The radius of the arc is related to the B0, the mass and the velocity of the reference particle (assumed to be singled charged).

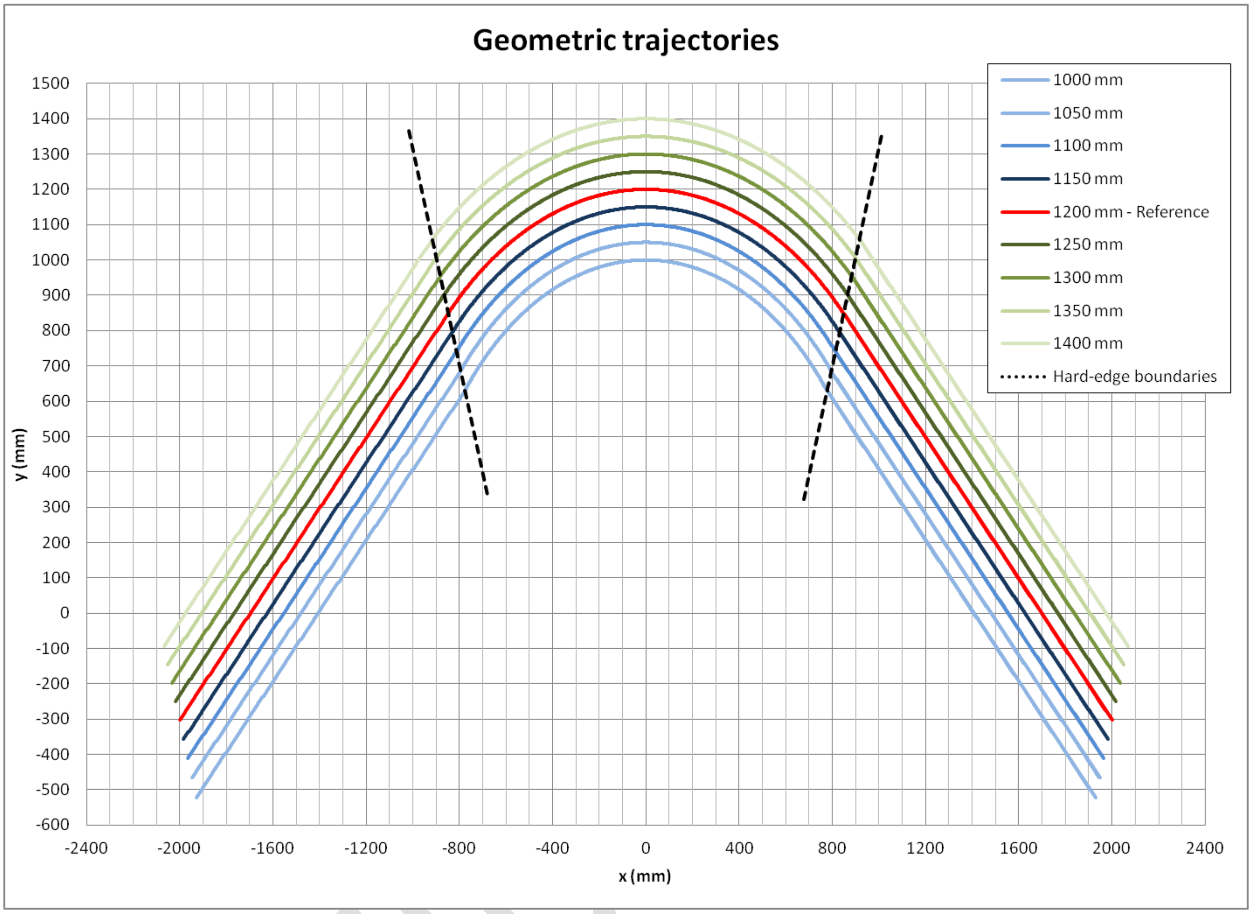

Figure 25: Geometric trajectories. The reference trajectory represented in red has a radius of curvature of 1200 mm.

We define the integral ratio for any given geometric trajectory as follow[4]:

$$IR_\rho = \frac{\int_l \ B_z(s)\, ds}{\int_{arc} B_0\, ds}$$

Where $B_z(s)$ is the magnetic field vertical component of the OPERA magnet along the considered geometric trajectory of path l. At the denominator the integral of the hard-edge case is done only over the arc component of the geometric trajectory since the field integrals along the straights are zero by construction.

We define the integral flatness as follow:

$$Integral\ flatness = \frac{IR_\rho}{IR_{1200}} - 1$$

where the index ρ represents a geometric trajectory ($\rho = 1200$ being the reference one).

[4] This is the same definition given in Document-74319 (ARIEL high resolution spectrometer requirements)

CONFIDENTIAL

The optimization is achieved by studying the field flatness as a function of selected design parameters and by comparing the field integrals of the OPERA model with respect to the equivalent (B_0 equals to the field value at the center of the pole) hard-edge case. The optimization criteria are stated in the "ARIEL high resolution spectrometer requirements" Document-74319.

The integrals are calculated along the geometric trajectories represented in Figure 25. These nine trajectories are spaced 50 mm apart from an internal bending radius of 1000 mm to an external of 1400 mm, 1200 mm being the reference radius of curvature as per the beam dynamics. The straight paths extend 1628 mm beyond the hard edge boundaries.

The first optimization goal is a field flatness in the radial direction at the center of the pole of $2.5 \cdot 10^{-5}$ or better inside a region that extends ±160[5] mm good field region around the reference geometric trajectory in the middle plane; we define this to be the good field region. The second optimization goal is an integral flatness $2.5 \cdot 10^{-5}$ or better within the good field region. The requirements document also specified an upper limit for the $\left|IR_\rho - 1\right|$ being $1 \cdot 10^{-3}$ or better. This value is related to the position of the effective field edge with respect to the hard-edge case.

The initial coil section is 69×69 mm with a current density of around 2.6 A/mm^2, this generate a field in the reference geometry of about 0.45 T. In the calculation we used the C1006 BH curve.

The vertical magnetic field component (B_z) along the geometric trajectories and the field flatness of the reference design are represented respectively in Figure 26 and Figure 27. The field component is plotted as a function of the angle where zero degrees corresponds to center of the magnet (symmetry axis) in Figure 23, while ±45 degree corresponds to the hard edge point on the reference geometric trajectory. The flatness is plotted as a function of the radial position; the red portion of the curve in Figure 26 represents the flatness within the limit of the geometric trajectories.

We also evaluate the field integral along geometric trajectories to study the effective field. The integrated field to bend mass 238 at 60 keV (Bρ equals to 0.548 T·m) around the reference trajectory is circa 0.860 T·m and the field at the center of the pole is circa 0.457 T.

---

[5] This region is based on optics calculation.

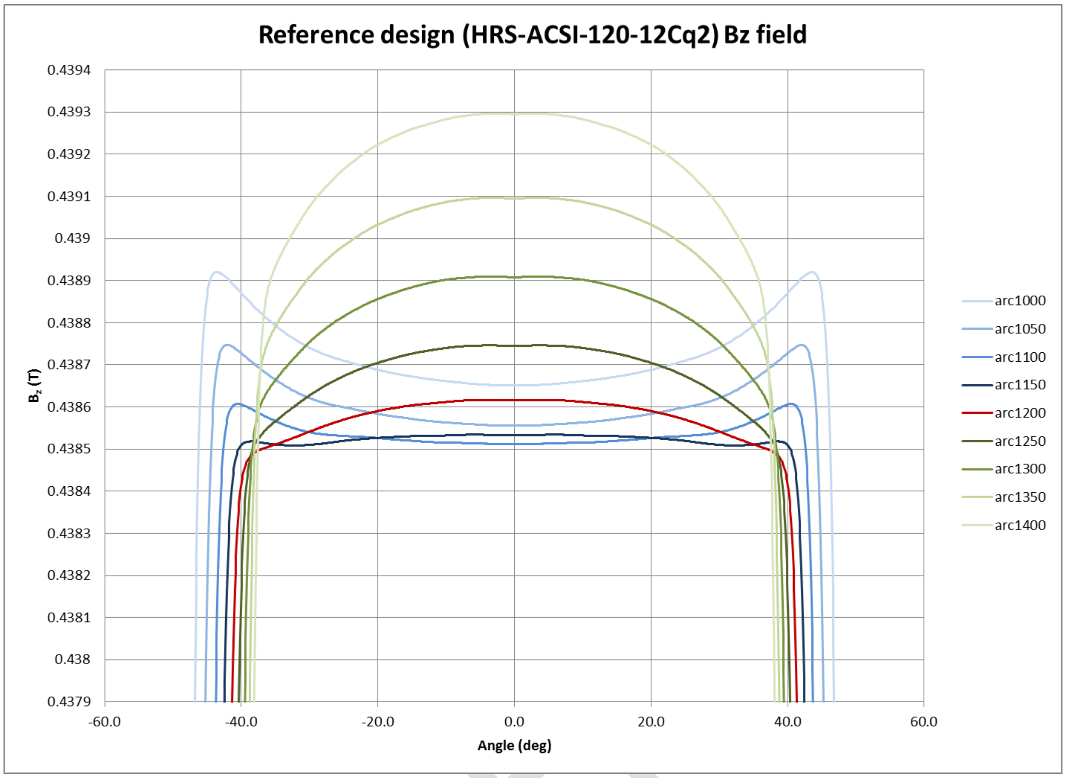

Figure 26: Reference design vertical field component: the red line represents the reference geometric trajectory.

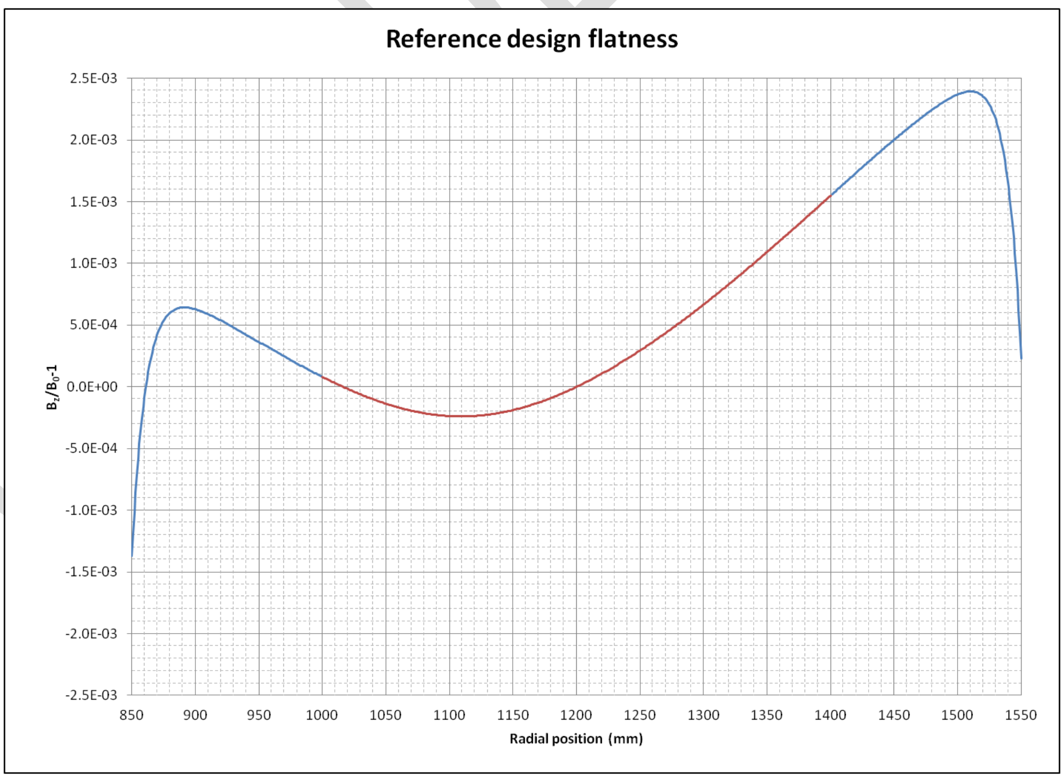

Figure 27: Reference design flatness: the red portion of the curve represents the flatness within the limit of the geometric trajectories.

9.1 Flatness versus pole gap

The minimum pole gap is limited by the beam envelope. The initial gap dimension of 70 mm takes into account both the vertical beam envelope and the vacuum chamber dimension. The vertical beam envelope based on initial first order calculation is around 5 mm; we allow for a vertical space inside the vacuum chamber in the order of 10 times the envelope. The vacuum chamber wall thickness is estimated to be 10 mm.

Reducing the beam gap allows to reduce the coil current for the same magnetic field. On the other end OPERA calculations show that a narrower gap has increased the flatness value, as shown in Figure 28. A 50 mm gap required 26% less current and increase the flatness value by 40%. On the other end an 80 mm gap required 15% higher current and reduces the flatness value by 12%. The initial 70 mm gap is a good compromise between current and flatness. This value is maintained in the following optimization.

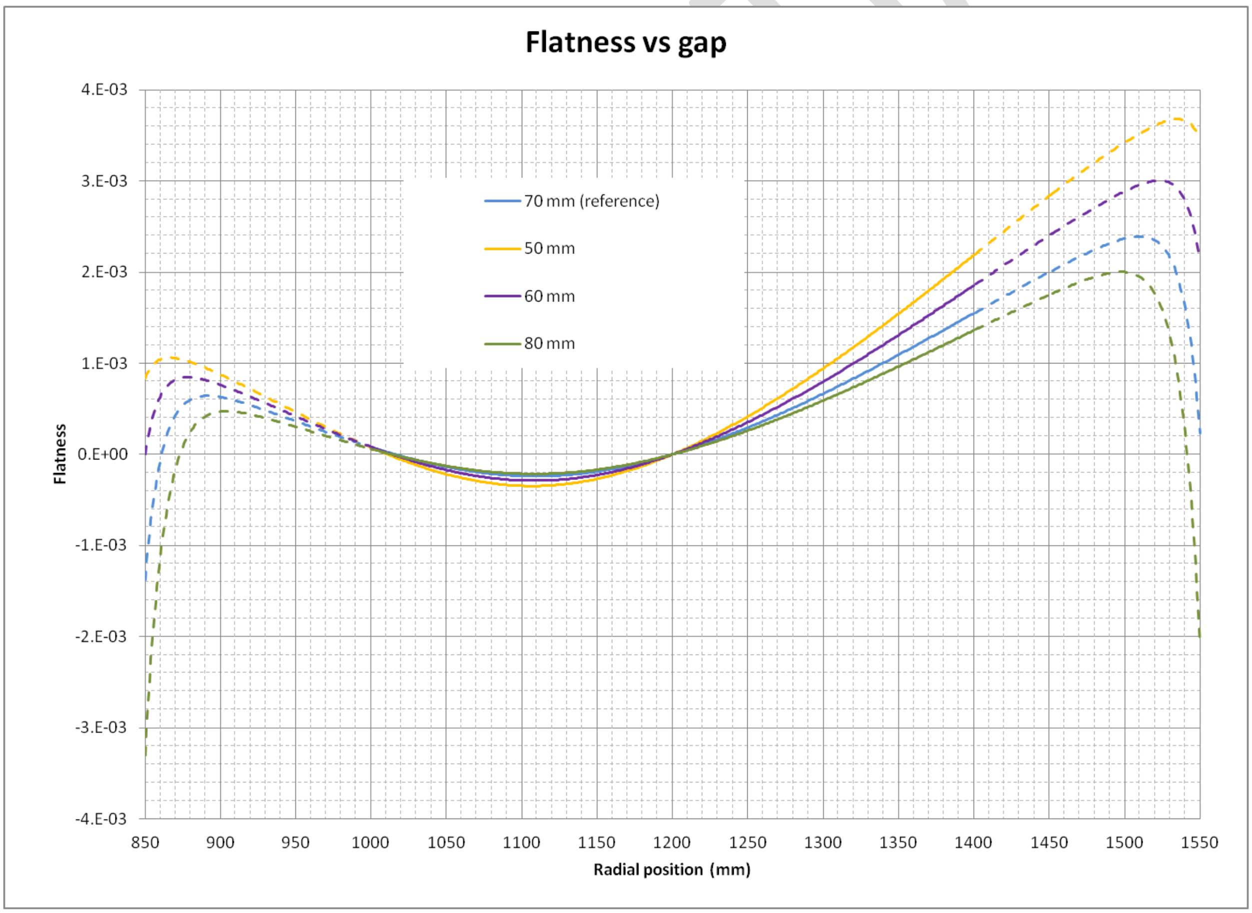

Figure 28: Flatness versus gap; the solid line represent the flatness within the limit of the geometric trajectories.

9.2 Return yokes flux balance

The radial symmetry of the reference design results in the magnetic flux through the internal yoke (with a lower radius of curvature) is higher than the one through the external yoke (with a higher radius of curvature). This asymmetry in the flux distribution causes the field along the external trajectories (from 1250 to 1400) to be higher than those with an internal trajectory (from 1150 to 1000), as seen in Figure 26. Before proceeding to the next round of investigation, the magnetic flux density through each of the return yokes (Bmod in OPERA) is equalized.

We consider two different methods for the equalization. On an historical note, the second method comes later in time; this is the reason why a first round of optimization uses the first one. As we are going to show, the second method returns a far better result and it is also easier to implement from a mechanical point of view.

In the first method, the equalization is achieved by having equal surface areas of the return yoke in the horizontal and vertical planes as represented in Figure 29.

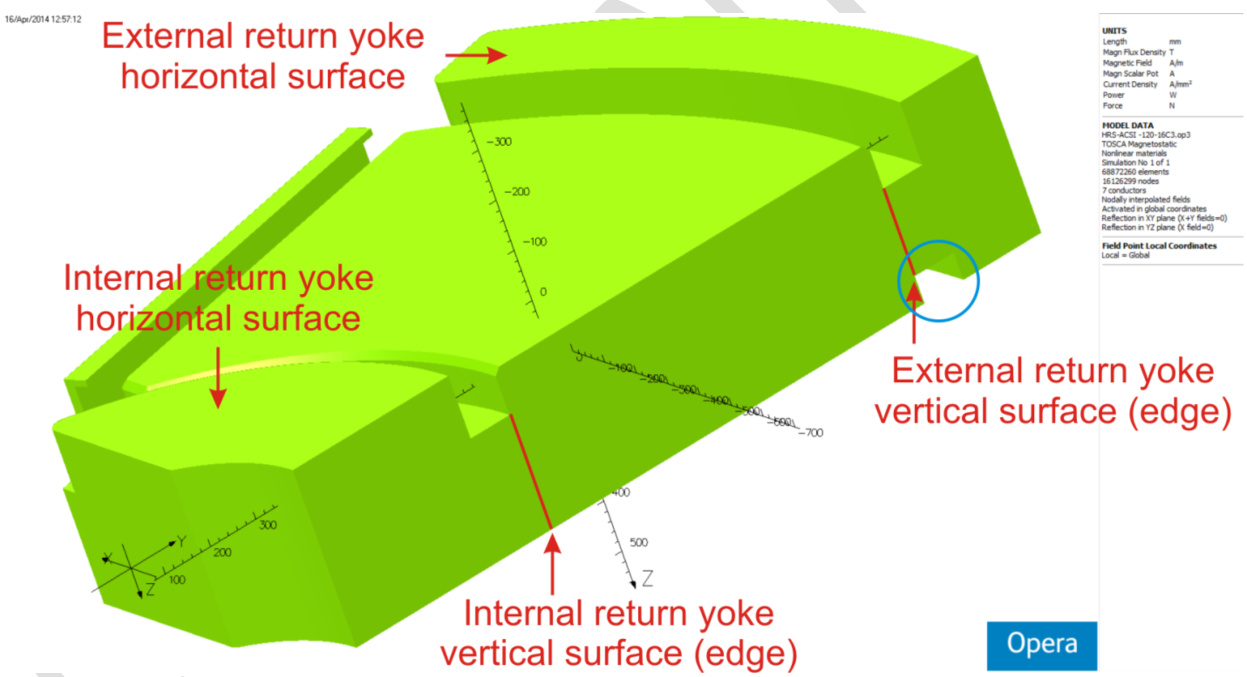

Figure 29: Return yoke surfaces utilized for area equalization (HRS-ACSI-120-16C3). The edges of the vertical surface are the red straight lines. The blue circle identifies the carved channel of the external yoke necessary to equalized the external return yoke vertical surface

In order to achieve equal surface in the vertical plane we carve a channel in the external yoke iron in the b-c coordinates region (see blue circle in Figure 29). This makes all the considered surfaces equals. The height of the carved channel is a parameter of the geometry generator COMI file. The result is plotted in Figure 30 where the field along external and internal geometric trajectory are similar.

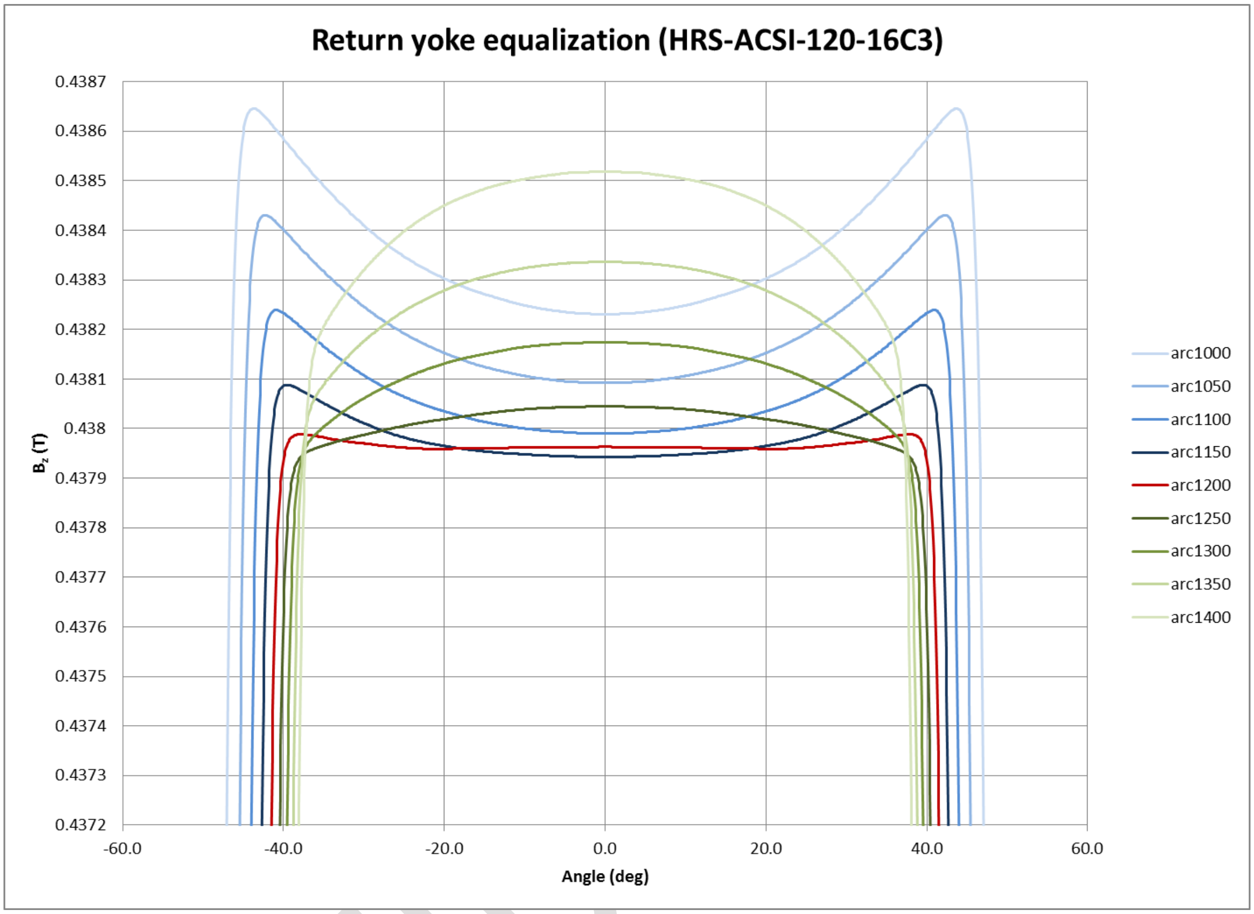

Figure 30: Return yoke surface areas equalization.

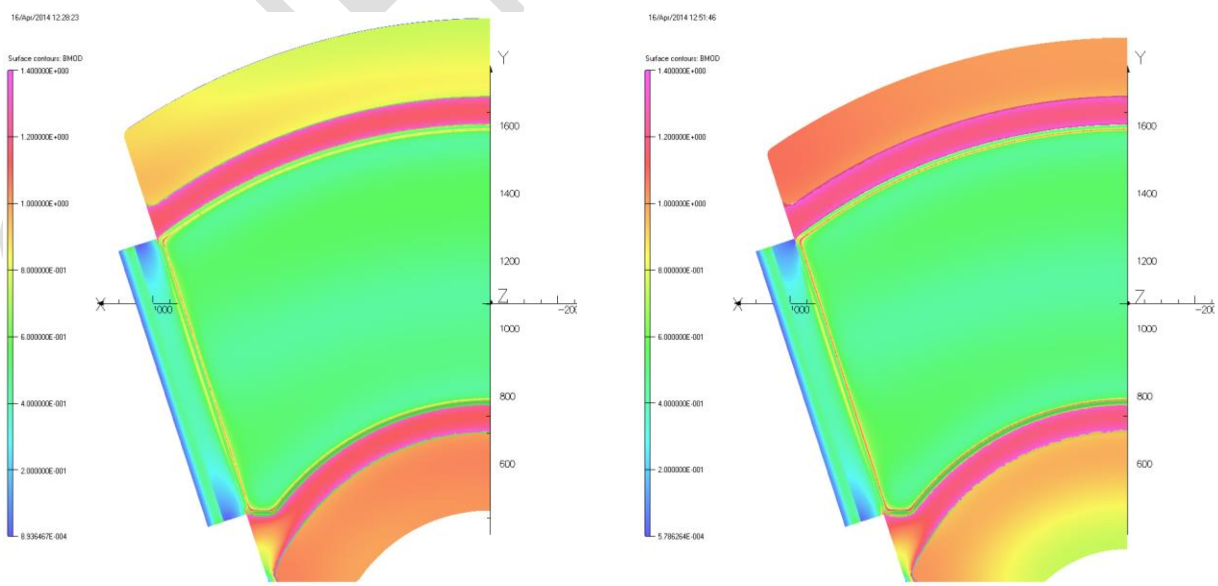

Figure 31: Magnetic flux through the return yoke before (left) and after (right) equalization using the first method. The color range goes from 0 (blue) to 1.4 T (purple).

In the second method, we consider only the horizontal surfaces of the return yoke and the pole face surface (no carved channel). This last one is split in two portions, the divider being the radius of curvature where the magnetic flux split inside the return yoke. This splitting point is the tip of the blue dome pictured in Figure 32. This splitting point corresponds in our case to a radius of curvature of circa 1170 mm. We call internal portion the one containing radii <1170 mm, and external portion the other.

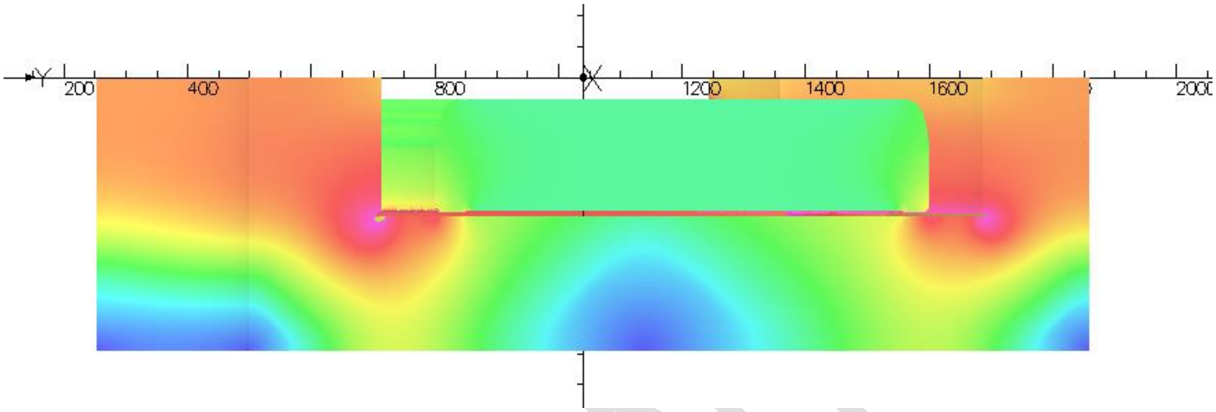

Figure 32: Cut view of the dipole magnet: the blue dome tip in the return yoke is the splitting point of the magnetic flux.

The equalization is achieved by making equal the two surface ratios between the internal return yoke surface and the internal portion and between the external return yoke surface and the external portion.

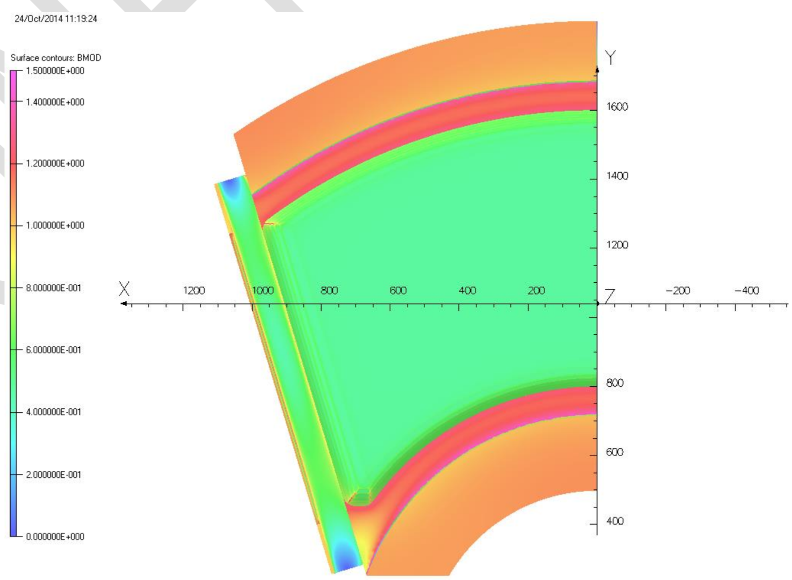

Figure 33: Magnetic flux through the return yoke equalization using the second method. The color range goes from 0 (blue) to 1.5T (purple).

9.3 Flatness versus pole height

We distinguish two regions in the central part of the magnet, as illustrated in Figure 34, the pole and the pole base. The boundary of the two regions is the plane that contains the base of the coil channel.

The first set of simulations is done by fixing the pole base height, at 229.5 mm, with respect to the reference geometry and varying the pole height. The coil elevation with respect to the horizontal middle plane is also fixed. The pole height is changed from 90 mm (reference) to 180 mm in step of 30 mm. A second set of simulations is done by fixing both the pole height, at 180 mm and the pole base height and varying the elevation of the coil toward the base of the coil channel. We move the coil two steps down, each of 30 mm magnitude. Lastly a final set of simulations is done with the pole height and the elevation of the coil fixed and varying the height of the pole base ±60 mm around the original value.

The results of these studies are summarized in Figure 35. Increasing both the pole and the pole base height results in a decrease of the flatness value. This results in a heavier and more expensive magnet due to the increase of the iron volume. The location of the coil gives marginal improvement of the flatness (yellow and orange curves in Figure 35), but it is preferred to sit the coil at the base of their channel (it seems reasonable to assume that this is also the simpler mechanical solution as far as coil location).

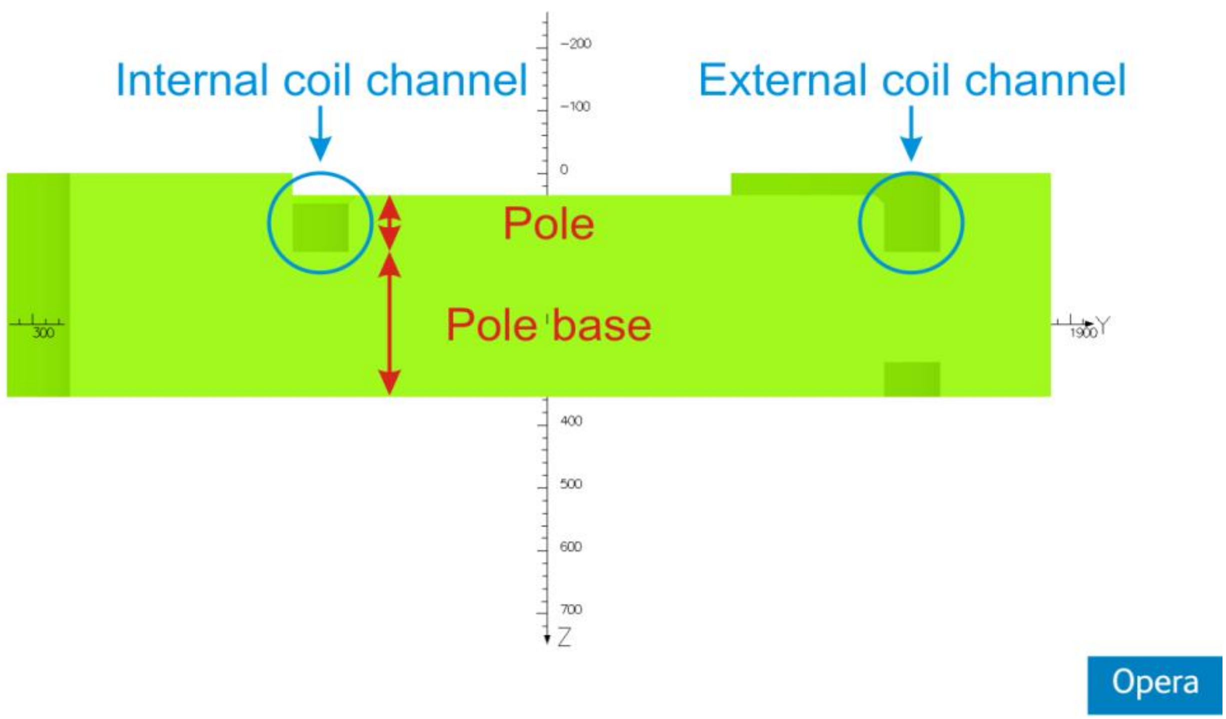

Figure 34: The picture illustrates the difference between pole and pole base.

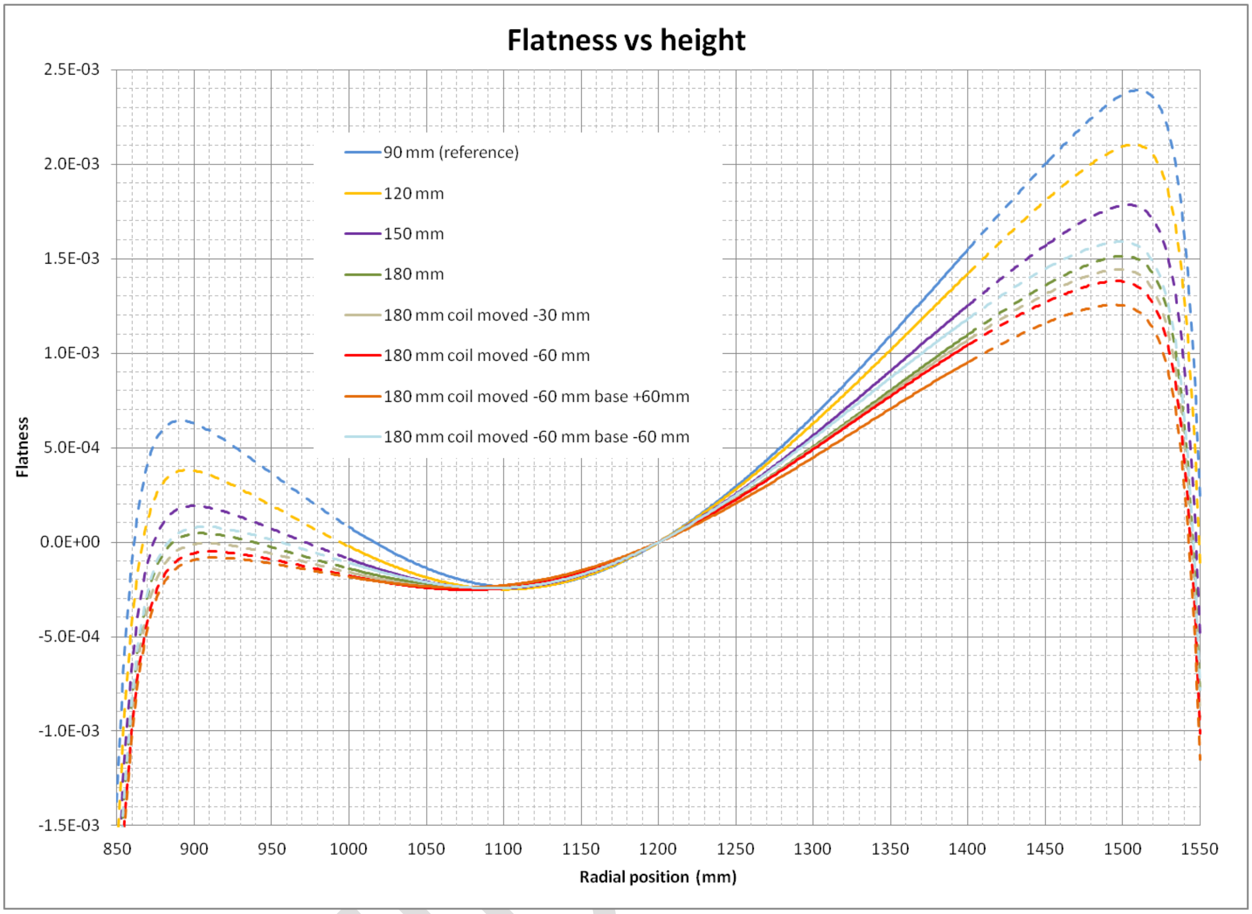

Figure 35: Flatness as a function of pole and pole base height and coil location.

9.4 Flatness versus pole width

The strength of the field in the external trajectories is diminished when the pole width is reduced because they are more sensitive to the edge effect. This improves also the flatness up to the point where the edge effect is so strong that the flatness value starts increasing (in absolute value).

The results of the calculation are displayed Figure 36. Starting from a reference 826 mm width, we increase it up to 926 and down to 526 in step of 100 mm.

The strong edge effect is seen at 526 mm where the flatness value increase. The vertical field component and relative flatness are detailed in Figure 37. The field at the two extreme trajectories (1000 and 1400) falls well below the field in the reference trajectory.

The best result in term of flatness is the 626 mm case, but the good field region is on the edge of the field fall off.

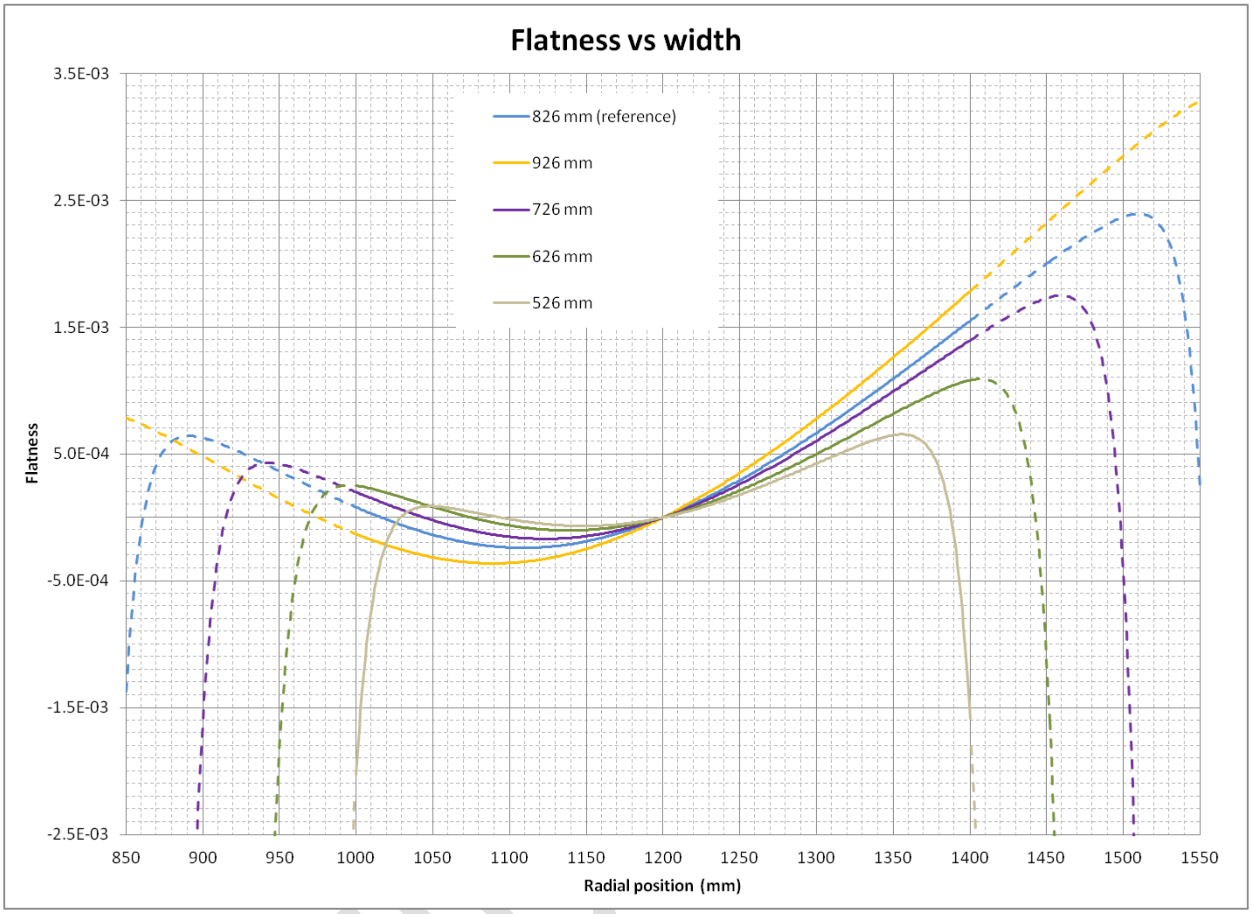

Figure 36: Flatness versus pole width.

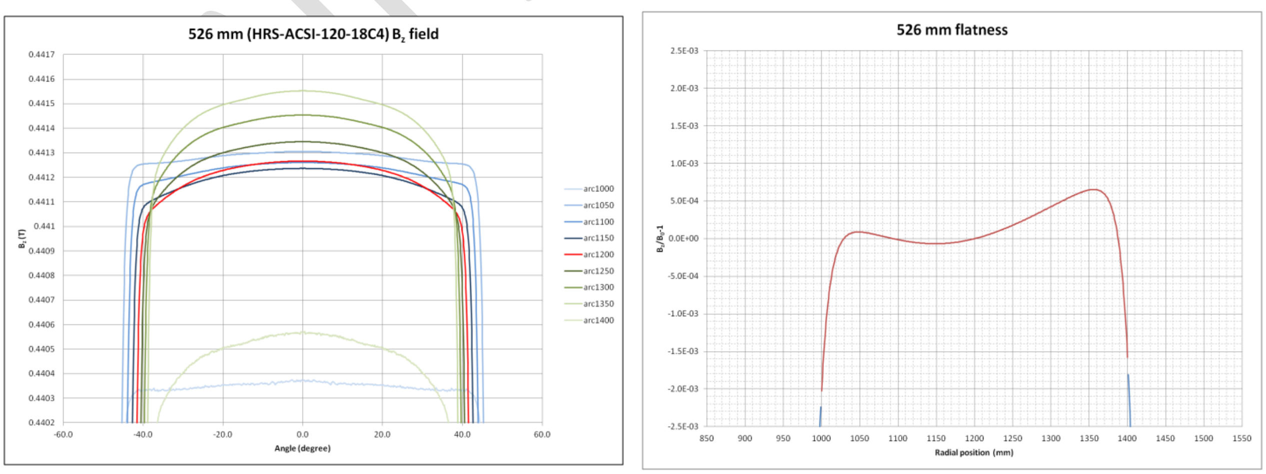

Figure 37: Flatness versus pole width. In this case the strong edge effect increases the flatness.

9.5 Nominal geometry

The first round of investigation produces a new geometry that we call the nominal geometry to distinguish it from the initial reference design. The main dimensions of this new geometry are the following:

1. Pole gap equal to 70 mm
2. Pole height equal to 180 mm
3. Pole base height equal to 229.5 mm. This is not changed with respect to the reference to avoid a significant increase of the iron volume.
4. Pole width equal to 676 mm
5. Equalizing channel height 44 mm
6. Coil sit 8.5 mm above the base of their coil channel. This is a realistic location since the real coil don't sit directly on the iron[6]

The vertical field component and relative flatness are represented respectively in Figure 38 and in Figure 39.

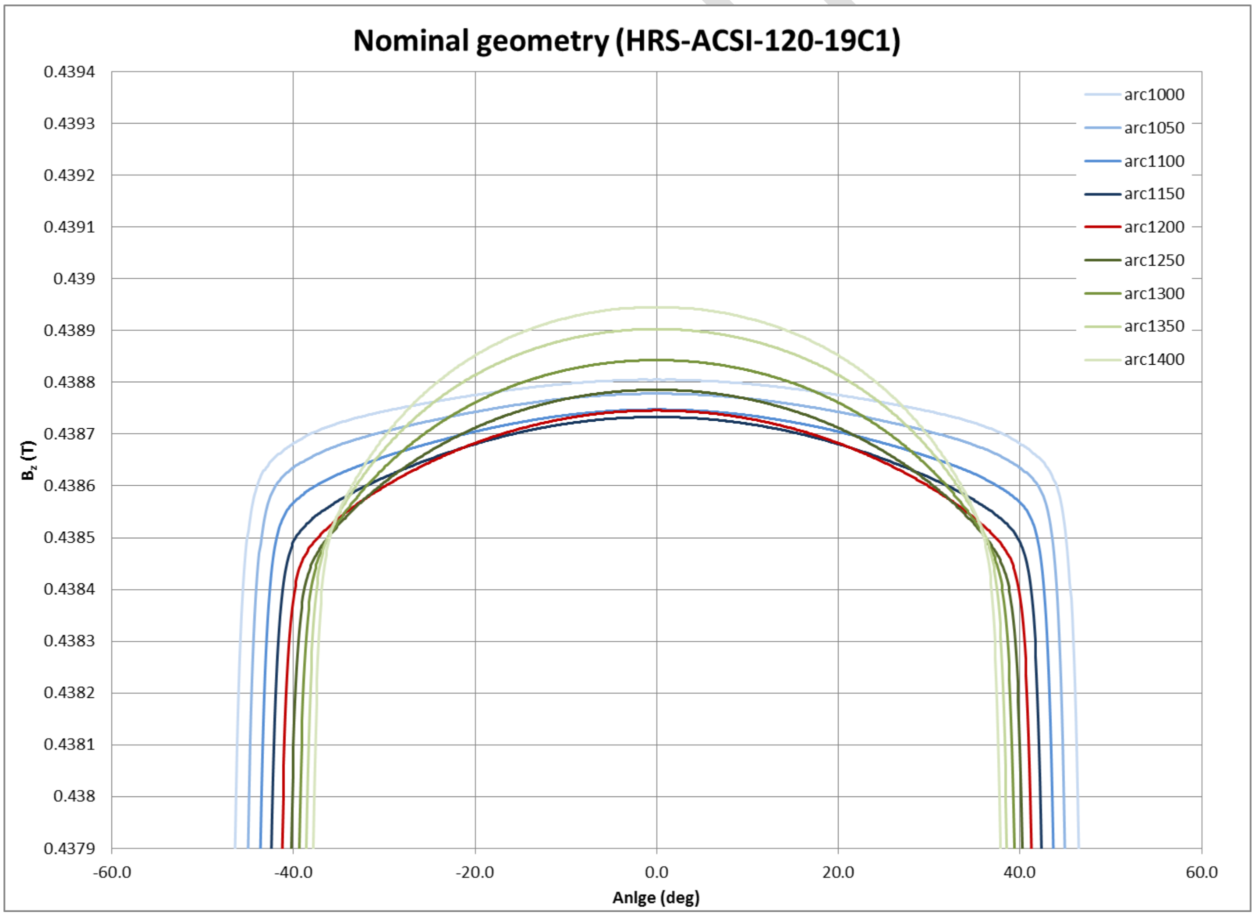

Figure 38: Vertical field component of the nominal geometry (HRS-ACSI-120-19C1).

[6] George Clark private conversation.

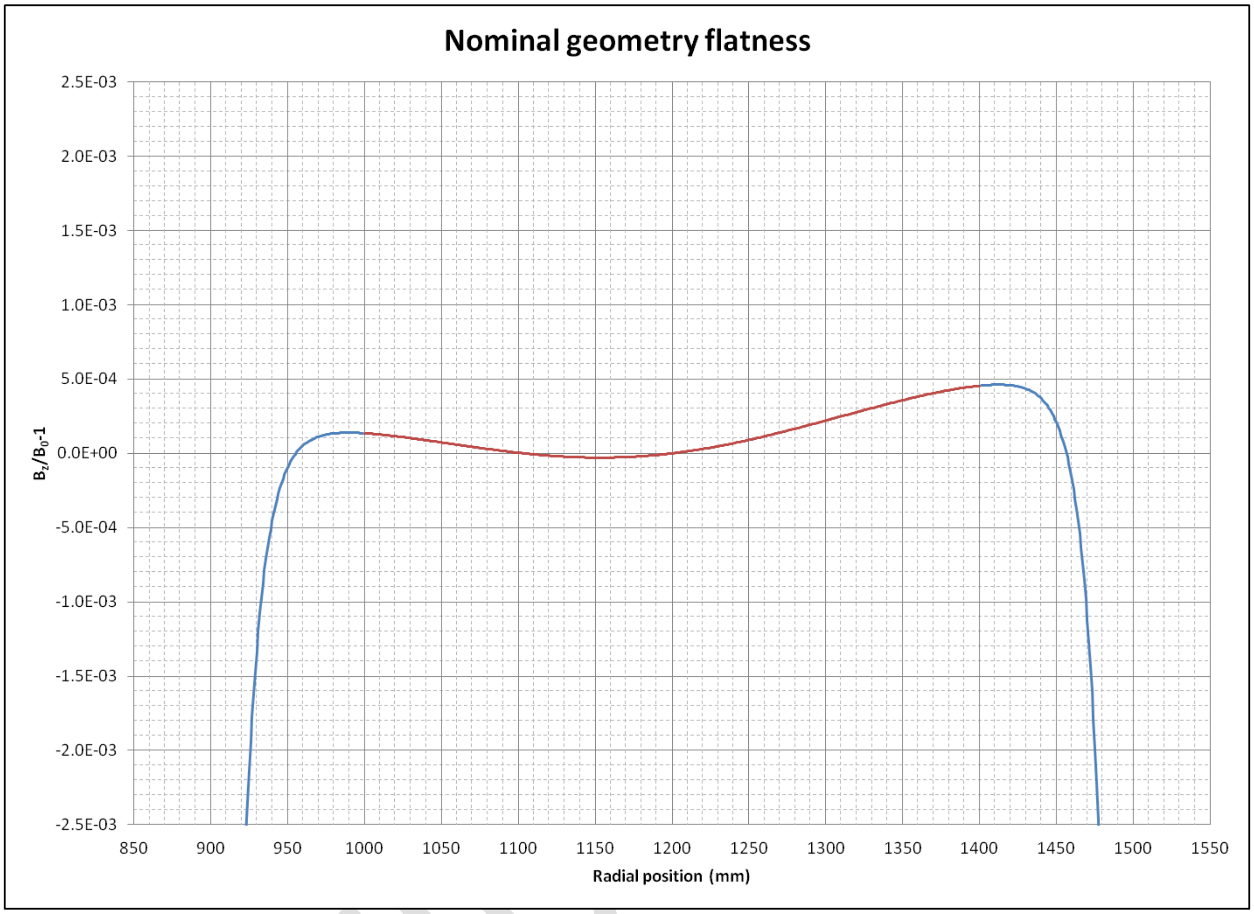

Figure 39: Flatness of the nominal geometry (HRS-ACSI-120-19C1).

9.6 Rogowski profile

Before proceeding with the investigation of the Purcell filter, we consider the introduction of the Rogowski profile to reduce the saturation of the pole edges so to maintain field reproducibility at different current excitation level. The theoretical curve is approximated with 4 straight cuts giving the geometry represented in Figure 40. We chose to apply the profile to all the edges of the pole.

Since the profile is obtained by removing iron from the edges, this reduces the effective pole width. This implies that if we create a Rogowski profile starting from the nominal case, we increase the flatness value due to edge field effect.

The geometry represented in Figure 40 differs from the nominal in terms of pole width equal to 800 mm. This is the minimum width necessary to avoid edge field effect, but it still has a higher flatness value with respect to the nominal case.

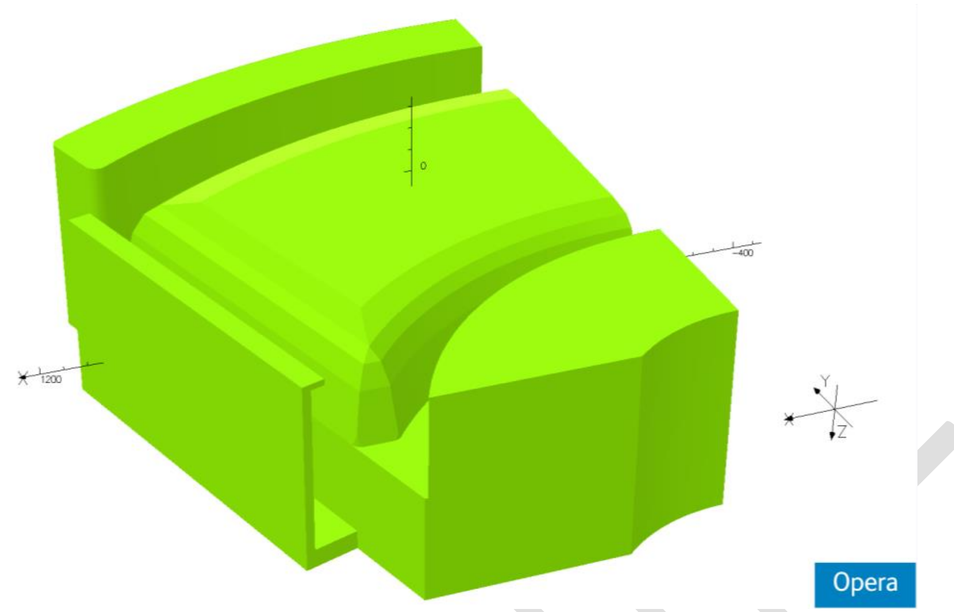

Figure 40: Geometry with applied approximate (4 cuts) Rogowski profile.

In order to evaluate the effectiveness of this profile we simulate both the nominal case and the Rogowski geometry at a lower current that produces a field around 0.087 T (a field adequate to bend a particle of mass around 10).

In order to compare the two cases we plot the field relative longitudinal profile along the geometric trajectories with respect to the reference (namely $\frac{B_z}{B_{z-1200}} - 1$, notice that in this case the reference case is constantly zero). The longitudinal coordinate is converted to an angle, zero degree corresponding to the center of the magnet.

The relative longitudinal profile at reduced current for the nominal and Rogowski are represented respectively in Figure 42 and Figure 44. These are compared with the respective full current cases.

The Rogowski profile has an advantage with respect to the simple 45 degree edge cut of the nominal geometry in term of field fall off reproducibility (at the entrance and exit edges) at different excitation levels. This means that the optics behaviour of the separator is also consistent at the two levels. Figure 45 shows the iron field of the nominal and the Rogowski geometry for both the high and low current cases.
On the other end, a Rogowski profile reduces the effective pole and in particular the location of the effective field edges. If we want to implement this profile and match the effective field boundaries to the hard edge case then we need a longer pole.

We are going to implement a scaled Rogowski to maintain optical property at different excitations and at the same time to control the location of the effective field edges without elongating the pole. Details of the implemented profile are given in paragraph 9.9

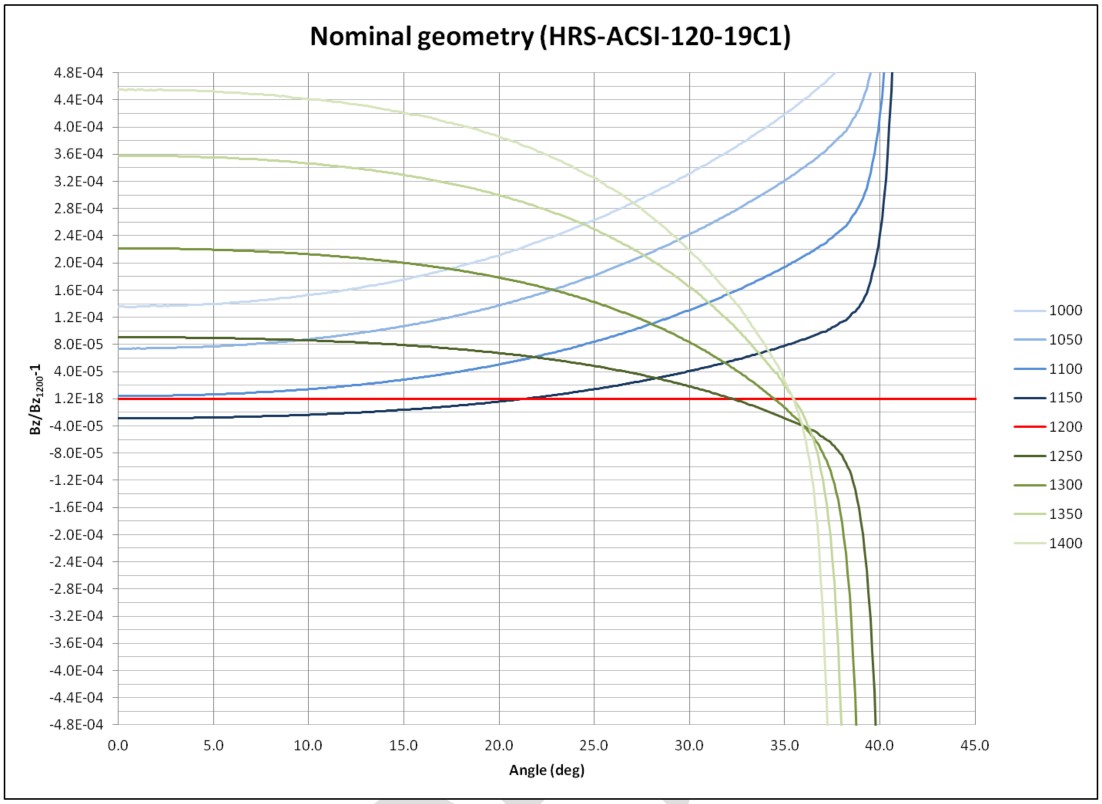

Figure 41: Relative longitudinal profile of the nominal geometry (HRS-ACSI-120-19C1).

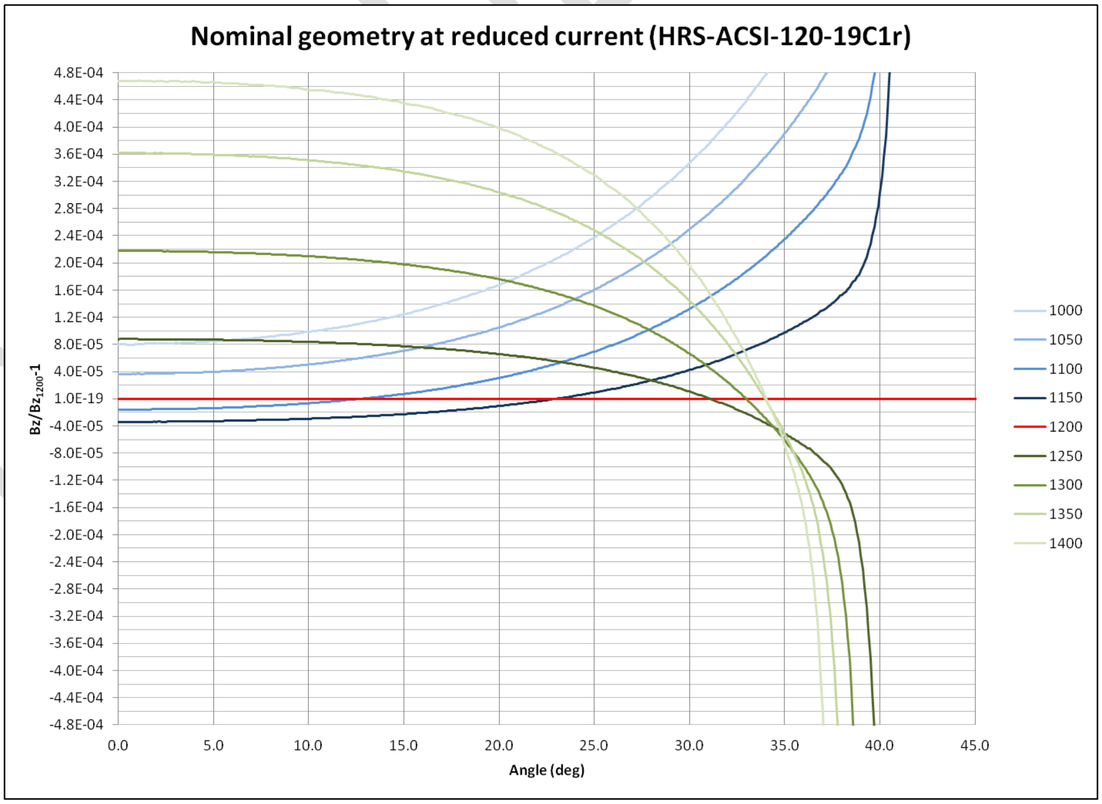

Figure 42: Relative longitudinal profile of the nominal geometry at reduced current (HRS-ACSI-120-19C1).

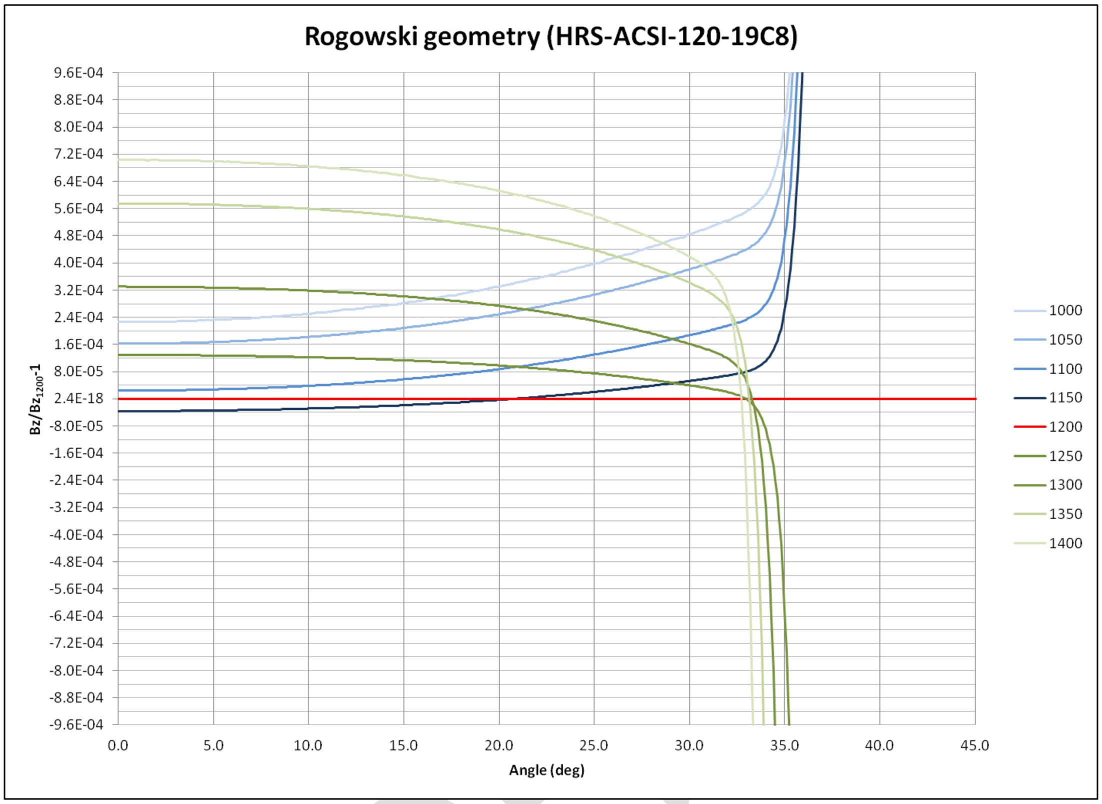

Figure 43: Relative longitudinal profile of the Rogowski geometry (HRS-ACSI-120-19C8).

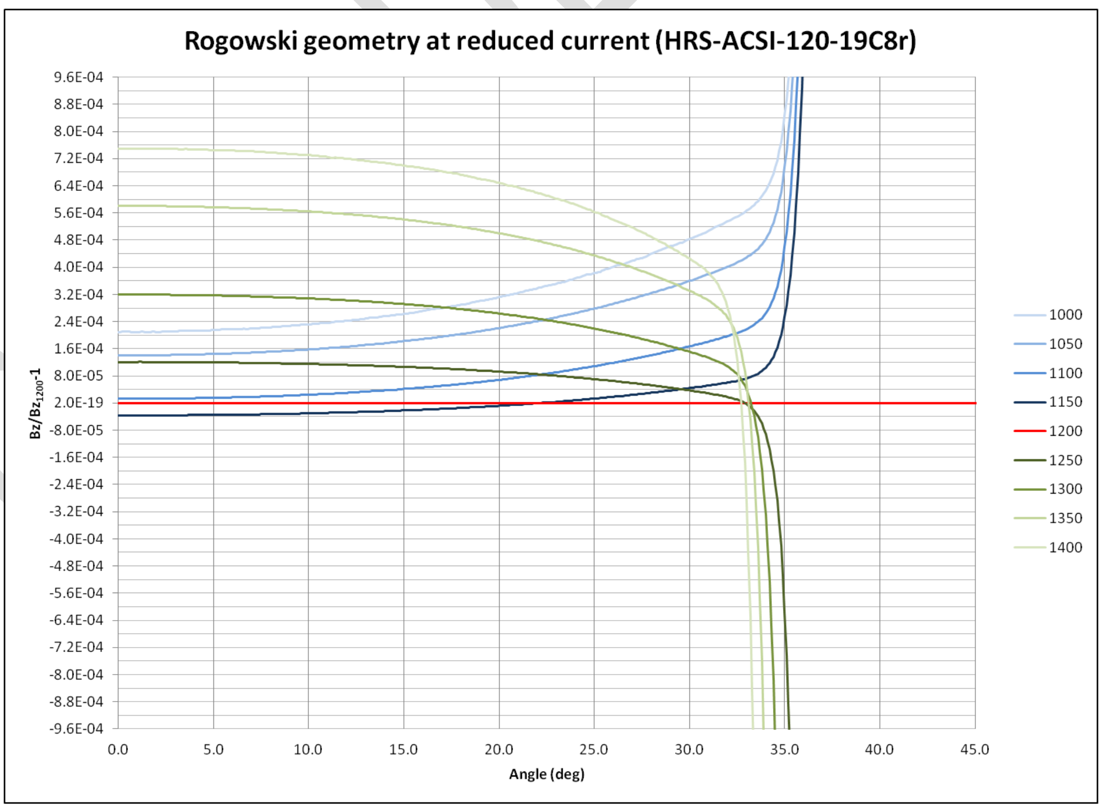

Figure 44: Relative longitudinal profile of the Rogowski geometry at reduced current (HRS-ACSI-120-19C8).

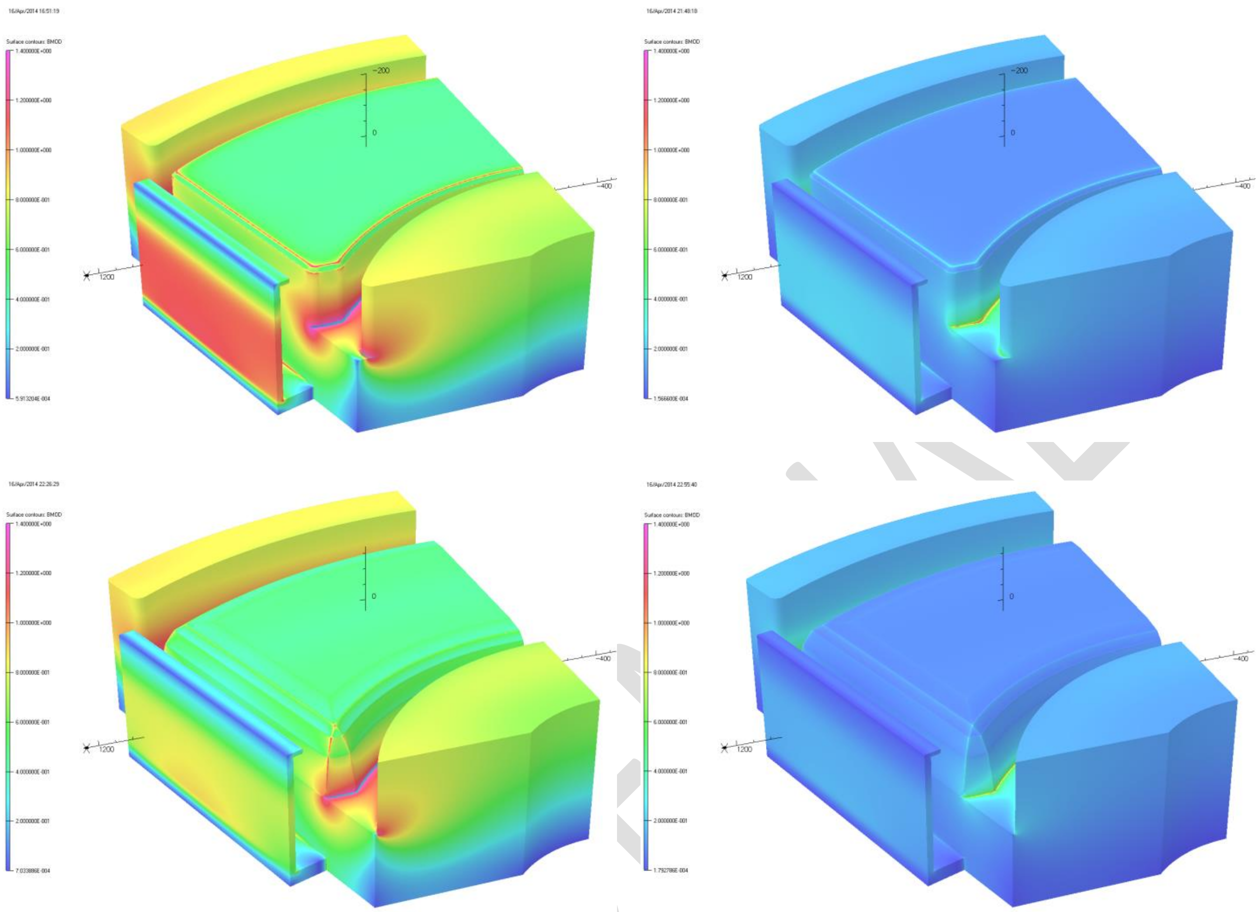

Figure 45: Iron field of the nominal (top) and Rogowski (bottom) for the high (left) and low (right) current cases. Note that the Rogowski geometry has a wider pole.

9.7 Purcell-like filter

A Purcell filter is a μ_r=1 region (air for example) in the pole that improve the field uniformity in the pole and improves the flatness. We considered different geometries for the Purcell filter.
The full Purcell filter is represented in Figure 46. The pole is completely separated from the pole base with a uniform air gap. This solution requires a wider pole to reduce the flatness value. The results plotted in Figure 47 are obtained with a 900 mm pole width. Still the flatness doesn't meet the goal.

The partial Purcell filter is represented in Figure 48. In an attempt to increase the field for the external trajectories, we add legs at the extremities of the pole that rest on the pole base. Even small legs increase the external field by too much as plotted in Figure 49. Additionally the iron in the small legs is saturated.

The outboard Purcell filter is represented in Figure 50. The pole has two rectangular slots carved at the extremities. The idea is to reduce the field for the external trajectories fields starting from the nominal case. This is successful in reducing the flatness to value close to the goal as represented in Figure 51. The radial profile of the field however is complicated. For example, the 1400-trajectory field is lower than the reference while the 1350-trajectory is higher. The next geometry tries to address this issue.

The windows Purcell filter is represented in Figure 52. This filter has two air windows inside the pole. The position and dimensions are optimized to control the strength of different fields at different geometric trajectories. The result as represented in Figure 53 is not satisfactory. Even though it is possible to control the fields to some extent, the radial profile still present anomalies.
The final approach reconsiders the full Purcell filter and tries to increase the external fields without overshooting and saturating the iron like in the partial Purcell filter.

The detached partial Purcell filter is represented in Figure 54. The geometry of the pole is like the partial Purcell but the pole is now detached from the pole base. The idea is that the legs are closer to the pole base than the rest of the filter and therefore the field at the extremity is higher. The result plotted in Figure 55 meets the field flatness goal (better than $2.5 \cdot 10^{-5}$).

CONFIDENTIAL

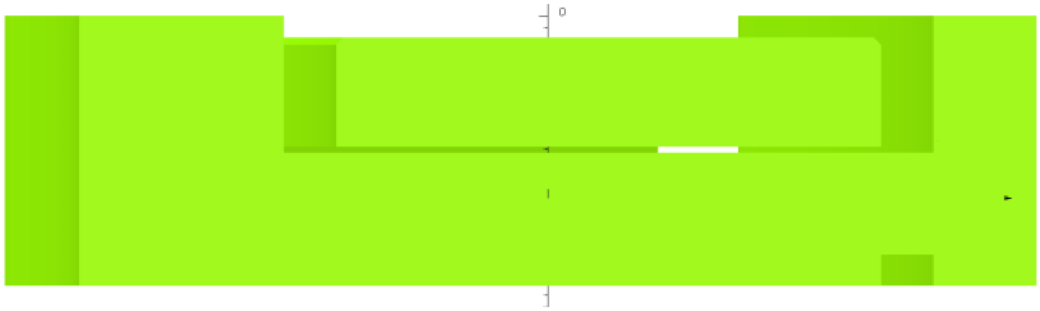

Figure 46: Full Purcell filter. The pole is completely separated by the pole base with a uniform air gap.

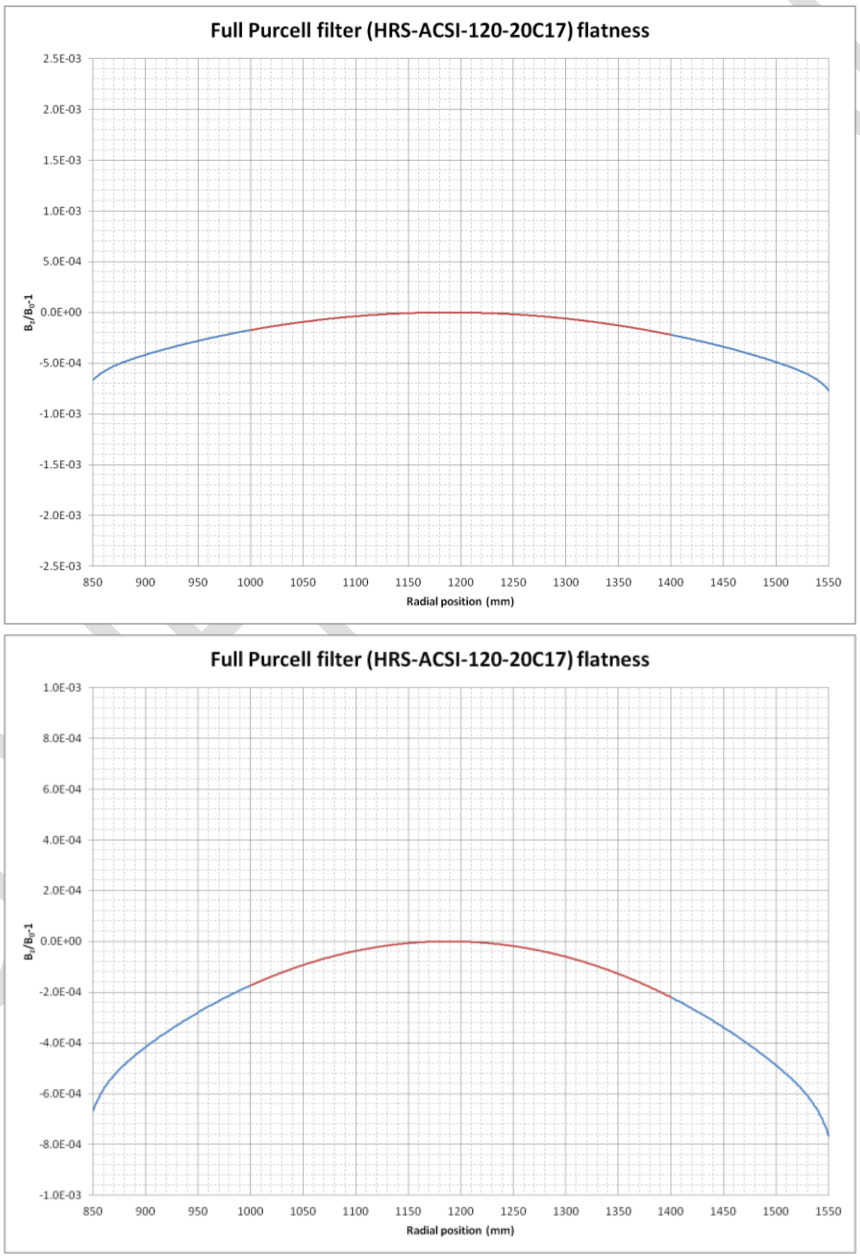

Figure 47: Full Purcell filter flatness (top full scale, bottom zoomed in).

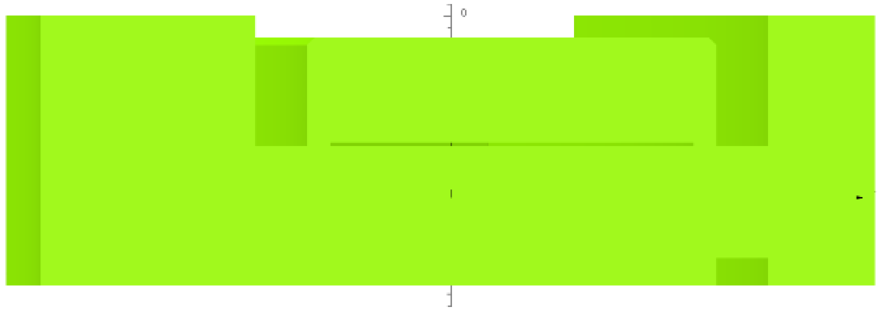

Figure 48: Partial Purcell filter. The pole has legs at the extremities that rest on the pole base.

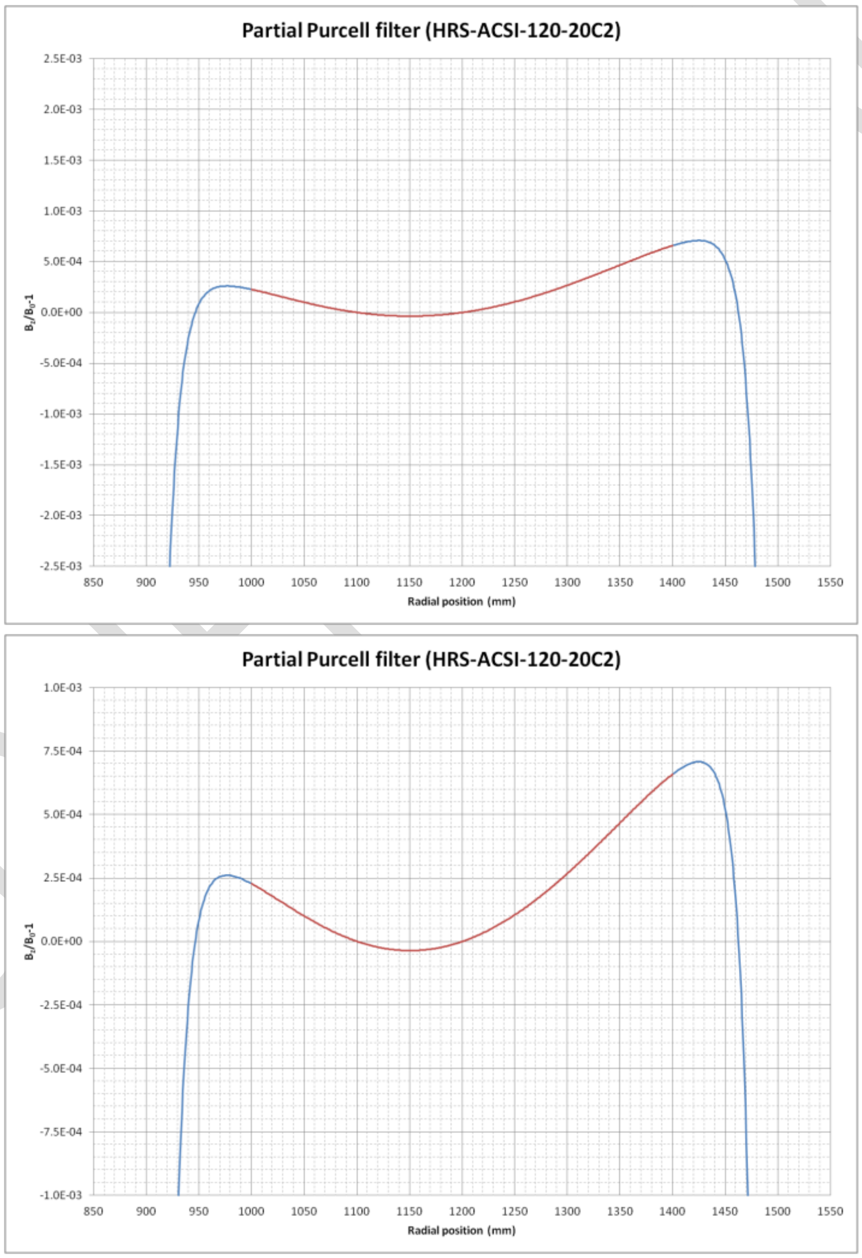

Figure 49: Partial Purcell filter flatness (top full scale, bottom zoomed in).

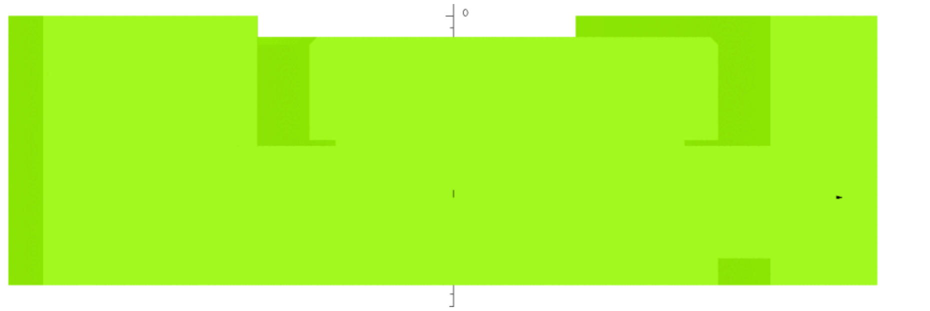

Figure 50: Outboard Purcell filter. The pole has two rectangular slots carved at the extremities.

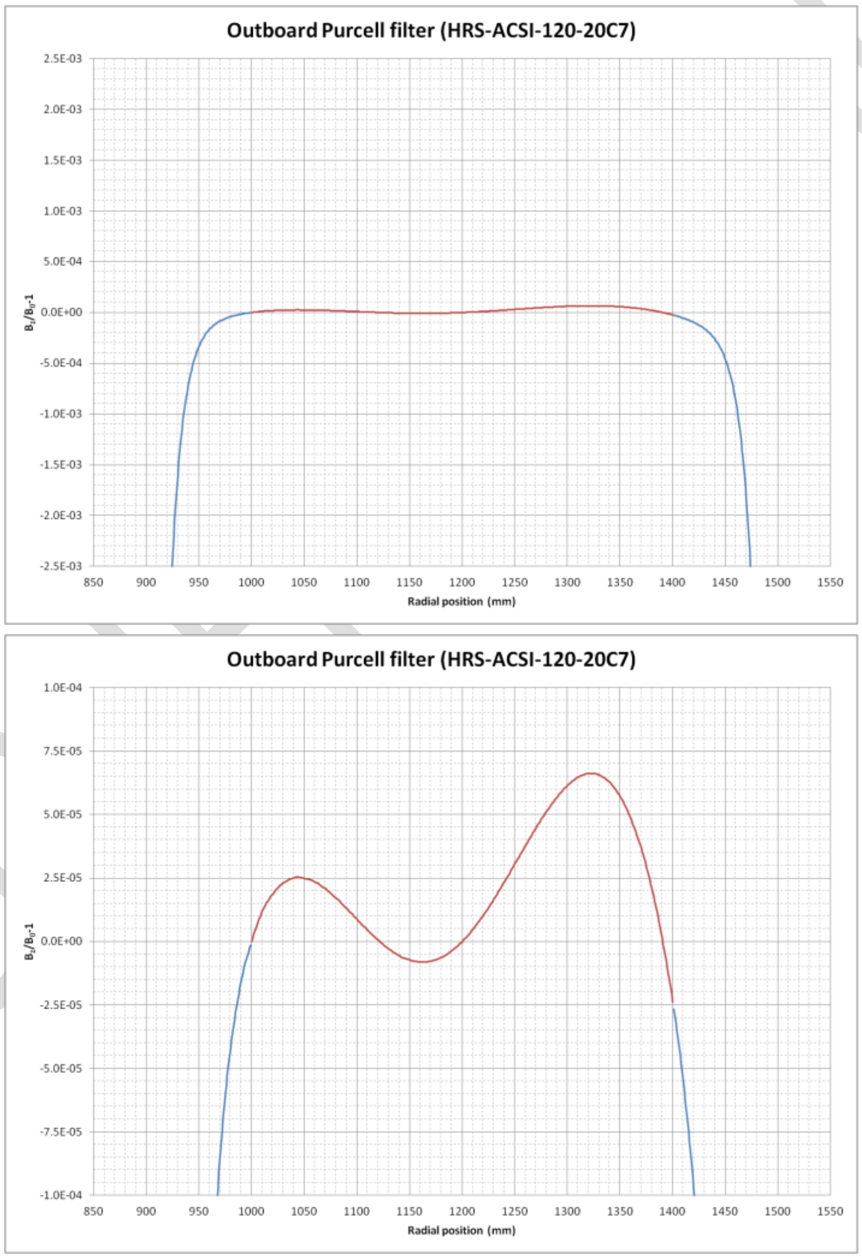

Figure 51: Outboard Purcell filter flatness (top full scale, bottom zoomed).

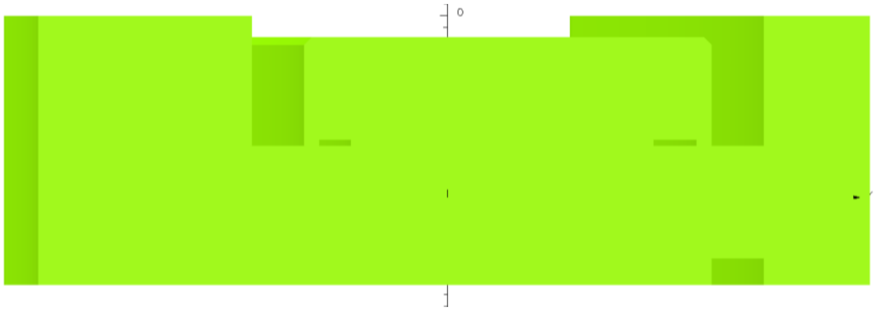

Figure 52: The windows Purcell filter.

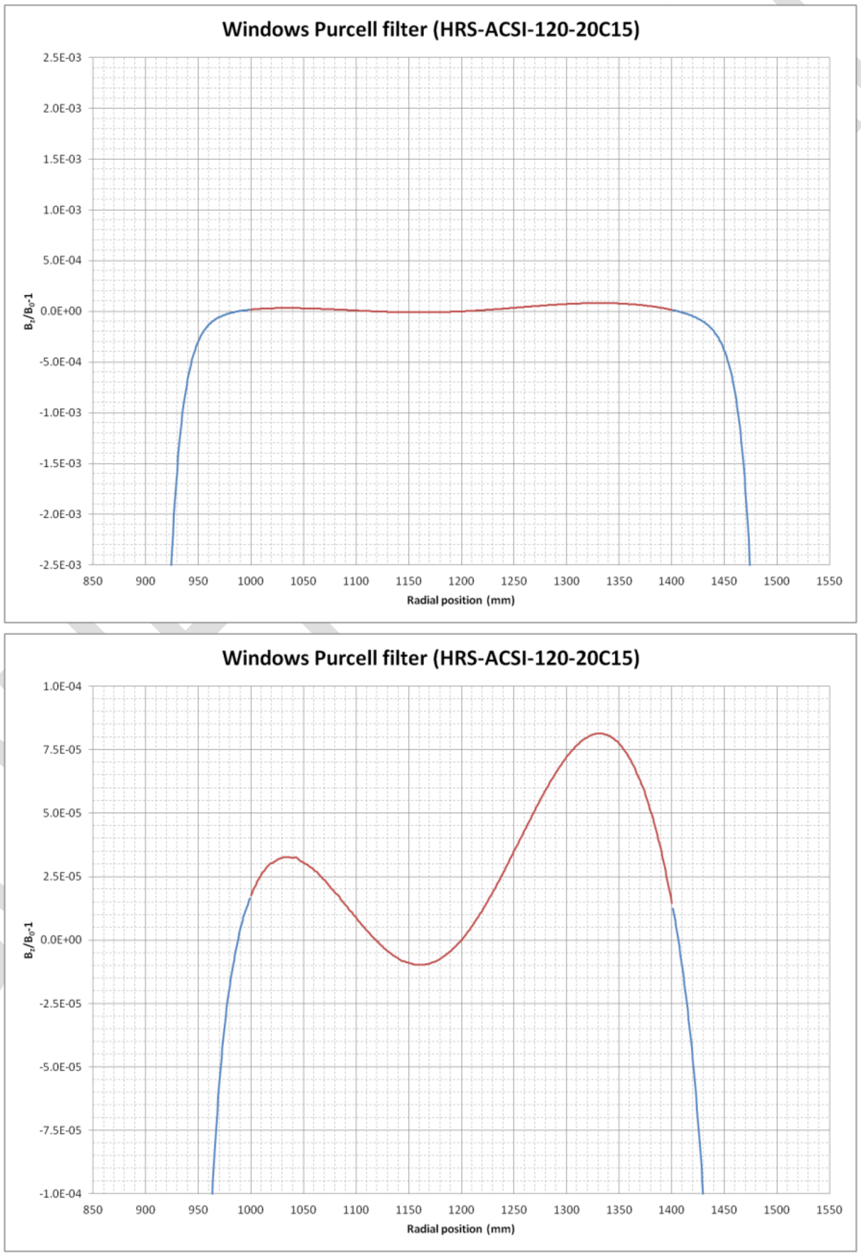

Figure 53: Windows Purcell filter flatness (top full scale, bottom zoomed).

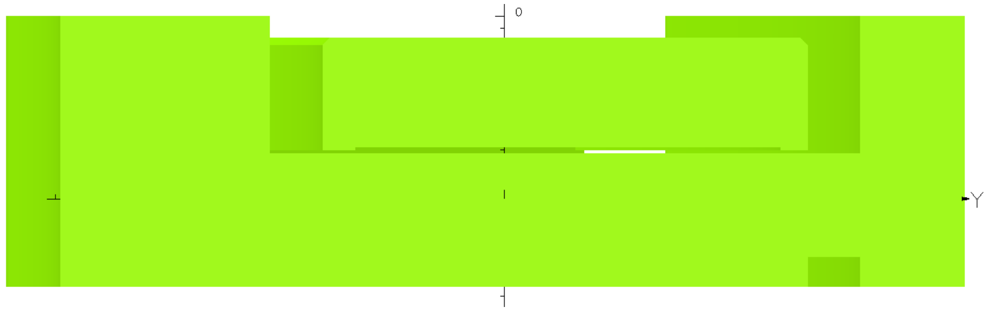

Figure 54: Detached partial Purcell filter.

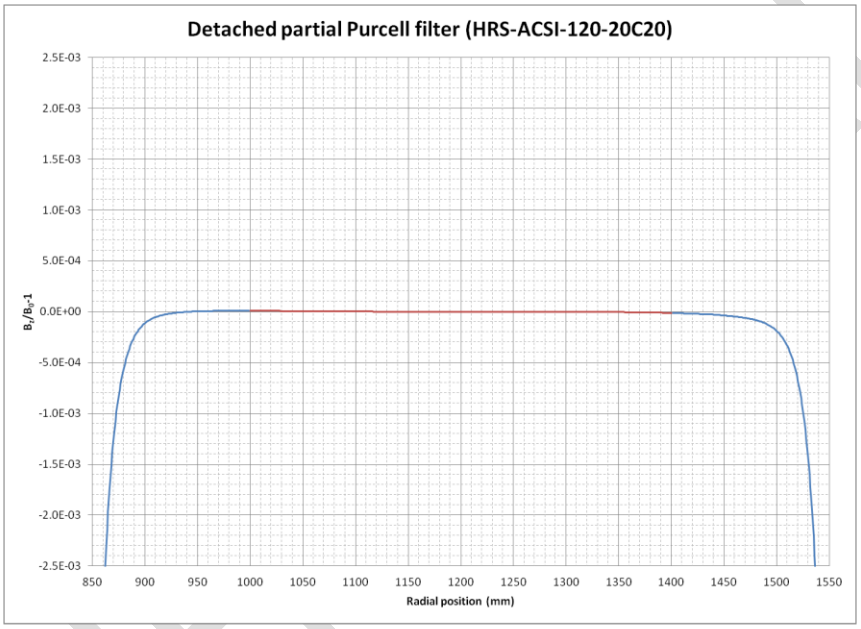

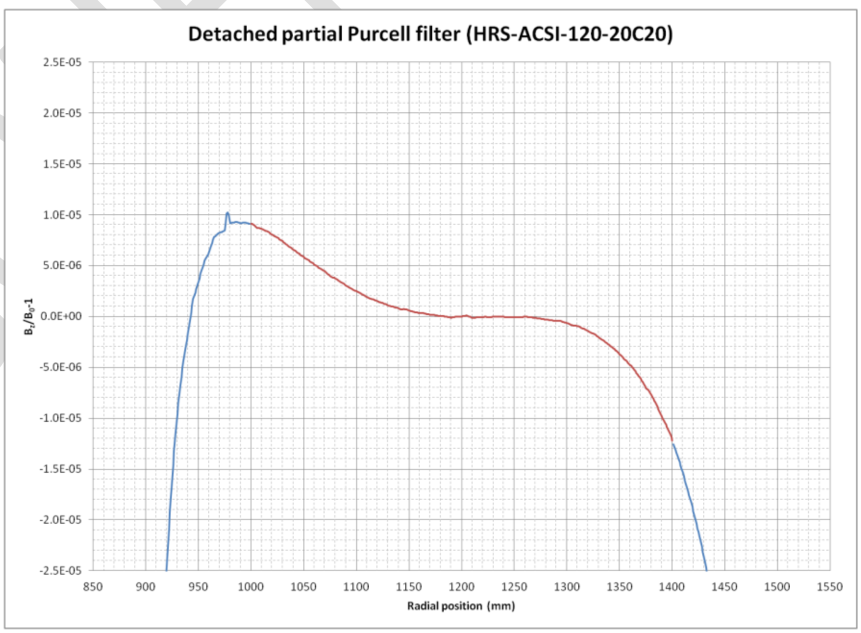

Figure 55: Detached partial Purcell filter flatness (top full scale, bottom zoomed in) within the goal of $2.5 \cdot 10^{-5}$.

9.8 Straight edge dipole optimization

All the previous considerations are implemented in the optimization of the straight edge model. This optimized dipole will serve as the base to obtain the final design that has curved entrance and exit edges.

Figure 56 is a rendering of the optimized straight edge case. The picture shows the iron magnetic flux distribution.

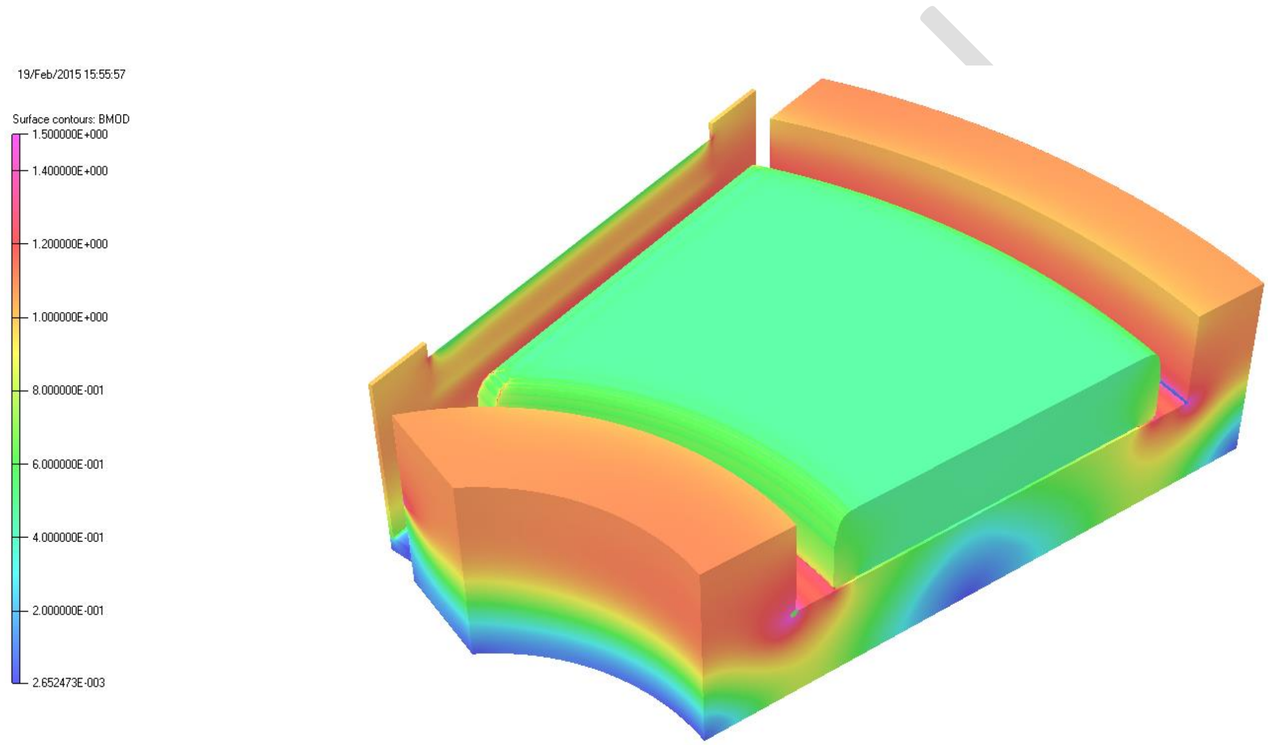

Figure 56: Optimized straight edge design.

The equalization of the return yokes is achieved using the second method explained in paragraph 9.2.

A Rogowski-like profile for both the longitudinal and transverse edges of the pole is implemented.

This profile is a scaled version of the theoretical Rogowski profile for a 70 mm gap being approximated by a six sectors segmented line as represented in Figure 57. The six sectors choice is the best compromise between approximation to the theoretical curve and minimization of the number of sector based on machining consideration. Figure 58 represents a comparison between approximation of the curve using 4, 6, 8 and 10 sectors.

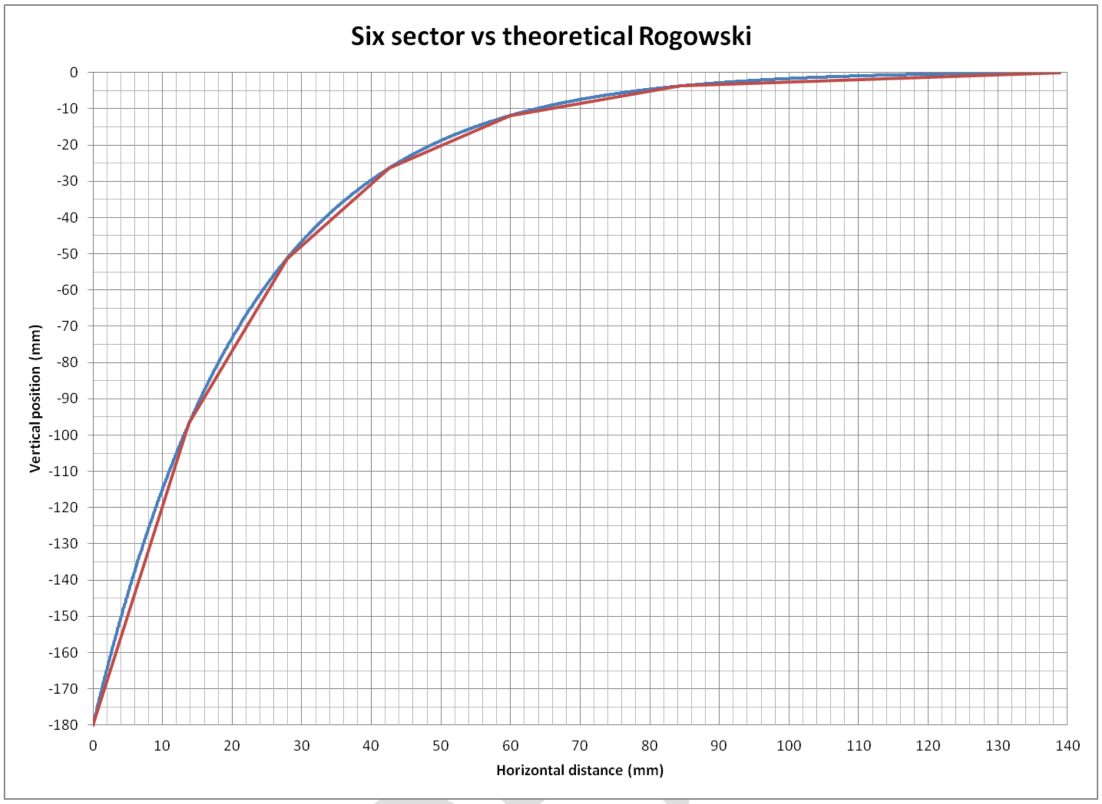

Figure 57: Six sector segmented line versus theoretical Rogowski profile for a 70 mm gap.

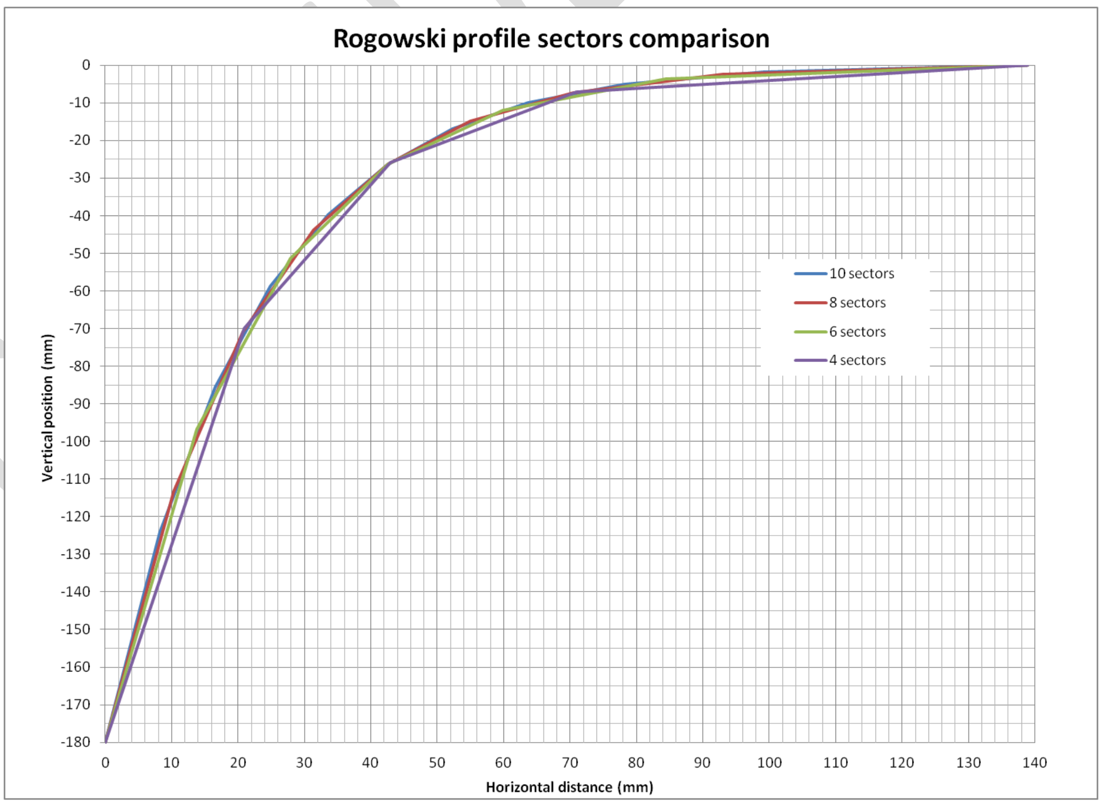

Figure 58: Comparison between different number of sectors for the segmented line.

The model has the detached partial Purcell filter (as Figure 54). The radial flatness due to the implementation of the filter is represented in Figure 59.

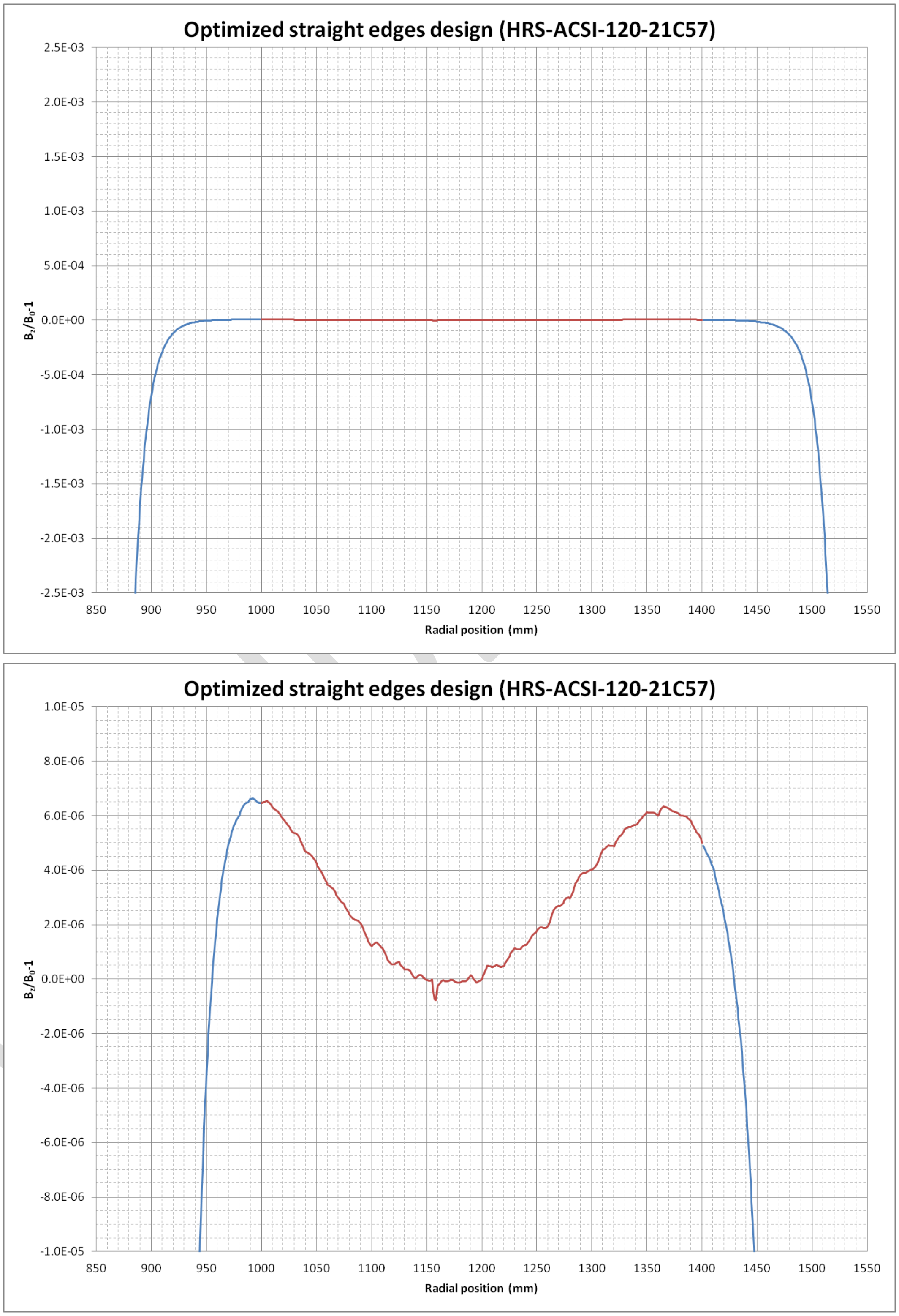

Figure 59: Field flatness of the optimized straight model (top full scale, bottom zoomed).

The field clamps are design to optimize the fringe field outside the magnet. The optimization criteria are:

1. Fringe field distance from the magnet to be minimized. This is to avoid the field profile being conditioned by other beam line or surrounding elements.
2. Field profile to minimize the first derivative of the field (sharp change in the profile). High first derivative contributes to high order aberration.
3. Avoid saturation of the field clamp (magnetic flux greater than 1.5T). This is in order to guarantee that the field clamp maintains the same behaviour at different excitation level.

Different configurations are considered and the effect of each of them are plotted in Figure 60; in the plot the distance of 120 mm corresponds to the mechanical edge of the field clamp.

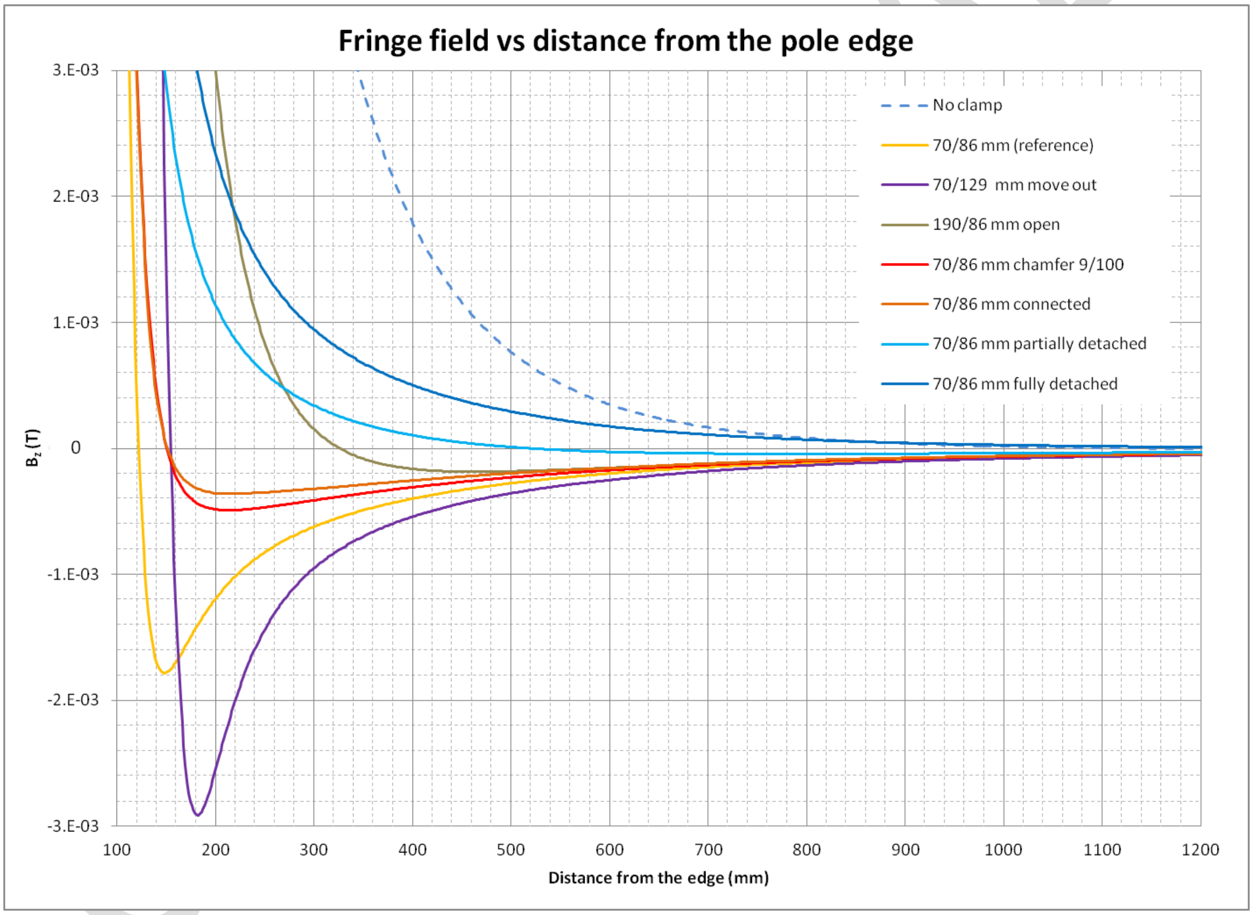

Figure 60: Fringe field profiles of different field clamp configuration. The mechanical edge of the clamp coincides with the 120 mm distance.

These configurations include:

1. <u>No clamp</u>: in this case the field fall off smoothly but it extend way beyond the edge of the magnet

2. 70/86 mm: these two numbers refer to the clamp aperture (70 mm, same as the pole gap) and distance from the pole edge (86 mm). In this case the clamp has a simple L shape. The fall off relative to this configuration has a significant overshooting on the negative side and a sharp change in the field profile.
3. 70/129 mm move out: in order to remove the overshooting and smooth the fall off we consider a configuration where the clamp distance is increased (129 mm) while maintaining the same aperture (70 mm). The result goes in the opposite direction of the goal.
4. 190/86 mm open: increasing the aperture (190 mm) while preserving the distance (86 mm) make the fall off smoother but move outward the fringe field.
5. 70/86 mm chamfer 9/100: applying a chamfer on the edge effectively reduced the efficiency of the field clamp.
6. 70/86 mm connected: connecting the lower and upper field clamp create a path for the magnetic flux that also results in a weaker field through the gap.
7. 70/86 mm partially detached: inserting an opening (filter like) where the clamp is connected to the base of the magnets generated a smooth fringe field while maintaining the fringe field close to the magnet.
8. 70/86 mm fully detached: a clamp non-magnetically connected to the dipole results in the fringe field to move away from the magnet.

The final design is represented in Figure 61. The clamp has an aperture equal to the pole gap and a minimum distance from the edge that allows for the coil accommodation. The edge has a chamfer and the lower and upper clamp are connected. Finally the clamp has a filter like windows (clamp to yoke windows) where it attaches to the base of the magnet.

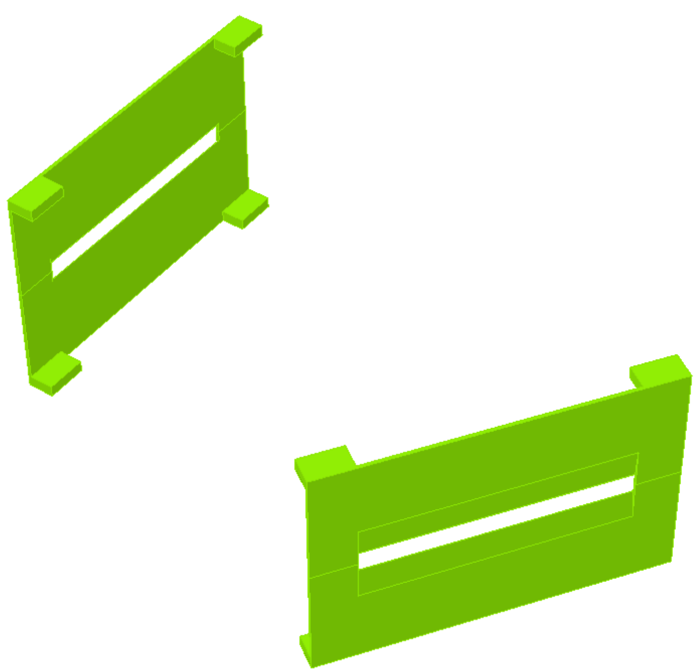

Figure 61: Field clamps design for the straight edge model.

CONFIDENTIAL

The effective field edge profile of the optimized straight edge case is represented in Figure 62. In the plot the red line represents the hard edge profile while the green one references the central trajectory. The integral field flatness is represented in Figure 63.

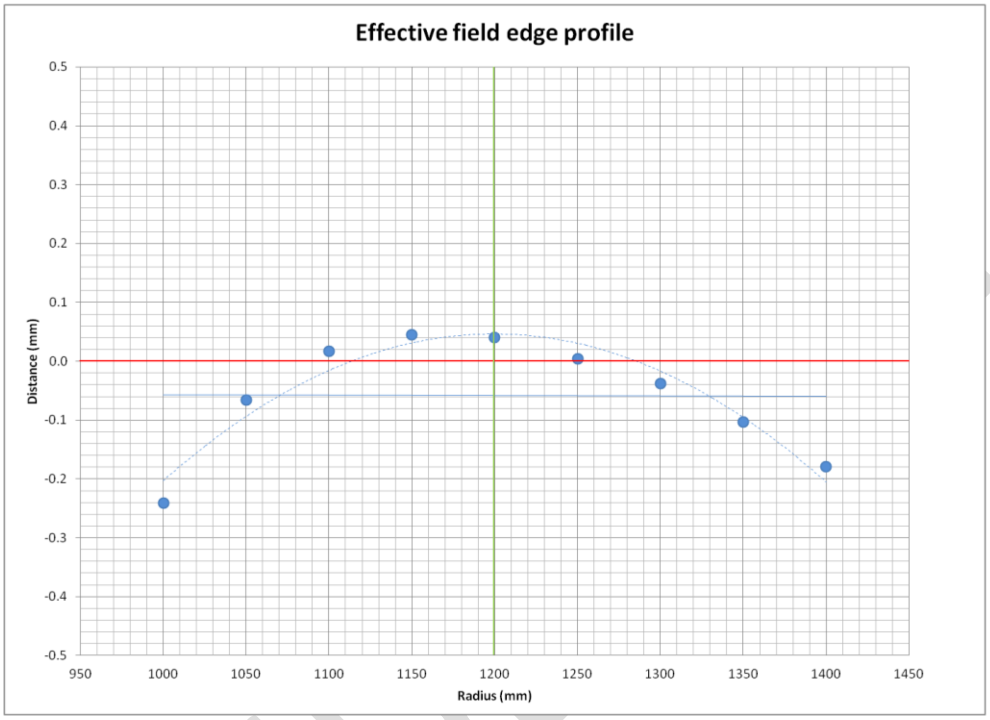

Figure 62: Effective field edge profile of the optimized straight edge case. The red line represents the hard edge case. The green line is the reference.

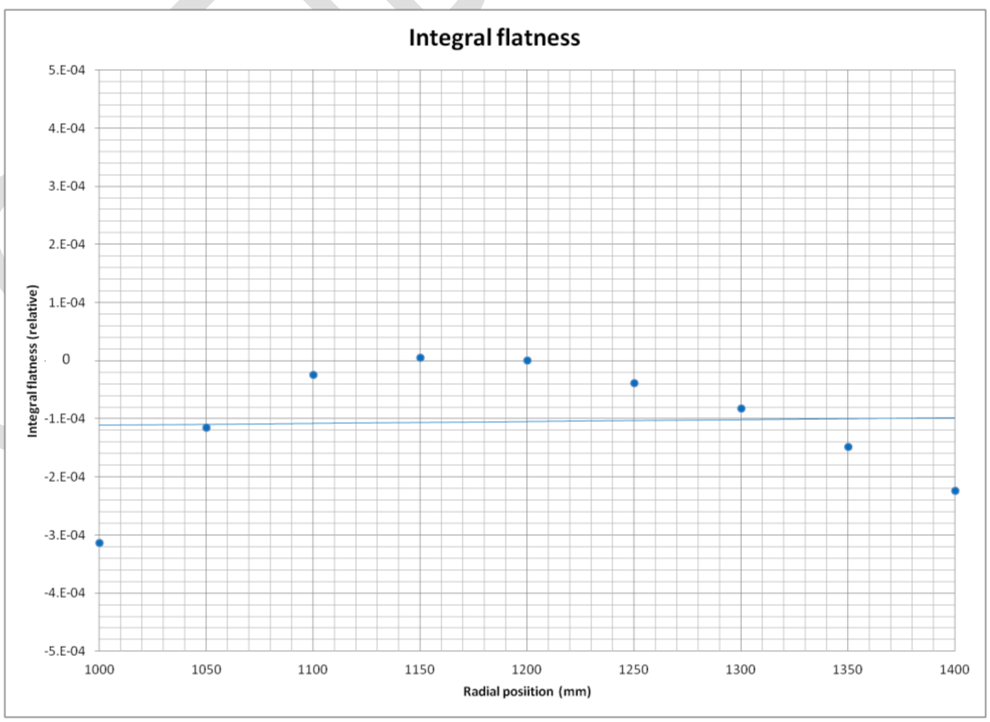

Figure 63: Integral field flatness of the optimized straight edge dipole.

9.9 Final design

The final design is obtained by applying a curvature to both the pole entrance and exit face and the field clamp. The final result is represented in Figure 64. The coil follows all the curvature of the pole.

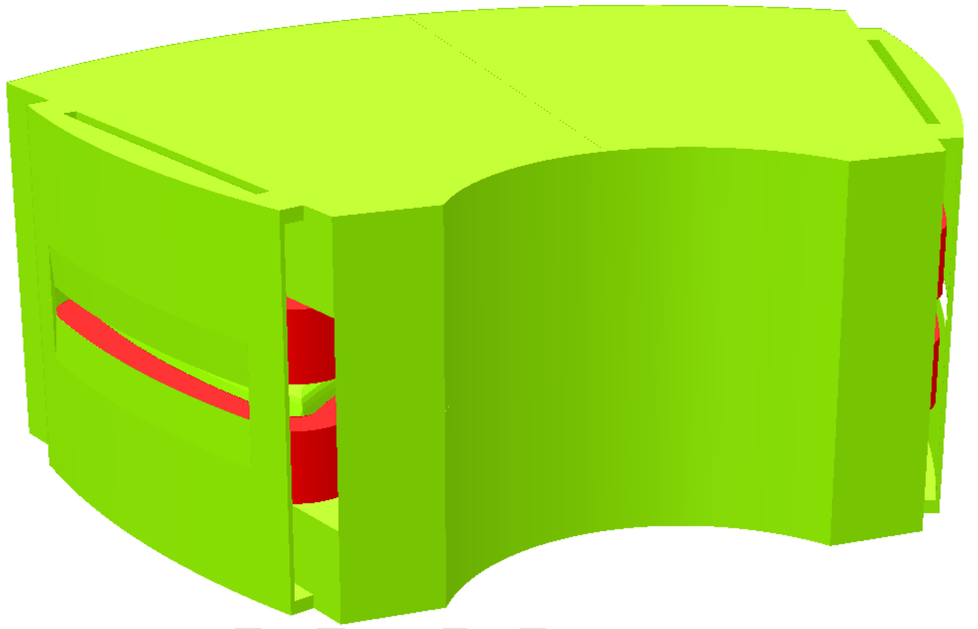

Figure 64: Final design (HRS-120-23C62).

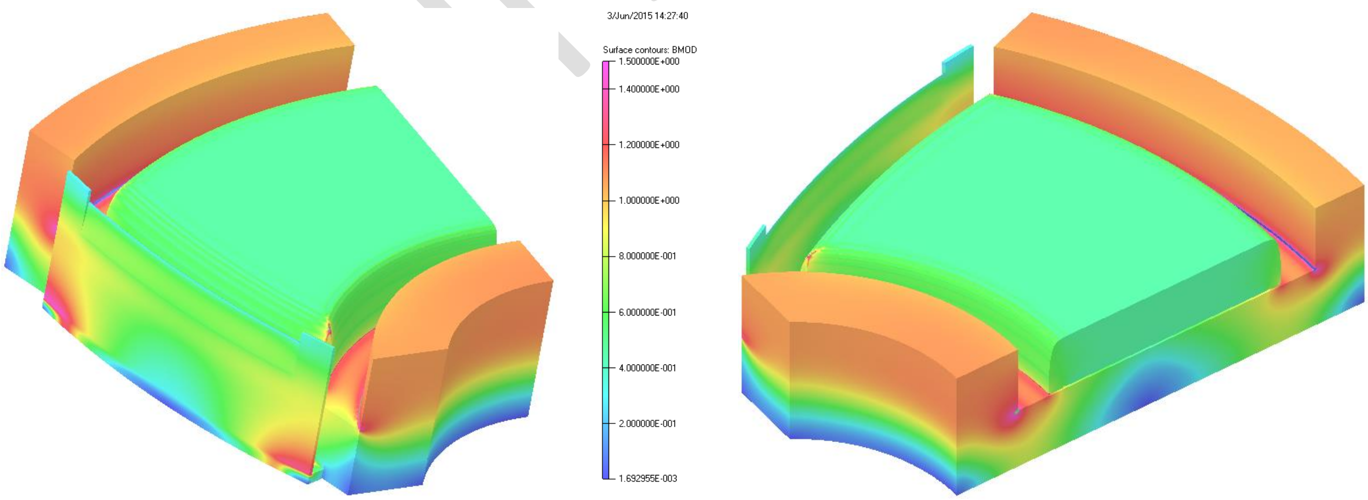

Figure 65: Magnetic flux distribution in the final model.

The following Table 7 contains the main parameters of the final design. Notice that the final mechanical dimensions of the dipole (necessary for production drawings) are listed in Table 11 and refer to the final engineered design (see paragraph 10).

Table 7: Main Parameters of the Final Design (for final mechanical dimensions see Table 11). These Parameters refer to the OPERA Model HRS-120-23C62.

Parameter	**Value**	**Note**
Reference radius	1200 mm	
Bending angle	90 degree	
Entrance and exit face angle	26.56 degree	effective
Geometric entrance and exit angle	26.77 degree	machined into steel
Edge radius of curvature	2237.9 mm	effective
Geometric edge radius of curvature	2227.0[7] mm	machined into steel
Pole gap	70.0 mm	total
Pole width	760 mm	±380 mm around the reference radius
Pole height (maximum)	185 mm	minimum of 183.2 mm
Pole blend radius	31.5 mm	applied after the Rogowski
Purcell filter maximum height	6.8 mm	maximum from the return yoke base
Purcell filter minimum height	5.0 mm	at legs location
External Purcell filter leg width	40.0 mm	
Internal Purcell filter leg width	50.0 mm	
External return yoke width	160 mm	
External return yoke height	225 mm	
Internal return yoke width	199 mm	
Internal return yoke height	225 mm	
Return yoke base height	205 mm	
Internal coil channel	100 mm	

[7] If (0,0) is the origin of the coordinate system where the center of the magnet is (0,1200) then the center of the entrance geometric edge radius of curvature is (1266.6951, 1545.2056). The center of the exit radius is of course (-1266.6951, 1545.2056).

CONFIDENTIAL

Table 7: Main Parameters of the Final Design (for final mechanical dimensions see Table 11). These Parameters refer to the OPERA Model HRS-120-23C62.

Parameter	Value	Note
External coil channel	110 mm	to accommodate coil transition
Field clamp width	1000 mm	±500 mm around the reference radius
Field clamp thickness	10 mm	
Field clamp aperture	70.0 mm	same as the pole gap
Field clamp chamfer dimensions	9 mm × 100 mm	
Field clamp connector width	100 mm	
Field clamp to yoke window width	760 mm	±380 mm around the reference radius
Field clamp to yoke window depth	30 mm	
Coil width	80 mm	see paragraph 10 for final engineered dimensions
Coil height	158 mm	
Current density	1.228 A/mm^2	this is the value used in OPERA
Coil distance from the iron	9 mm	this is the minimum distance
Coil minimum bend radius	40.5 mm	

CONFIDENTIAL

The six sectors profile of the final design is represented in Figure 66. The intersection point values together with the scaling factors for the longitudinal and transverse profiles are listed in Table 8.

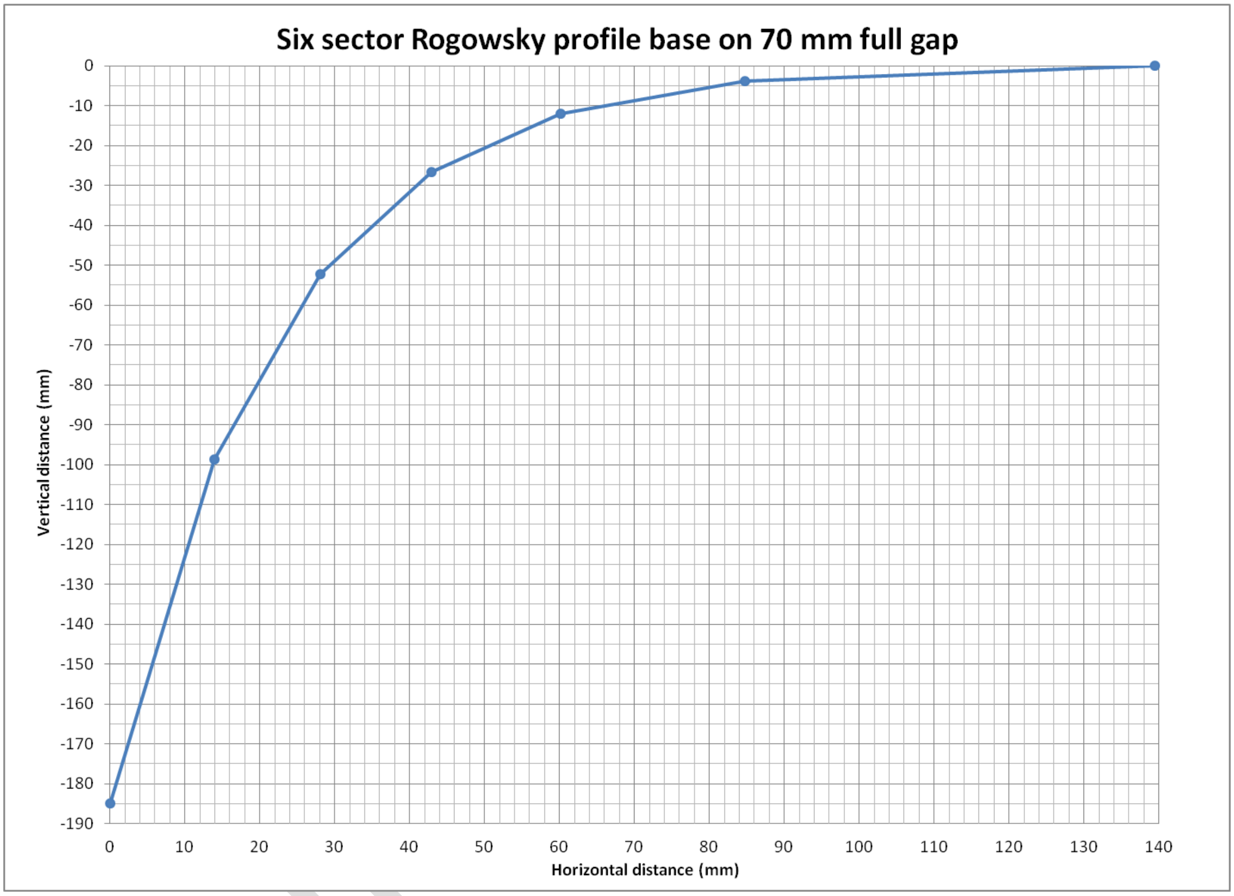

Figure 66: Six sectors segmented line for the final design.

Table 8: Intersection Point of the Six Sectors Rogowski Profile (final design)

Full Rogowski Horizontal distance (mm)	Full Rogowski Vertical distance (mm)	Scaling factor for the longitudinal profile (entrance and exit pole faces)		Scaling factor for the transverse profile	
		Horizontal	Vertical	Horizontal	Vertical
139.44	0				
84.77	-3.77				
60.2	-12.06				
42.91	-26.61	0.6573	0.6573	0.4	0.6573
28.07	-52.13				
13.90	-98.64				
0	-185				

The fringe field profile (green curve) is represented in Figure 67. The profile is graphed against other cases (already reported in Figure 60) for comparison.

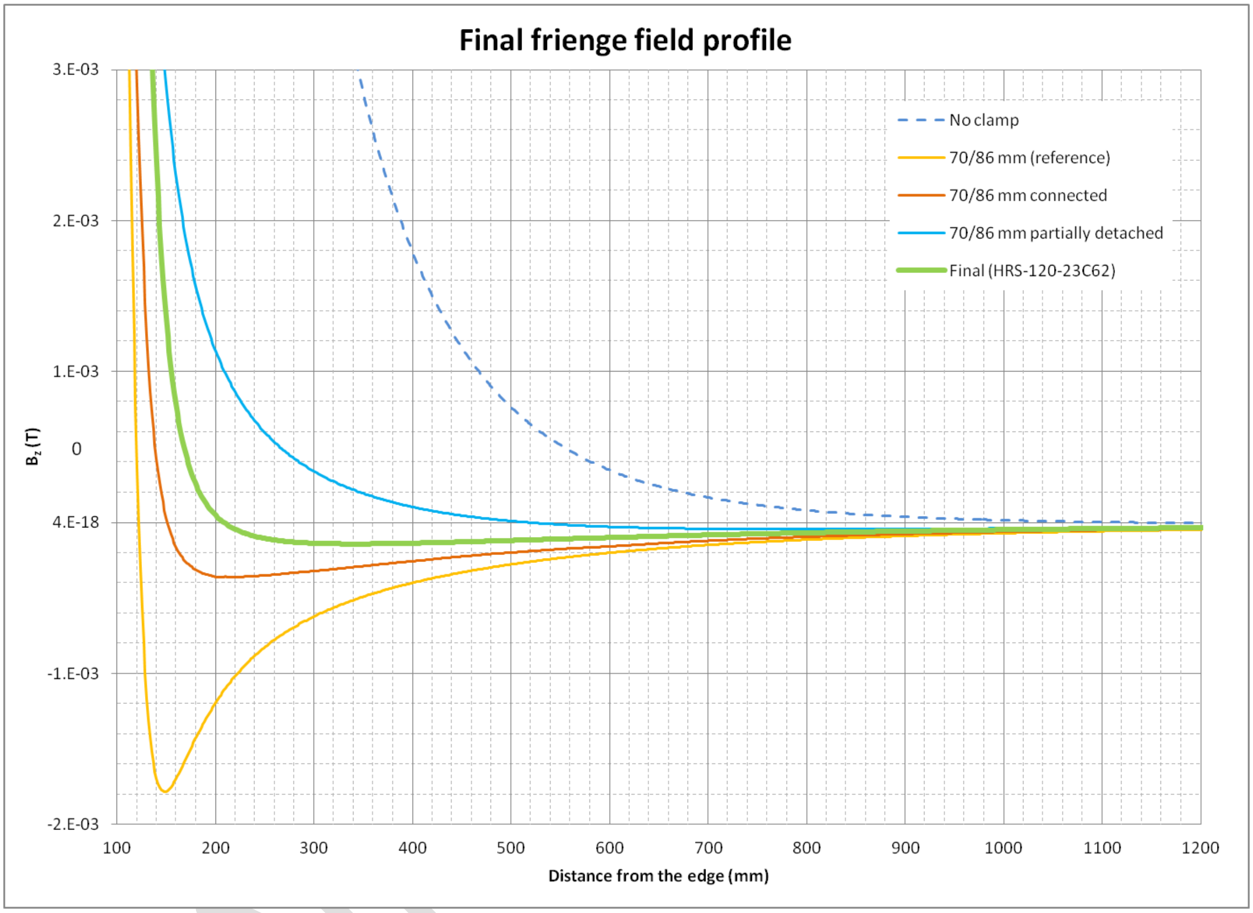

Figure 67: Fringe field profile (green curve) of the final design.

CON

The field flatness of the final design is represented in Figure 68. It meets the requirement of better than $2.5 \cdot 10^{-5}$.

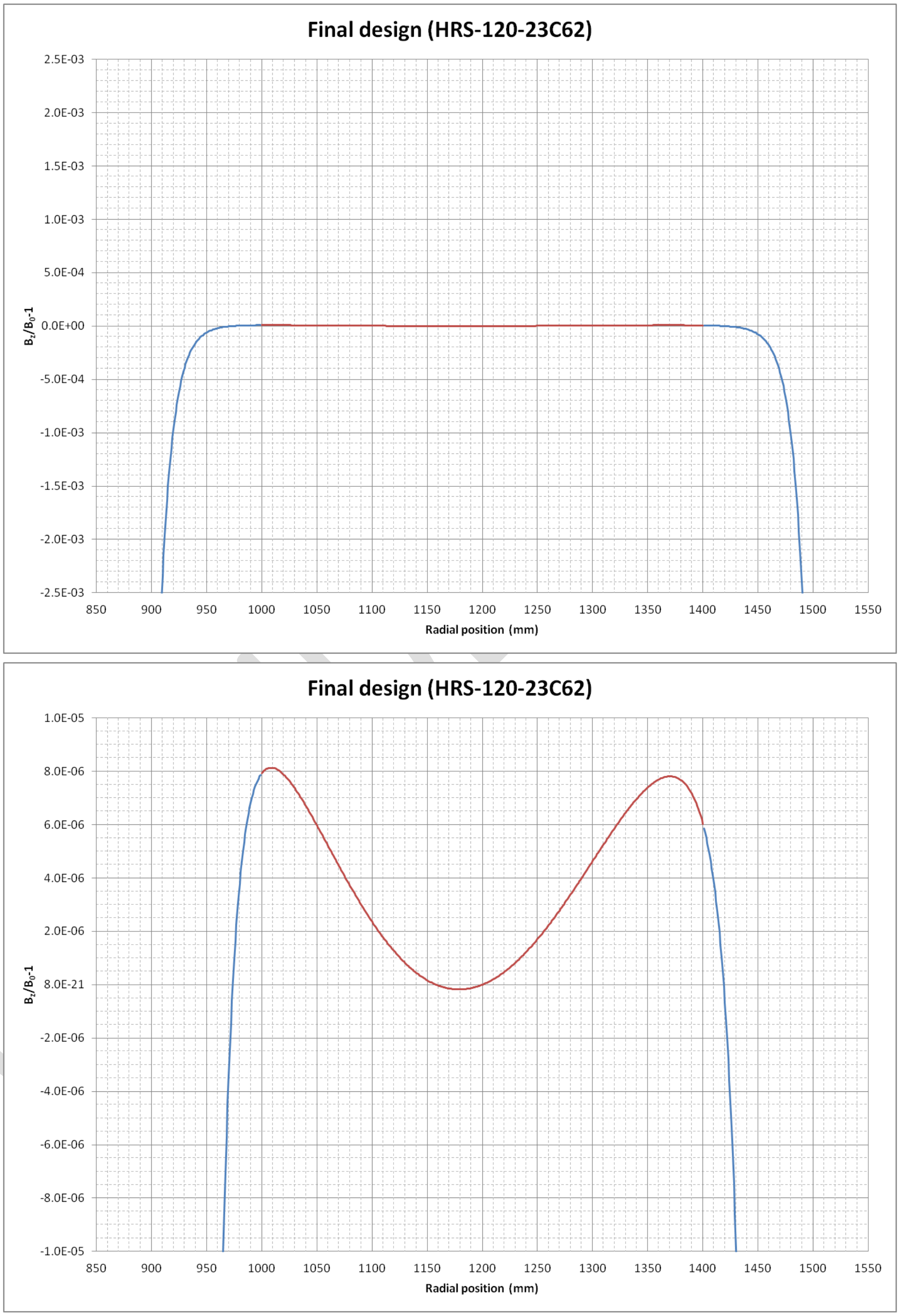

Figure 68: Field flatness of the final design (top full scale, bottom zoomed).

The effective field edge profile and the integrated flatness are plotted respectively in Figure 69 and Figure 70. In both cases the requirements are met. The red box in Figure 70 represents the integral flatness requirement. Integral values for the hard-edge case and the OPERA model are listed in Table 9.

Table 9: Field Integrals for the Hard edge and OPERA Models for the final Design (HRS-120-23C62)

Geometric trajectory	**Hard-edge integral (T mm)**	**OPERA integral (T mm)**	$IR_{\rho} - 1$	$Integral\ flatness$
1000 mm	802.195	802.147	-6.0E-05	-6.2E-05
1050 mm	819.383	819.382	-1.5E-06	-3.6E-06
1100 mm	835.414	835.417	4.4E-06	2.2E-06
1150 mm	850.275	850.282	8.7E-06	6.5E-06
1200 mm (reference)	863.955	863.957	2.2E-06	0.0E+00
1250 mm	876.443	876.448	5.2E-06	3.1E-06
1300 mm	887.727	887.731	4.4E-06	2.2E-06
1350 mm	897.796	897.798	1.8E-06	-4.0E-07
1400 mm	906.637	906.636	-1.4E-06	-3.6E-06

CONFIDENTIAL

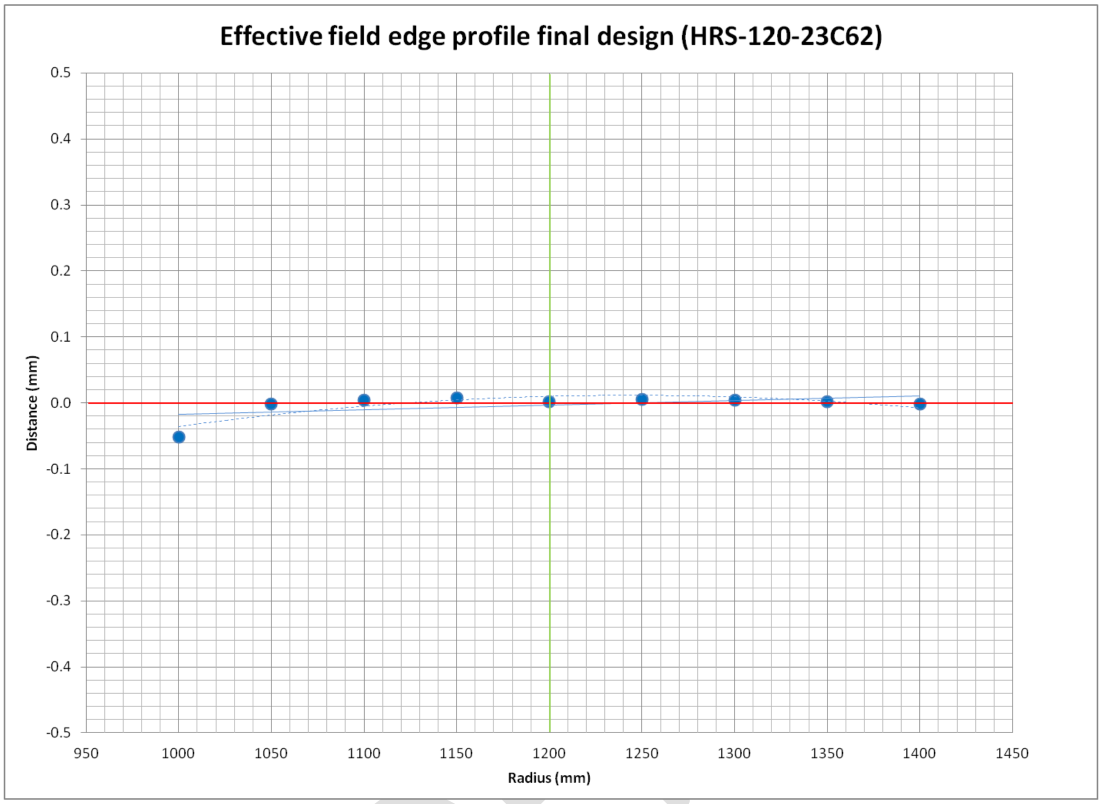

Figure 69. Effective field edge profile for the final design.

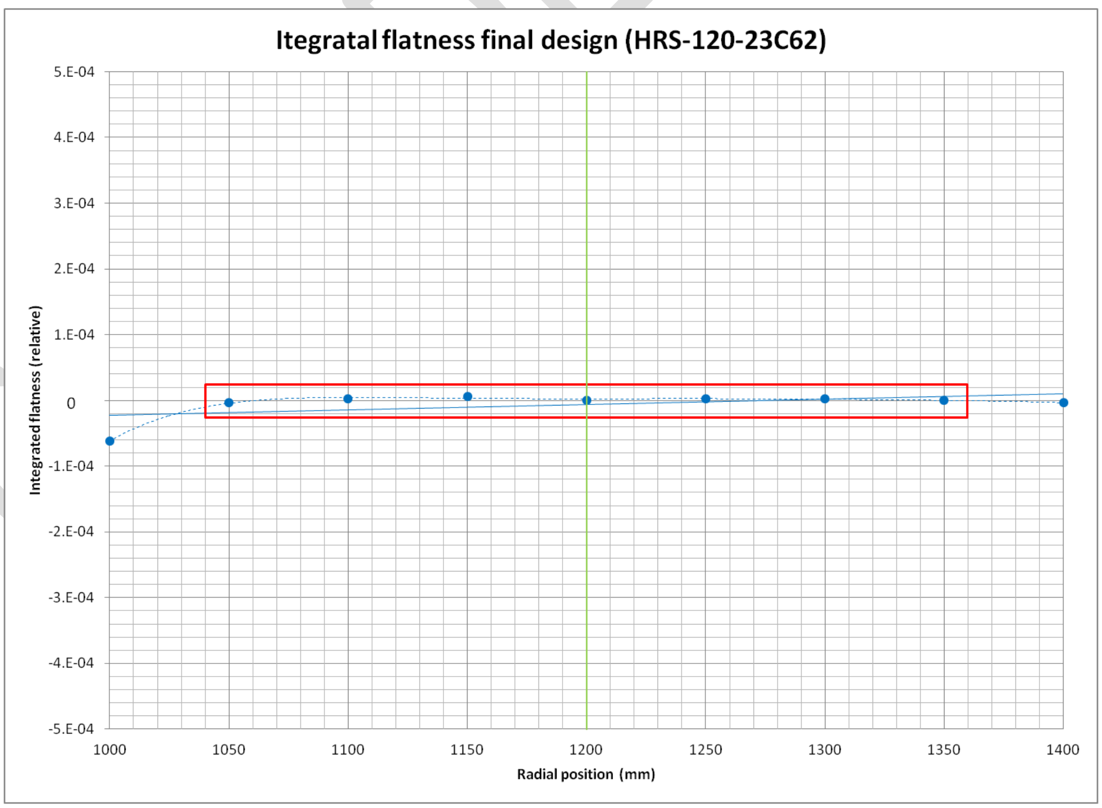

Figure 70: Integrated flatness for the final design. The red box represents the requirement that the integral flatness is $2.5 \cdot 10^{-5}$ or better within the good field region.

We run the final model at low excitation[8] corresponding to 0.098 T (B_z) at the center of the magnet (0,1200) compared with 0.458 T of the full excitation case (HRS-120-23C62). Figure 71 is a rendering of the flux distribution for this low excitation case.

Both the field flatness (Figure 72) and the integral flatness (Figure 73) requirements are met in the low excitation case, as well as the $\left|IR_\rho - 1\right|$. This last quantity is related to the effective field edge profile (Figure 74) that moved not significantly (less than 0.05 mm), with respect to the high excitation case.

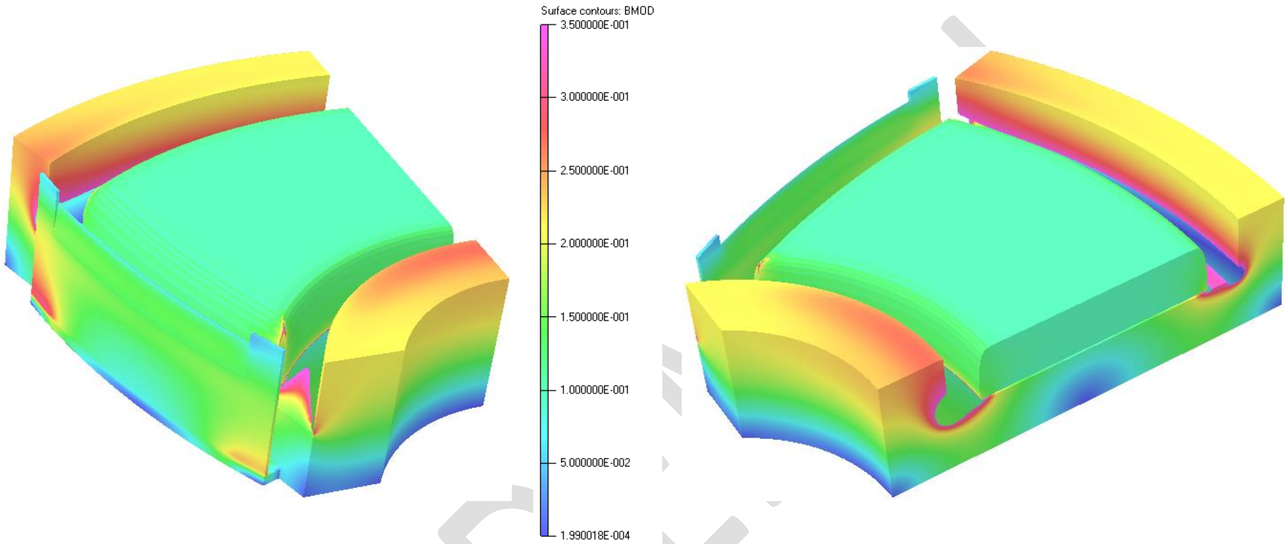

Figure 71: Magnetic flux distribution in the final model run at low excitation (simulation HRS-120-23C65); note the change of scale with respect to the final design at full excitation.

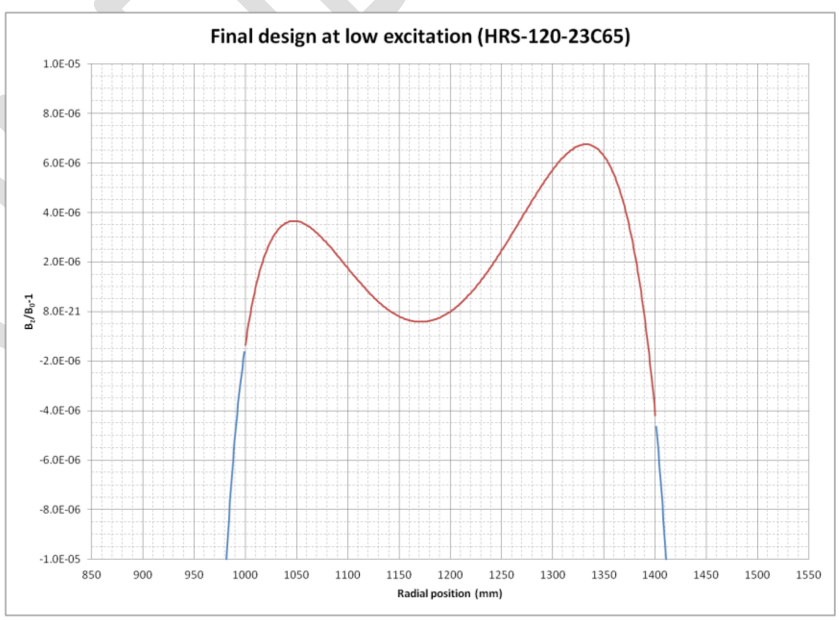

Figure 72: Field flatness of the final design in the low excitation case.

---

[8] This is to bend mass 11 at 60 kV. This mass is chosen since ^{11}Li is TRIUMF flagship radioactive beam. It should be noted though that at his low masses a resolving power of 20000 is not necessary.

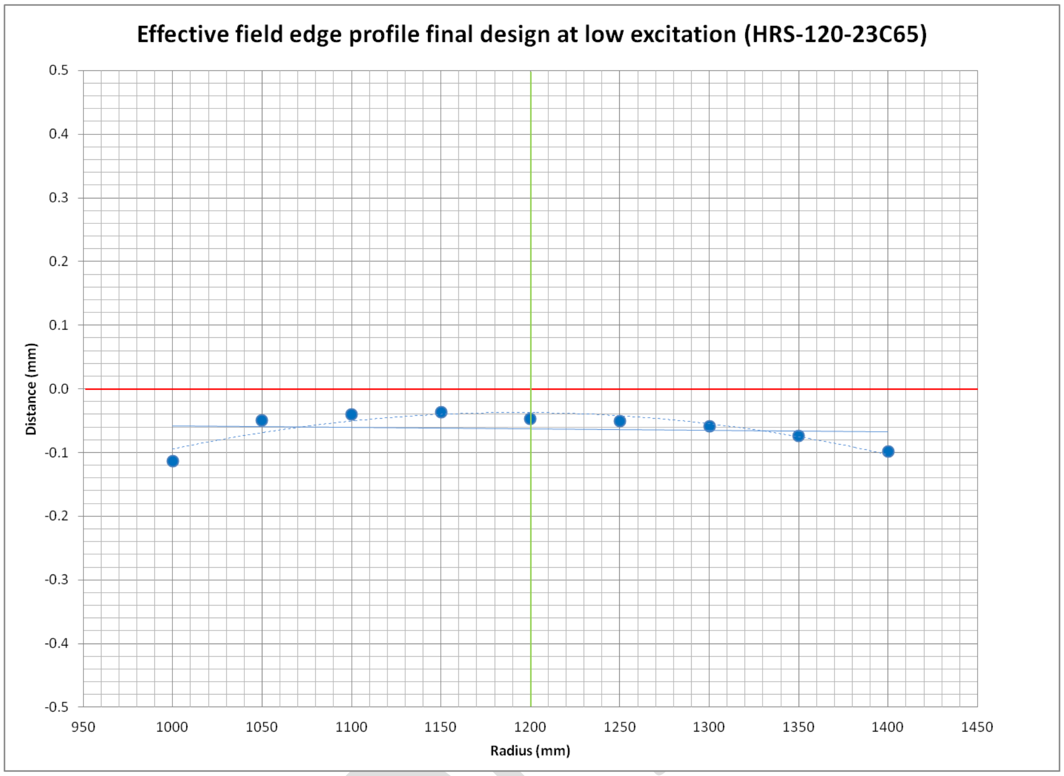

Figure 73: Integral flatness of the final design in the low excitation case.

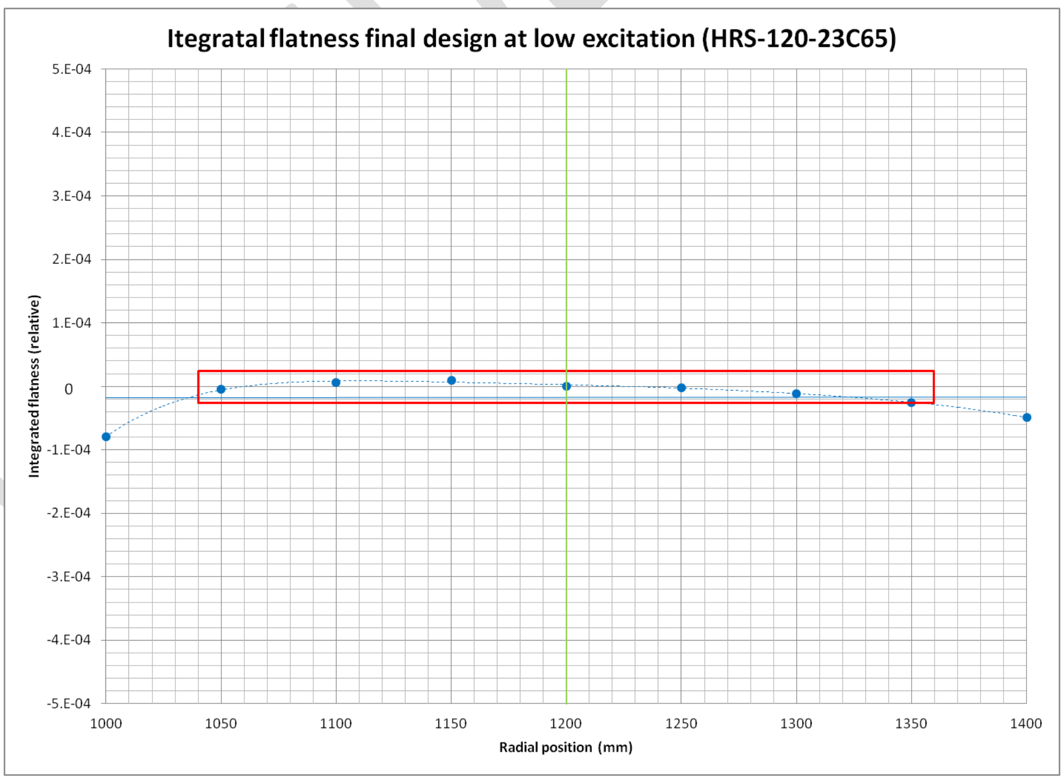

Figure 74: Effective field edge profile for the final design in the low excitation case.

10 Final Engineered Design

In this paragraph all the engineering features required to assemble, transport and operate the magnet in OPERA are simulated. The features are applied to the final design (HRA-120-23C62) and listed in Table 10. The results of the simulations are compared to the final design with respect to integral field flatness and effective field position.

Each feature is simulated cumulatively following the same order of Table 10. All the features are simulated as air (voids in the steel); in one case air has been substituted with stainless steel (with μ_r=2) showing no difference in the final result.

Table 10: Engineering Details Simulated in OPERA.

Proposed engineering feature	**OPERA Simulation**	**Result**	**Note**
Pole mount	HRS-120-23C62eng	acceptable	see Appendix D
Yoke mount and hoist rings	HRS-120-23C62eng2	acceptable	see Appendix F and Appendix H
Chamfer of the internal yoke	HRS-120-23C62eng3	acceptable	see Appendix J
Buckley's coil proposal	HRS-120-23C62eng4	acceptable but not adopted	163× 79 with separated pancakes
Reduced field clamp	HRS-120-23C62eng5	acceptable	see Appendix J
Field clamp mount	HRS-120-23C62eng6	acceptable	see Appendix I
Field clamp squared	HRS-120-23C62eng7	not acceptable	see Appendix I
Propose single-rib field clamp	HRS-120-23C62eng9	acceptable	alternative to squared option (see Figure 75)
Pole holes	HRS-120-23C62eng12	acceptable	see Appendix E
Field clamp connections	HRS-120-23C62eng13	acceptable	see Appendix K
5 mm blended field clamp knife edge	HRS-120-23C62eng14	acceptable	
Thermowells	HRS-120-23C62eng15	acceptable	see Appendix G
Final coil 159×76	HRS-120-23C62eng16	acceptable	see Appendix C
Move coil transition from external to internal coil channel	HRS-120-23C62eng21	acceptable	requires re-adjustment of Purcell filter, edge curvature and flux balance

CONFIDENTIAL

The parameters of the final engineered design (HRS-120-23C62eng21) are listed in Table 11, where the differences with respect to the final design are highlighted. The Rogowski profile (see Table 8) has not been changed. The final engineered design, the relative effective field and integral field flatness are represented respectively in Figure 75, Figure 77 and Figure 78.

Table 11: Main Parameters (and Final Mechanical Dimensions) of the Final Engineered Design. These Parameters refer to the OPERA Model Identified as HRS-120-23C62eng21

Parameter	Value	Note
Reference radius	1200 mm	
Bending angle	90 degree	
Entrance and exit face angle	26.56 degree	effective
Geometric entrance and exit angle	26.77 degree	machined into steel
Edge radius of curvature	2237.9 mm	effective
Geometric edge radius of curvature	2228.0[9] mm	machined into steel
Pole gap	70.0 mm	total
Pole width	760 mm	±380 mm around the reference radius
Pole blend radius	31.5 mm	applied after the Rogowski
Pole height (maximum)	185 mm	minimum of 183.2 mm
Purcell filter maximum height	6.7 mm	maximum from the return yoke base
Purcell filter minimum height	5.0 mm	at legs location
External Purcell filter leg width	45.0 mm	
Internal Purcell filter leg width	50.0 mm	
External return yoke width	160 mm	
External return yoke half-height	225 mm	
Internal return yoke width	198 mm	
Internal return yoke half-height	225 mm	
Return yoke base height	205 mm	
Internal coil channel	110 mm	to accommodate coil transition

CONFIDENTIAL

[9] If (0,0) is the origin of the coordinate system where the center of the magnet is (0,1200) then the center of the entrance geometric edge radius of curvature is (1267.6449, 1545.5185). The center of the exit radius is of course (-1267.6449, 1545.5185).

Table 11: Main Parameters (and Final Mechanical Dimensions) of the Final Engineered Design. These Parameters refer to the OPERA Model Identified as HRS-120-23C62eng21

Parameter	Value	Note
External coil channel	100 mm	
Field clamp width	970 mm	±485 mm around the reference radius
Field clamp thickness	10 mm	
Field clamp aperture	70.0 mm	same as the pole gap
Field clamp chamfer dimensions	9 mm × 100 mm	
Field clamp connector width	85 mm	
Field clamp to yoke window width	760 mm	±380 mm around the reference radius
Field clamp to yoke window depth	30 mm	
Coil width	76 mm	see Appendix C
Coil height	159 mm	
Current density	1.228 A/mm^2	this is the value used in OPERA
Coil distance from the iron	9 mm	this is the minimum distance
Coil minimum bend radius	40.5 mm	

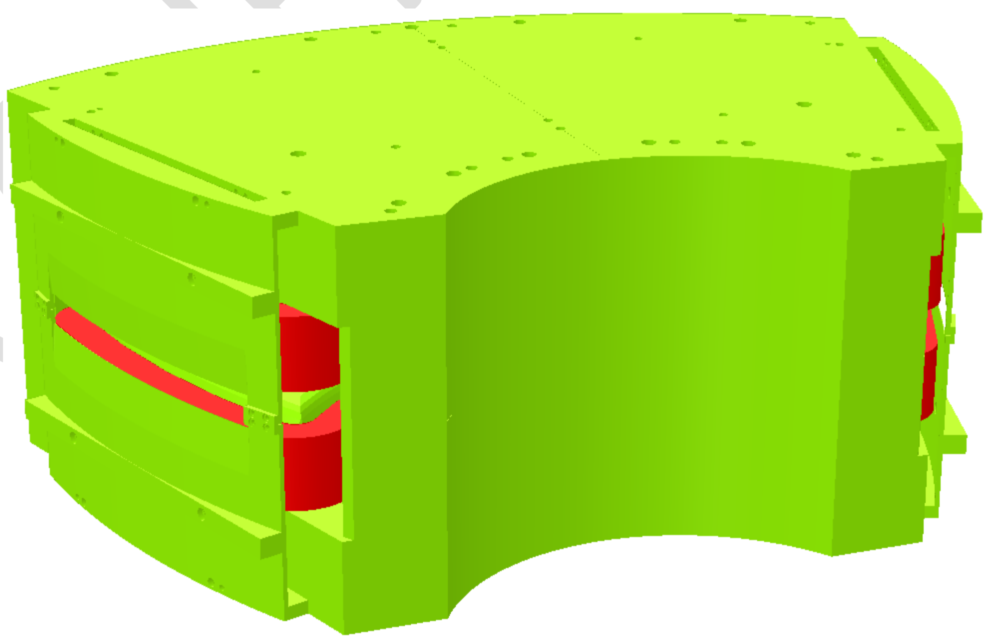

Figure 75: Final engineered design (HRS-120-23C62eng21).

The field flatness of the final engineered design is plotted in Figure 76, while the integral values for the hard-edge case and the OPERA model are listed in Table 12. These values are different with respect to the final design because the coil section is different but the current density is the same. This difference is neither changing the effective field position nor the integral field flatness.

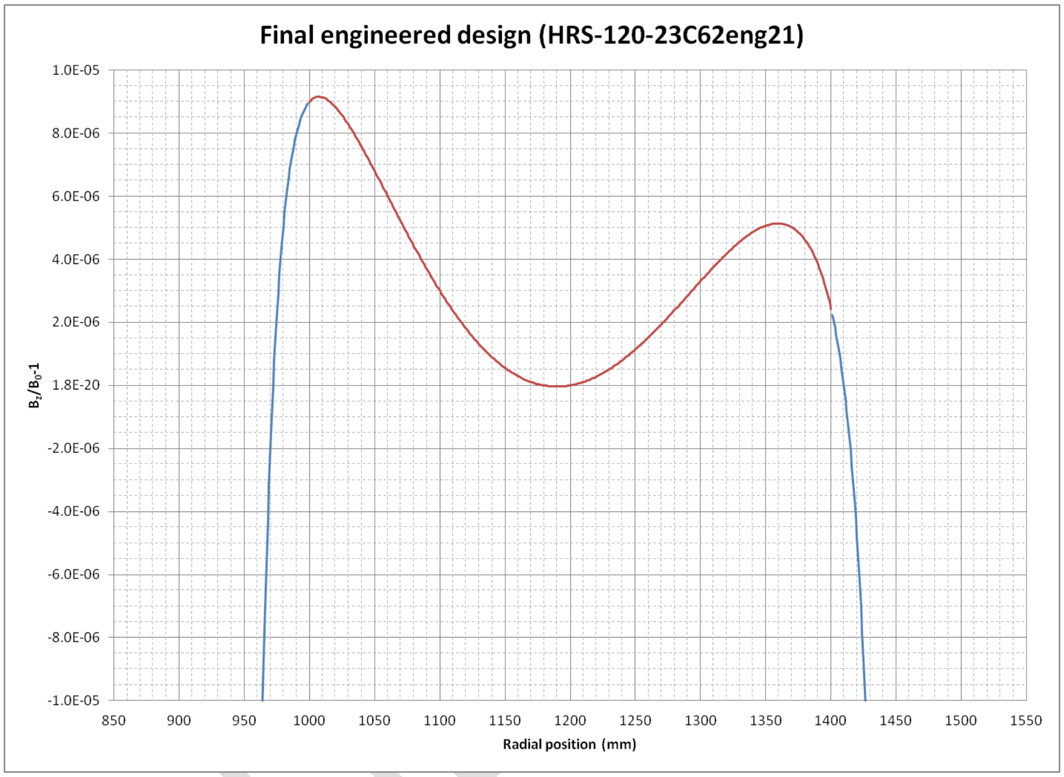

Figure 76: Field flatness of the final engineered design.

Table 12: Field integrals for the Hard Edge and OPERA Models for the Final Engineered Design (HRS-120-23C62eng21)

Geometric trajectory	**Hard-edge integral (T mm)**	**OPERA integral (T mm)**	$IR_\rho - 1$	***Integral flatness***
1000 mm	768.666	768.619	-6.0E-05	-5.8E-05
1050 mm	785.135	785.130	-6.8E-06	-4.1E-06
1100 mm	800.496	800.494	-2.1E-06	6.2E-07
1150 mm	814.736	814.736	8.3E-07	3.5E-06
1200 mm (reference)	827.844	827.842	-2.7E-06	0.0E+00
1250 mm	839.810	839.809	-1.1E-06	1.6E-06
1300 mm	850.623	850.622	-9.1E-07	1.8E-06
1350 mm	860.270	860.268	-3.3E-06	-6.2E-07
1400 mm	868.742	868.738	-5.3E-06	-2.6E-06

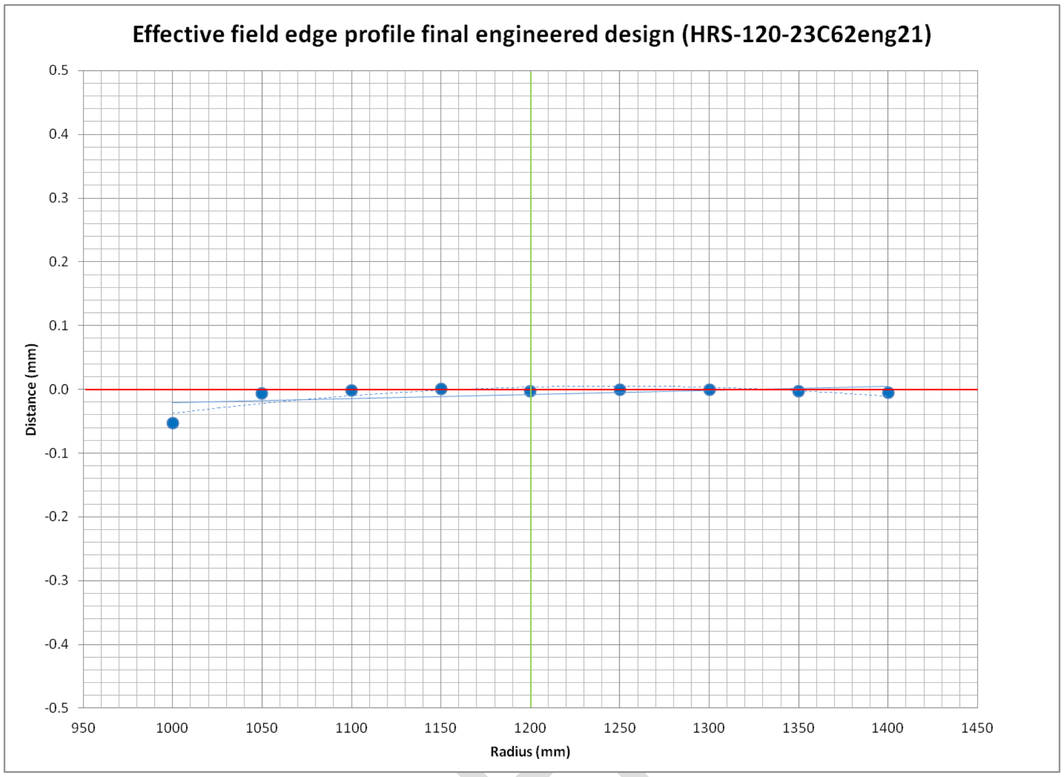

Figure 77: Effective field edge profile for the final engineered design at full excitation.

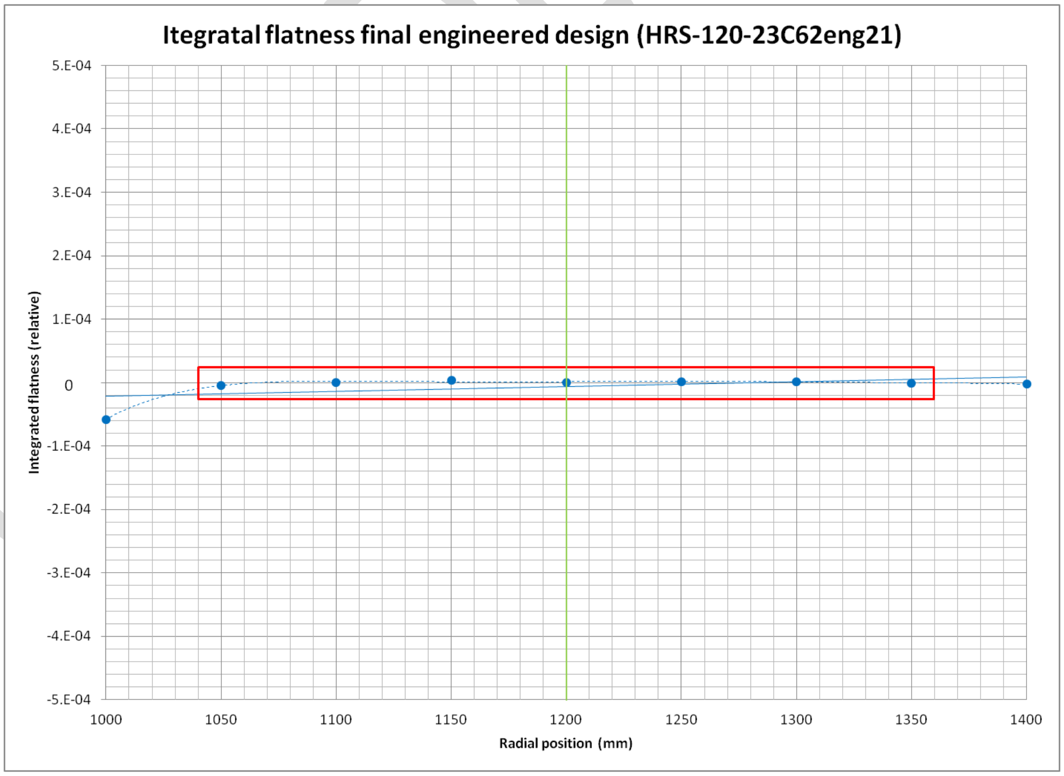

Figure 78: Integral flatness of the final engineered design at full excitation.

11 Magnet Steel and Testing

Quality of the steel used in the magnet poses one of the largest sources of risk in terms of achieving the goals of the HRS design. Furthermore, the optical design is premised on the similarity between the two magnetic dipoles. Substantial discrepancies in the field quality of the magnets individually or in tandem would reduce the ability of the HRS to reach its design goals.

To address these risk factors, the highest and most consistent quality of magnetic steel available should be selected. The most rigorous testing feasible should be employed to avoid inclusions and voids in the steel, particularly in the pole material.

For the dipole magnet's pole and yoke steel we have chosen to use ArcelorMittal USA HP Magnet Plate Steel with Fineline processing to reduce non-metallic inclusions, and with the most stringent ultrasonic examination possible. To increase the similarity between the two dipole magnets, the poles for each magnet should be machined from one plate. Magnet field clamps will be produced from material for the same batch of steel as the rest of the magnet.

12 Power Supplies

In order achieve and maintain its required resolution, high precise and stable power supplies are needed. The highest mass (A=238) particles transmitted in the HRS will experience bending fields within the magnetic dipoles on the order of ~.5 Telsa (~ 5000 G). To maintain resolution of 20000, it is reasonable to estimate that field incremental step on the order of 0.05 G will be needed to tune the HRS, and that the power supply ripple on the order of 10^{-5} or less is necessary for long term stability of the tune. As similar stability level (precision better than 10^{-5} relative to the field) will be necessary for a comparable incremental step size for the lowest mass to be separated at resolution 20,000.

Additionally, it is anticipated that the HRS will be placed on a 60 kV high-voltage platform. This platform will need to be grounded to a stability of < 1 V to maintain the energy spread in the beam.

Two alternative preliminary schematics have been developed for the magnetic dipole power supplies. The first option has a single main power supply connected in series with the two dipoles and one small trim power supply connected in parallel to each dipole. The second option has a main and trim power supply connected in parallel to each dipole. The selected choice (second option) is represented in Appendix B to this note.

CONFIDENTIAL

13 Thermal Stability

Thermal variations with the HRS, particularly at or near the magnetic dipole, also pose a challenge to meeting the spectrometer resolution specifications. For example, changes in coil excitation can result in temperature changes in the nearby steel. This can result in changes in the steel's dimensions and the shape of the magnetic fields. These changes have both a short and long time frame. Rapid changes in coil excitation create prompt changes that can make the HRS difficult to tune. Large variations in temperature over many hours of operation should be avoided to maintain beam tunes within the HRS.

To address this risk, the HRS coil design includes an insulating layer with water flow to act as a heat sink and regulate the heat flow from the coils to the magnetic steel. A preliminary sketch of the coil design has been developed. The water-cooled coils will have an inlet temperature of 30 C controlled to better than +/- 0.25 C. Additionally, the air temperature of the HRS room is expected to be 22 C. Maintaining consistency of this temperature within a limit of better than +/- 2 C has been set as a requirement to help ensure long term stability of the magnetic fields. This may require placing the dipole magnets within a separate tent so that air temperature can be controlled.

14 Diagnostics

Effective beam tuning to meet the resolution goals for the HRS will require extensive diagnostic tools. Studies of existing separators show that this is often a key deficiency that prevents the design goals from being reached. In light of this, the HRS requirements outline certain minimal diagnostics to be included in the HRS to facilitate properly threading the beam through the separator, focusing the beam, and identifying and correcting higher order effects in the beam. These beam diagnostic elements include:

- Faraday cup (FC) for high intensity and a scintillator detector (SCD) for low intensity beam current measurements at the entrance and exit to the HRS.
- Rotating profile monitor to measure beam profile and matching at the entrance and exit to the HRS.
- Allison type with CEM emittance scanner to measure transverse emittance at the entrance and exit to the HRS.
- Collimating slits capable of maintaining a horizontal aperture gap on the order of ~50−100 μm at the entrance and exit to the HRS.
- Waist aperture slits capable of operation from fully closed and opening in ~5 μm steps for setup and conditioning of the beam.

Although these outline a minimal level of diagnostic tools, it could be optimal to include additional emittance scanners and profile monitors at the waist created by the matching/magnification section, and additionally at some point between the magnetic dipoles.

CONFIDENTIAL

Additionally, diagnostics are needed to measure the field within the dipoles. Initially this will be use to tune the beam. Since variations in the field during tuning have a short time scale, Hall probes will provide the measurement of the fields. The controls will also use a feedback loop to help maintain stable and consistent fields from the magnets. For these slower varying measurements, NMR probes will be used. The precision of these probes will need to be of order of 0.05 G or less since the dipole fields will need to be maintained to an accuracy of 10^{-5}. A coil to measure flux through the entire magnet may also be a possible diagnostic used.

15 Vacuum Chamber Design

To avoid interference with the optical design cause by stray magnetic fields, the vacuum chamber for the HRS will be made from non-magnetic material.

A preliminary design for the vacuum chambers within the dipole magnet has been developed. It will be manufactured from aluminum and designed to maintain vacuum of 10^{-7} Torr or better.

A preliminary design for the magnetic dipole vacuum chambers has been developed and is attached to this note as an Appendix. The vacuum chambers for the remaining HRS beam line and matching/magnification sections will be based on TRIUMF standard designs.

16 Multipole Corrector Design

The HRS utilizes an electrostatic multipole corrector to compensate for aberrations uncorrected by the dipole edge shaping. This element is centered at the geometric midpoint of the HRS to allow full mirror symmetry of the separator. Originally this element was simulated in COSY using idealized multipole fields through 5th order (duodecapole) and COSY's basic fringe field models. Based on an element length of 30 cm and an aperture of 10 cm from the optical axis to the poletips, the poletip potentials were determined, and have previously been list in Table 2.

For more accurate simulation, the corrector has also been modeled in OPERA. The basic design is inspired by the corrector used in the CARIBU system at Argonne National Laboratory. As shown in Figure 79, the corrector consists of 24 cylindrical poletips places symmetrically around a larger, grounded cylindrical support, and separated by a non-conducting insulator. Voltages are independently applied to the 24 poletips to create the desired multipole fields. 24 poletips were chosen because this allows for creation of geometrically "pure" multipoles at 2nd (sextupole), 3rd (octupole) and 5th (duodecapole) order.

CONFIDENTIAL

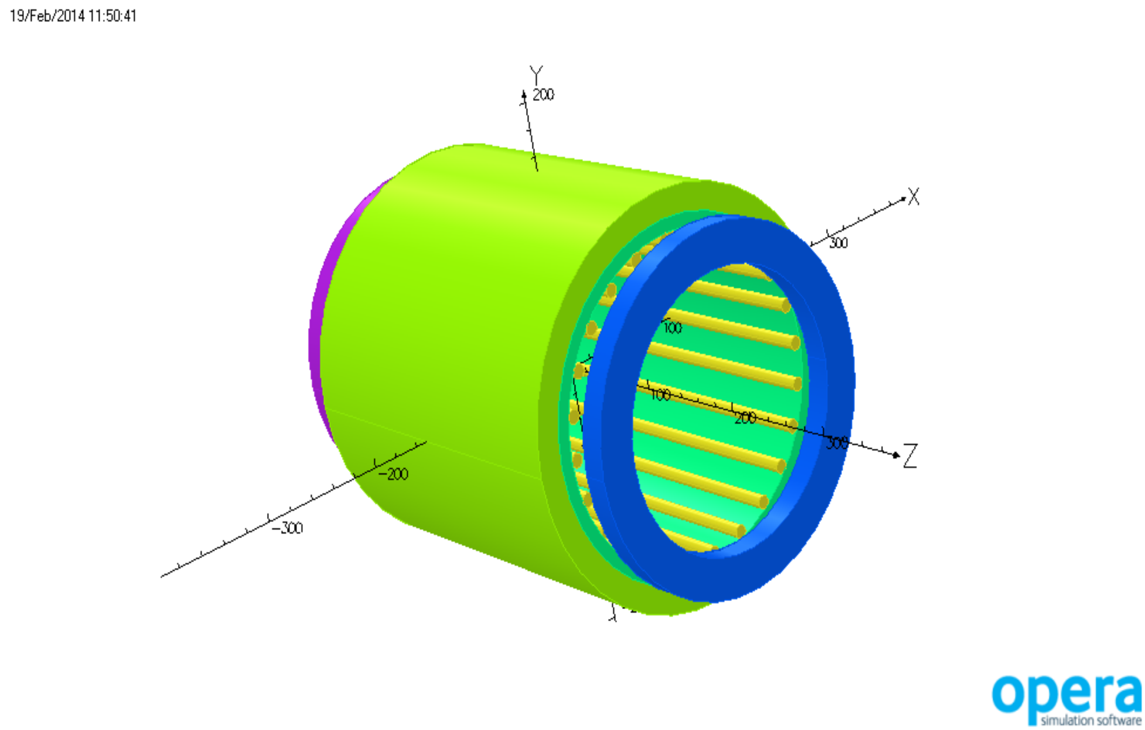

Figure 79: OPERA model of the HRS Electrostatic multipole corrector.

Grounded “shunts” are used to minimize the length of fringe fields outside the element [5]. The effect of adding these shunts is shown in Figure 80 and Figure 81. In this plots, the horizontal and longitudinal components of the electrostatic field are measured along a line offset horizontally by 7.5 cm from the optical axis from a location outside the entrance to the HRS multipole corrector through the center of the element.

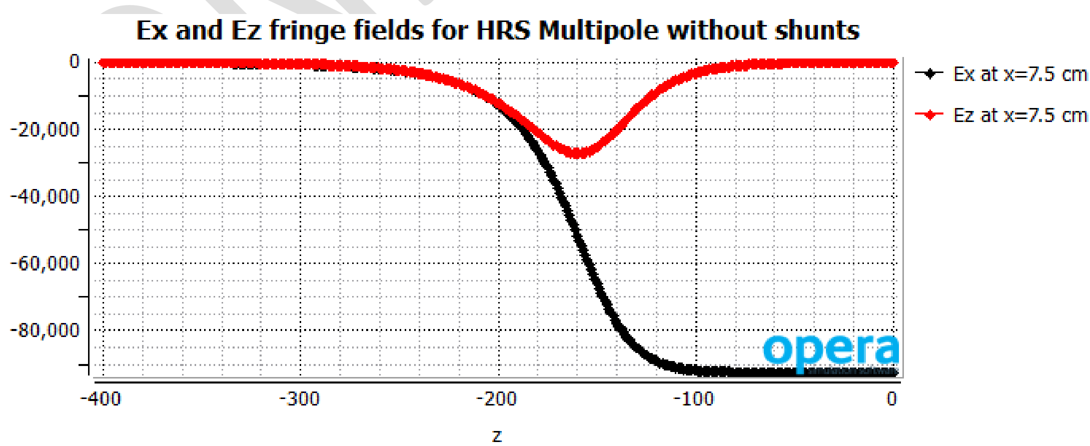

Figure 80: OPERA model of electrostatic field vector components Ex and Ez for the entrance fringe field of the HRS multipole corrector. The entrance edge of the element is at z = - 150 mm. z = 0 represents the center of the HRS multipole corrector. Field components are given along a line in the x-z midplane and offset from the optical axis horizontally by 7.5 cm.

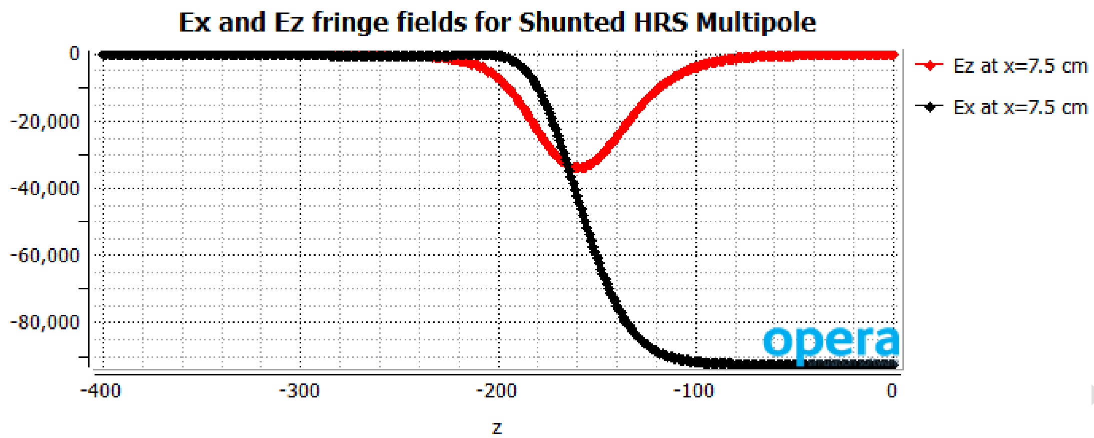

Figure 81: OPERA model of the electrostatic field vector components Ex and Ez for the entrance fringe field of the HRS multipole corrector. The entrance edge of the element is at z = - 150 mm. Grounded "shunts" have been added z = -170 mm. z = 0 represents the center of the HRS multipole corrector. Field components are given along a line in the x-z midplane and offset from the optical axis horizontally by 7.5 cm.

This OPERA model has been used to generate data for the fields and potentials, including the fringe field regions. Figure 82 shows an example plotting data points for the electrostatic potential (Volts) in the x-z midplane from the center of the corrector (z=0) through the fringe field region outside the element. That data is then used in COSY to simulate the OPERA design of the element, including non-linearities created by actual design geometry and shunted fields [6]. This will allow for more precise study of the HRS design, particularly the nonlinear dynamics that can be determined from the COSY simulations.

CONFIDENTIAL

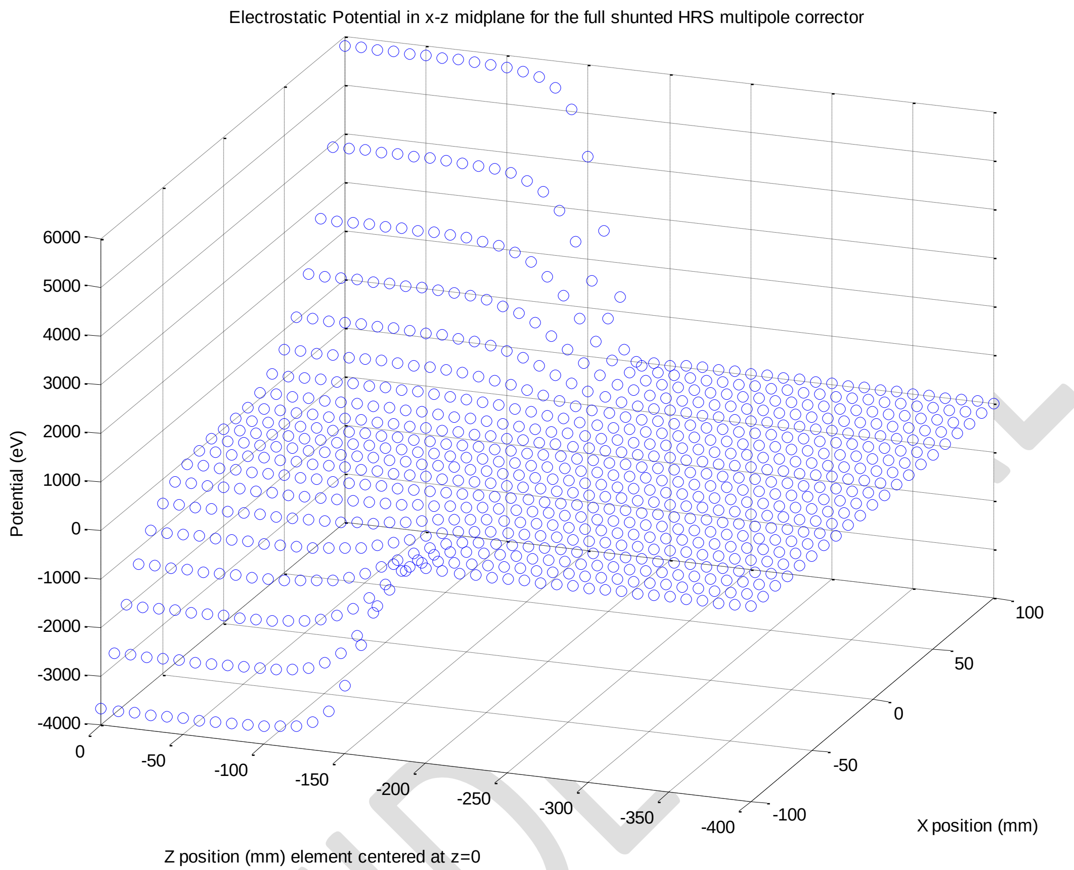

Figure 82: Modelling of the electrostatic potential in the x-z midplane for the HRS multipole corrector from the entrance fringe field region through the center of the element (z = 0) based on data determined from OPERA model of the corrector.

CONFIDENTIAL

17 Works Cited

[1] K. Makino, M. Berz, "COSY Infinity Version 9," Nuclear Instruments and Methods A558 (2005) 346-350, 2005.

[2] M. Marchetto, "ARIEL High Resolution Spectrometer First Order Calculation," TRIUMF Design Note TRI-DN-13-07, TRIUMF Document-74265.

[3] M. Marchetto, "ARIEL High resolution Spectrometer Requirements," TRIUMF Document-74319.

[4] J. Maloney, "Studies of Magnetic Dipole Edge Shaping," TRIUMF Beam Physics Note, April 2014.

[5] H. Wollnick, "Optics of Charged Particles," Accademic Press, 1987.

[6] J. Maloney, "New Electrostatic Element Procedures for COSY Infinity," TRIUMF Bam Physics Note, March 2014.

[7] M. Berz, Advances in Imaging and Electron Physics Vol. 108 (1999) pp. 212-13.

CONFIDENTIAL

Appendix A: Preliminary Dipole Magnet Vacuum Chamber Schematic. The assembled dipole is shown inside the hatch the leads to the HRS underground room.

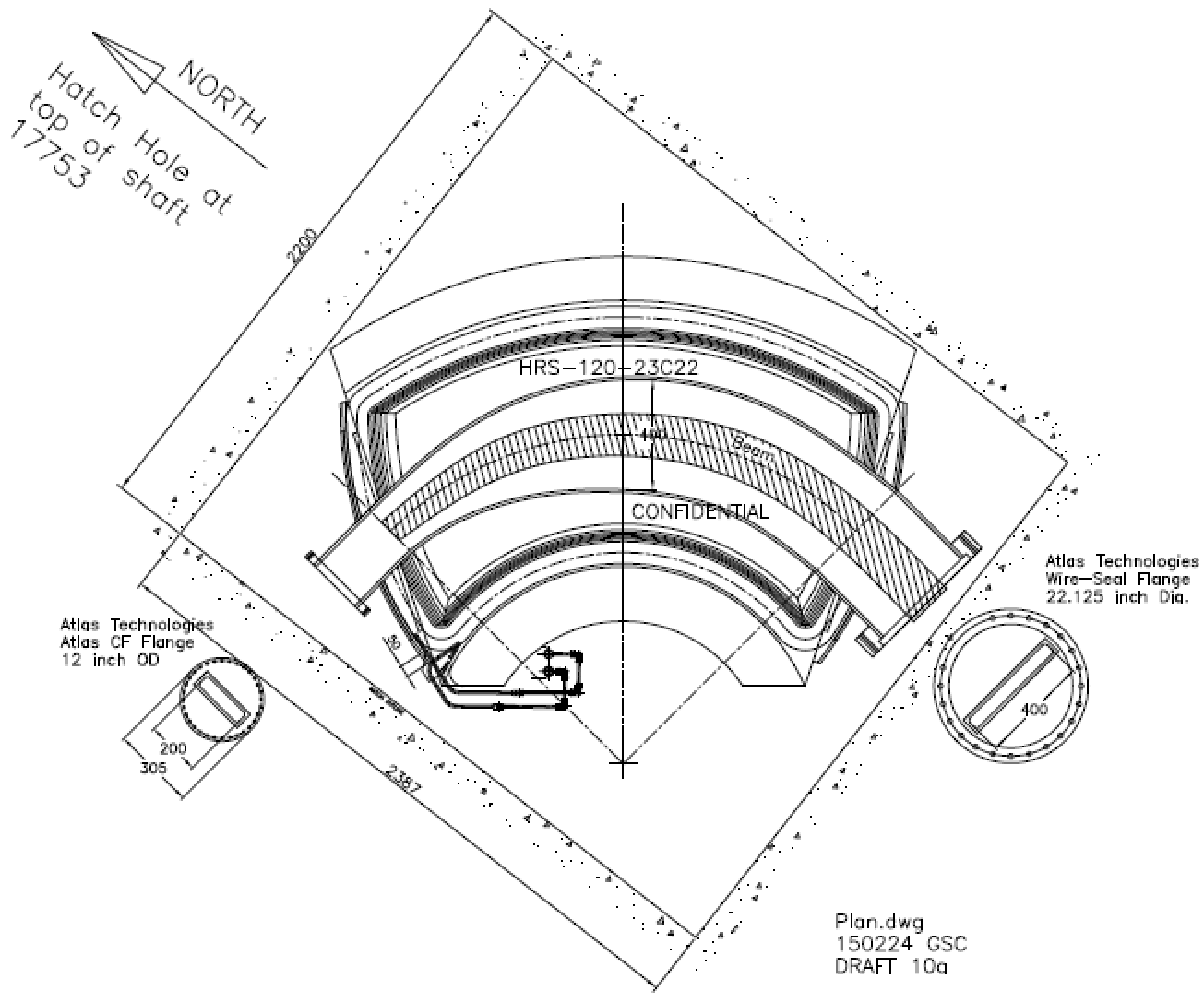

Appendix B: Dipole magnet power supply configurations. Each magnet will be powered by a main power supply (200 A 50 V) in parallel with a trim power supply that controls the magnetic field.

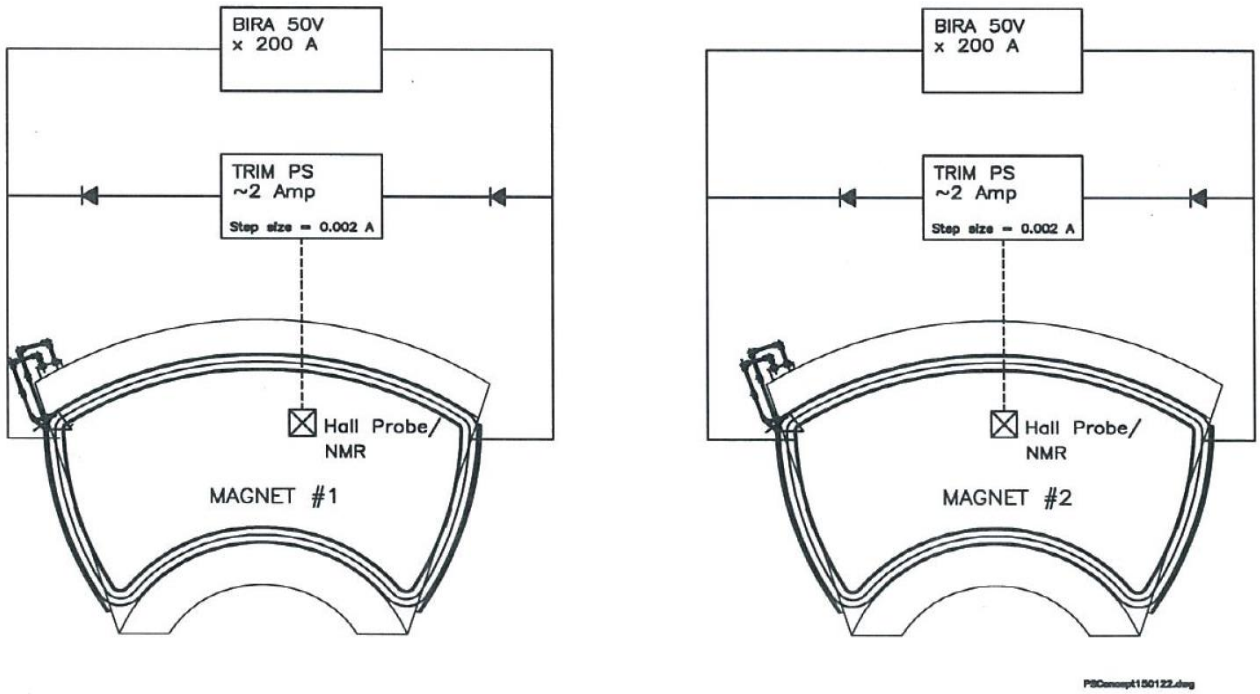

Appendix C: Coil design with cooling layer and sense coil.

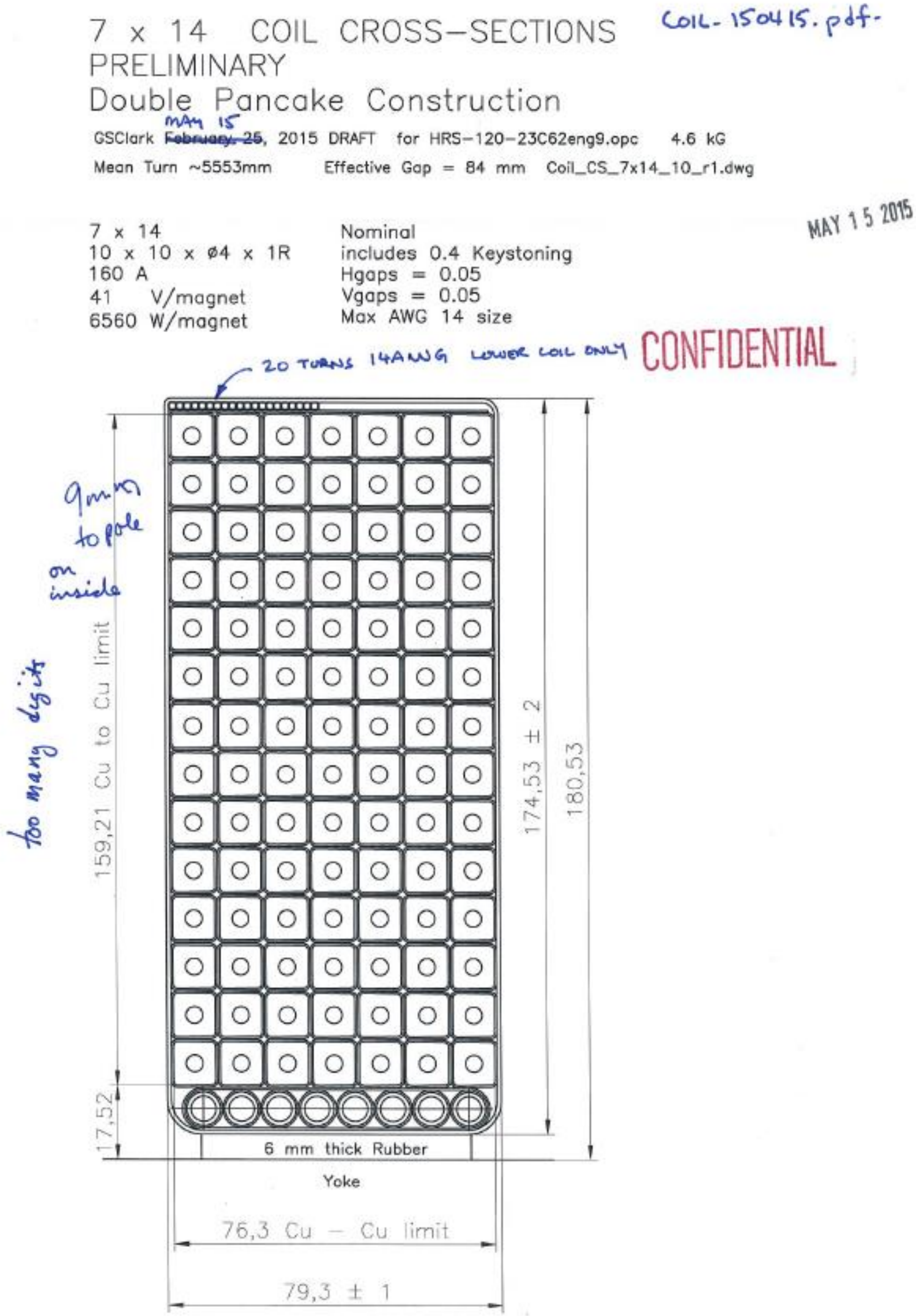

Appendix D: Pole mount: bolts, dowel and spacers.

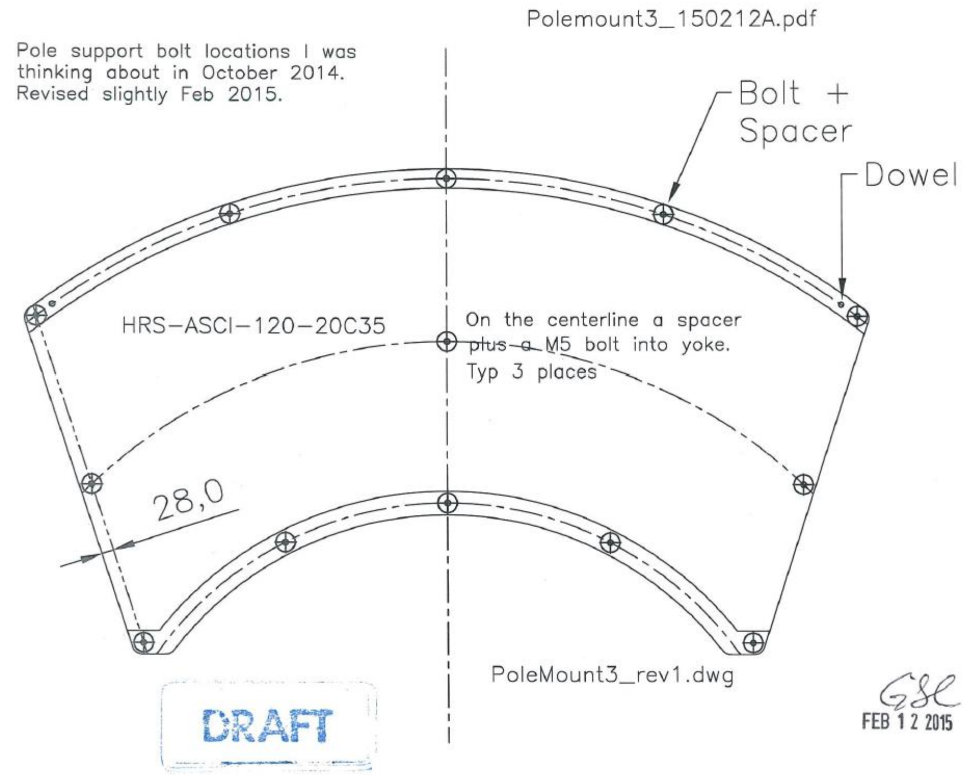

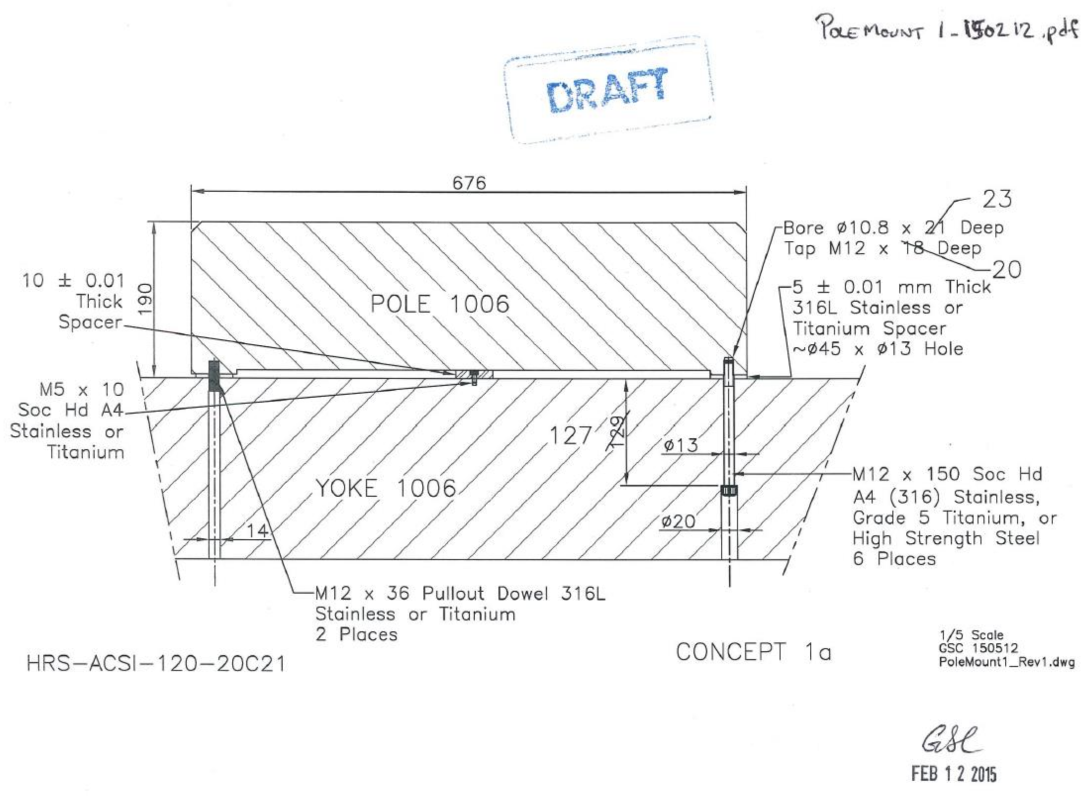

Appendix E: Pole holes for alignment and mapping.

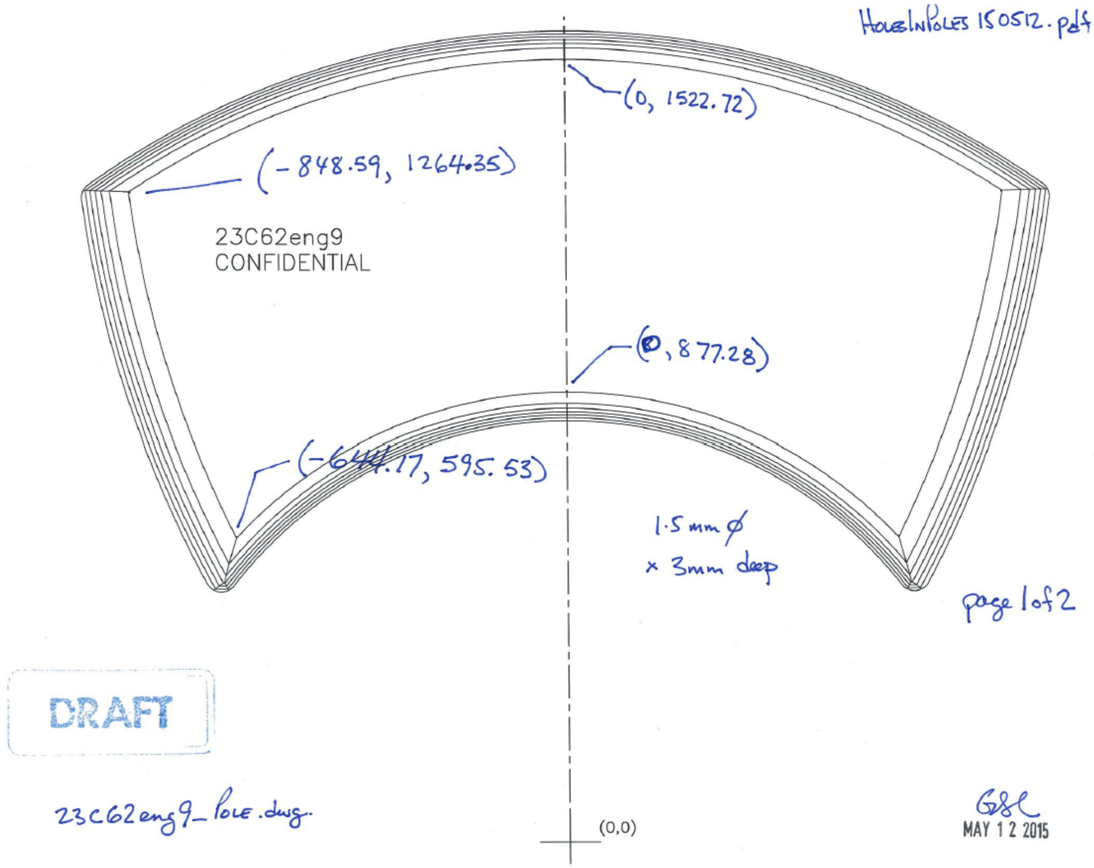

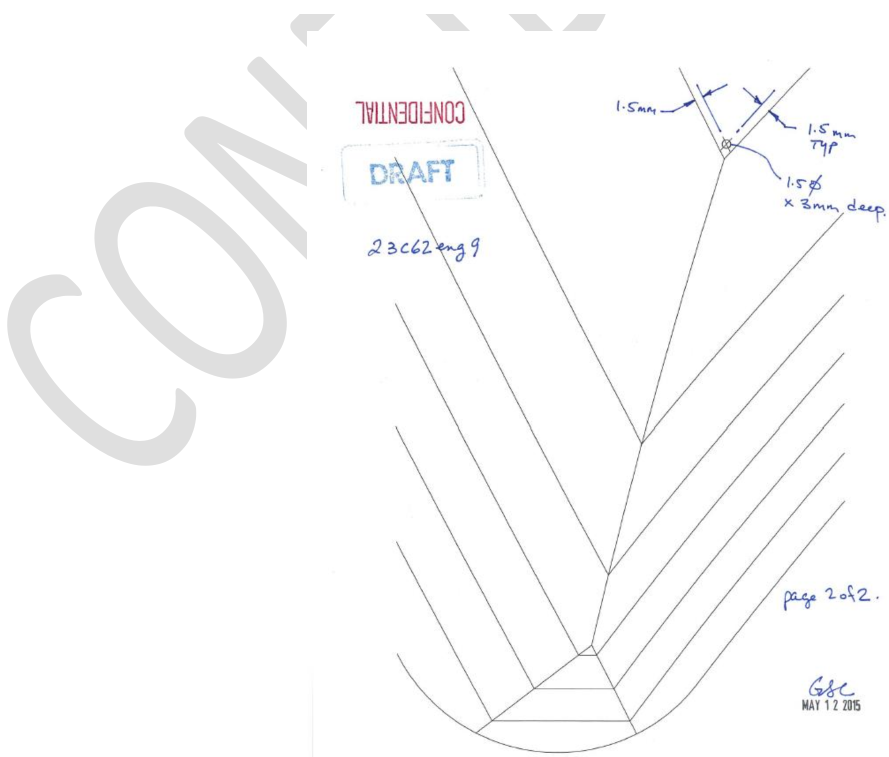

Appendix F: Yoke mount: bolts and dowels.

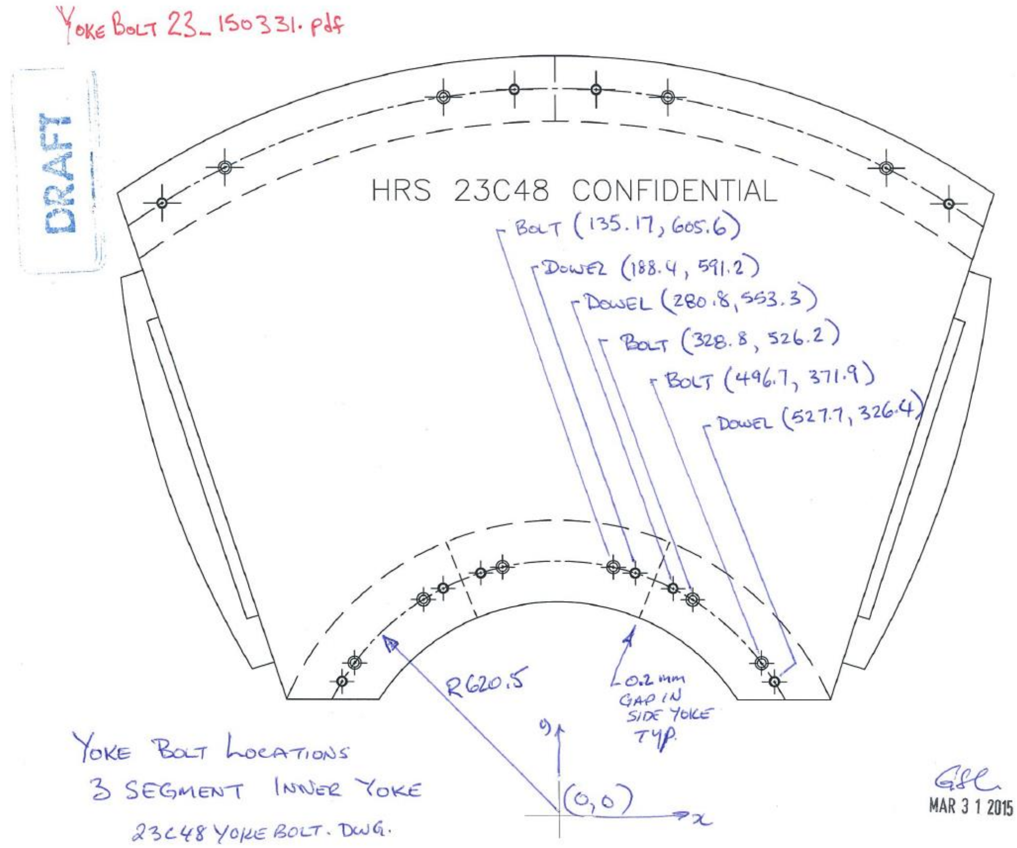

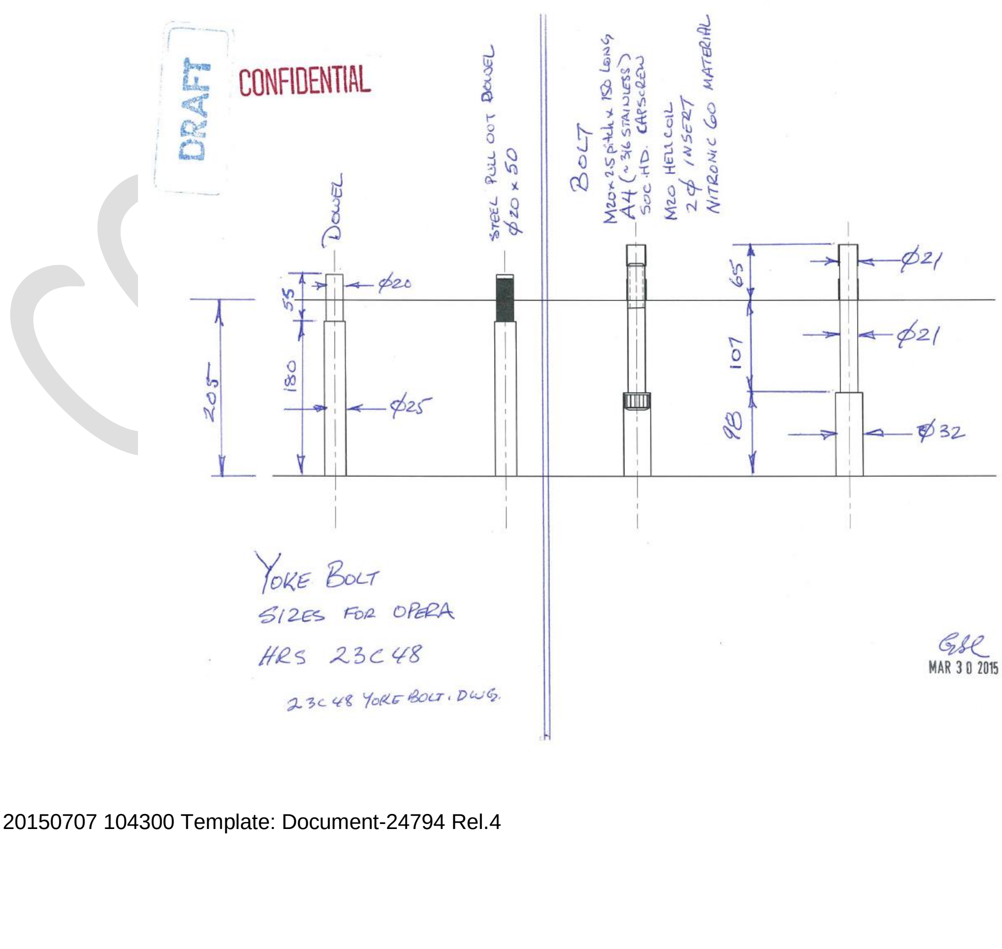

Appendix G: Thermowells.

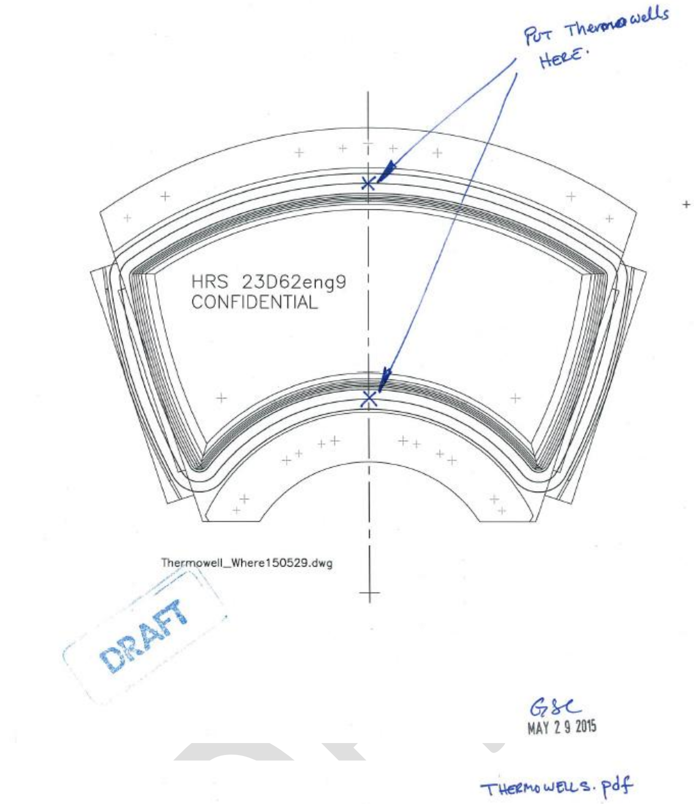

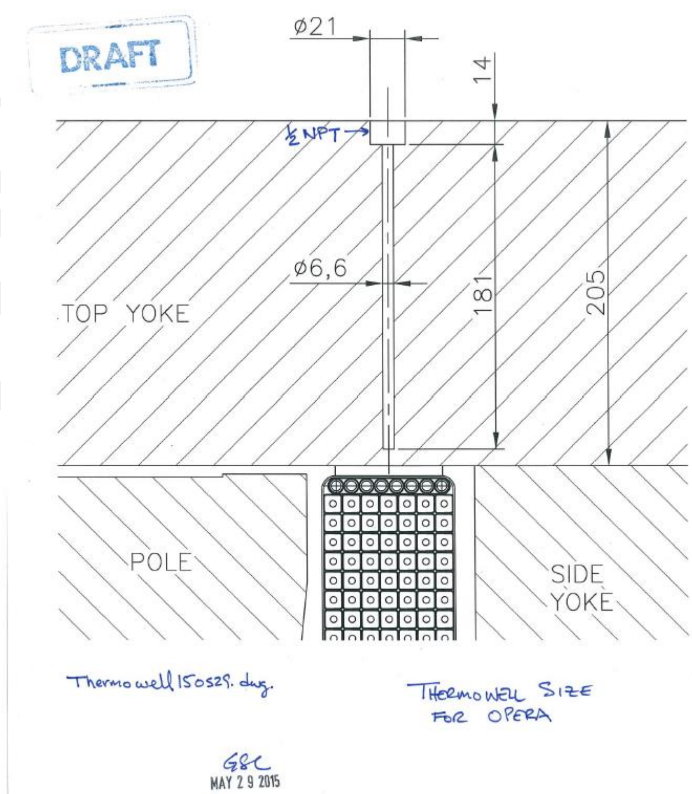

Appendix H: Hoist rings: lifting holes.

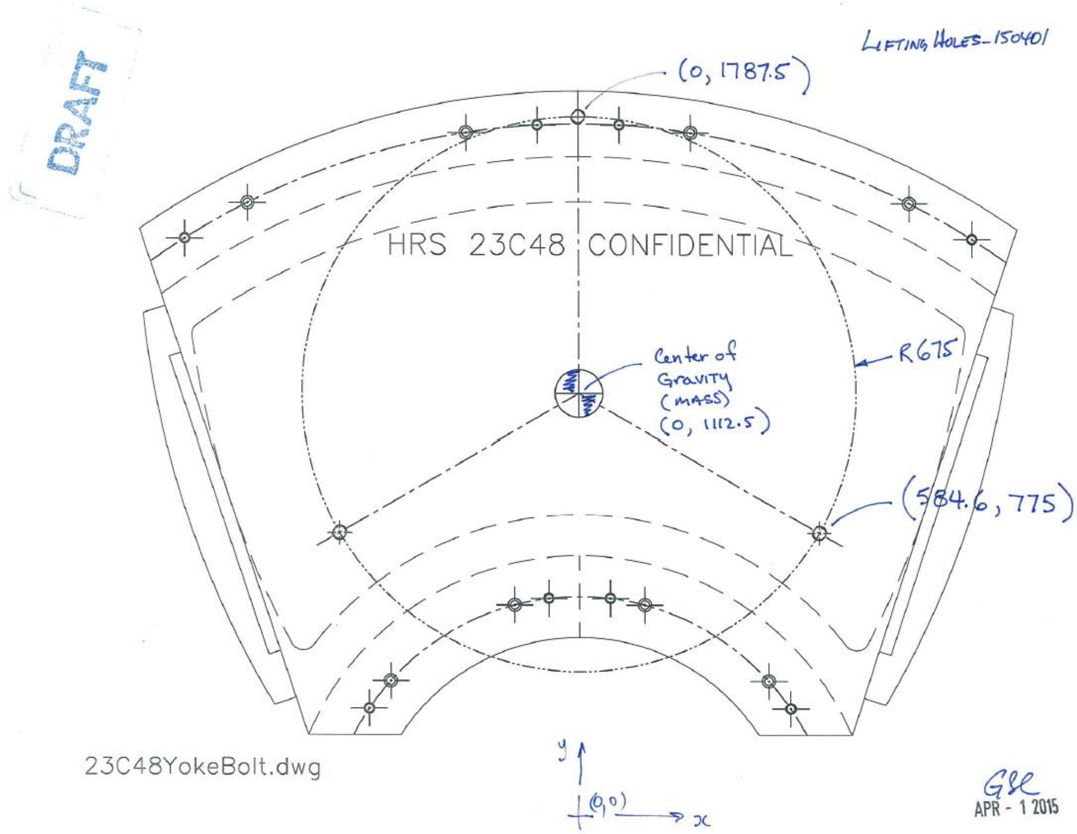

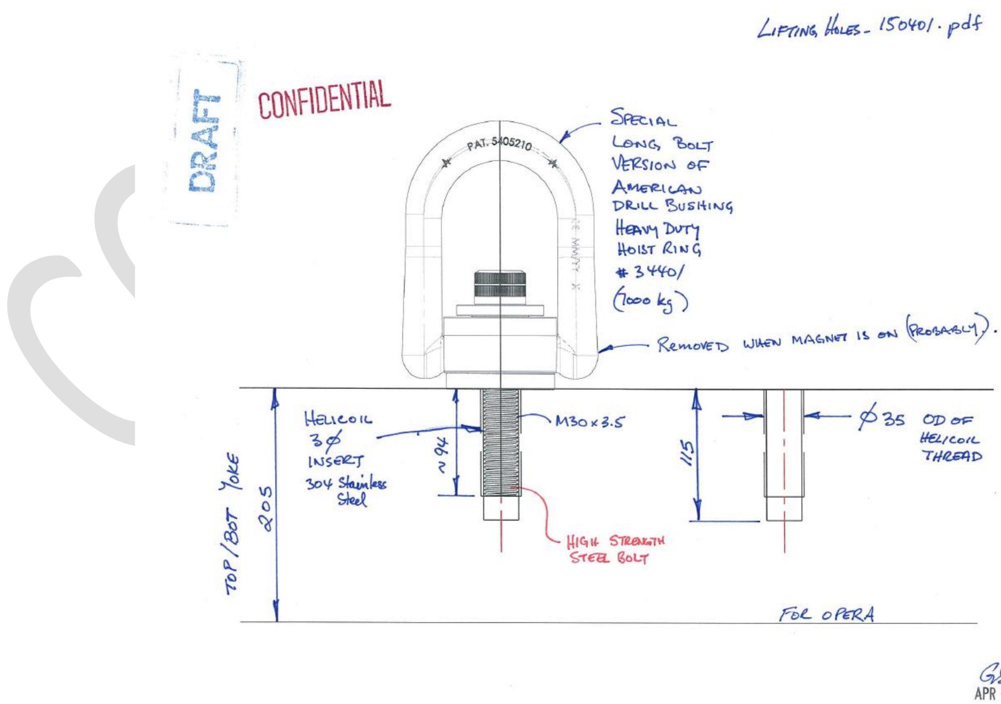

Appendix I: Field clamp mount, bolts and dowel, and squared at the bottom.

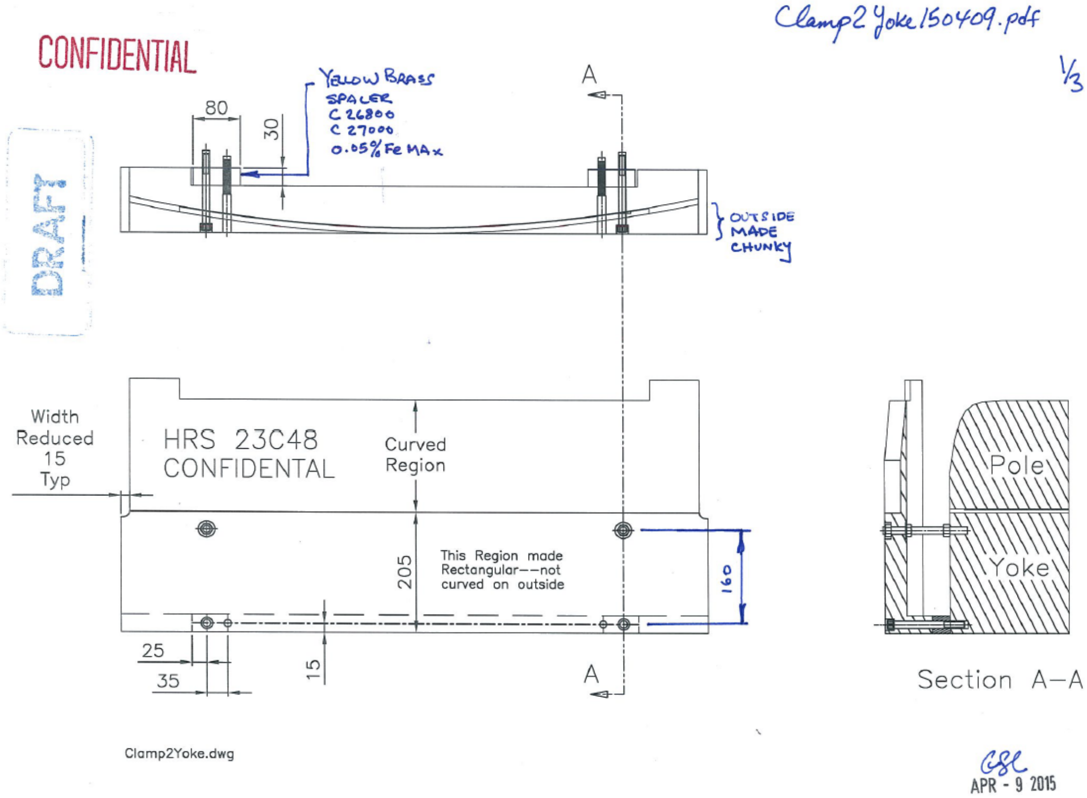

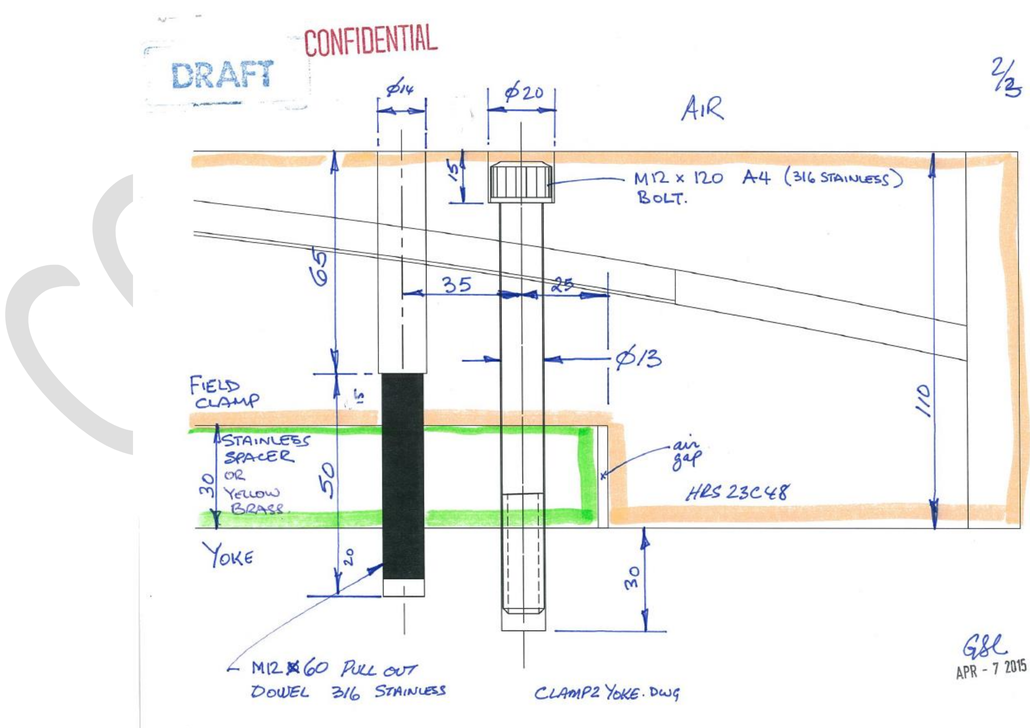

Appendix J: Internal yoke chamfer and reduced field clamp width to accommodate the coil tail.

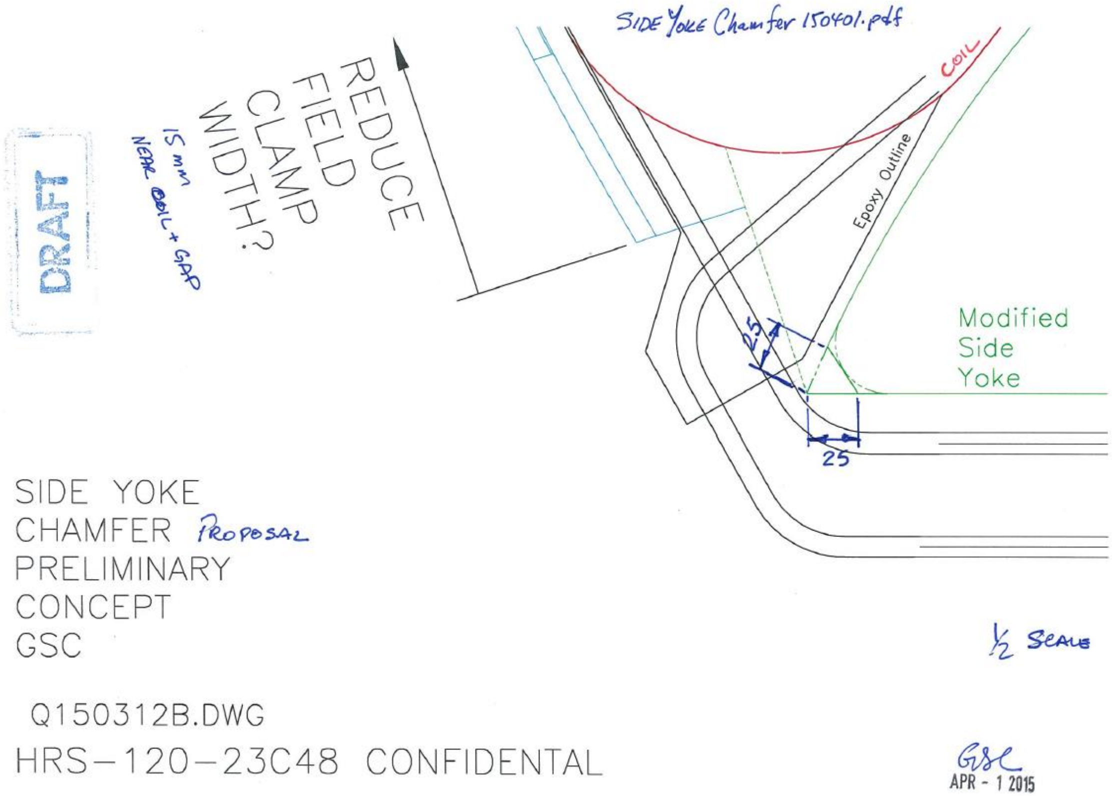

CONF

Appendix K: Field clamp connections

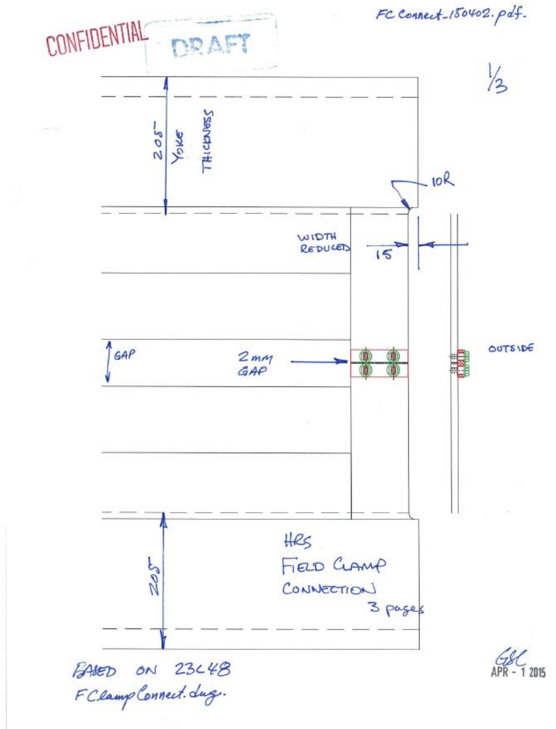

Appendix L: Beam Envelope Calculations

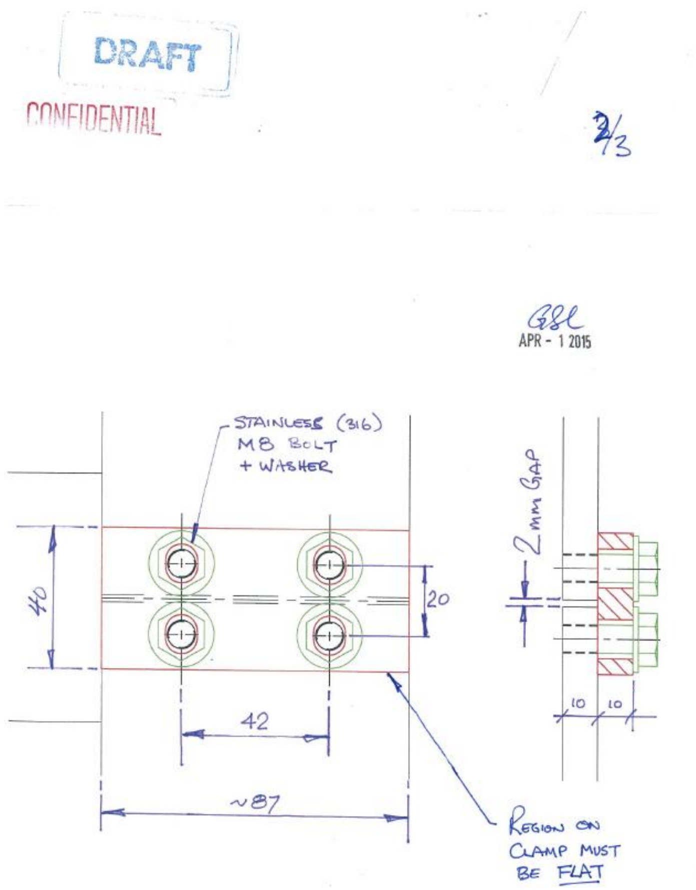

Estimated beam envelope for reference mass and energy along the pure separator portion of the HRS (assume initial beam with 3 pi μm horizontal emittance (.05 mm x 60 mrad) and 6 pi μm vertical emittance (2 mm x 3 mrad):

	Entrance 1st Dipole	Exit 1st Dipole	Entrance Multipole Corrector	Exit Multipole Corrector	Entrance 2nd Dipole	Exit 2nd Dipole
Horizontal Size (mm)	48 cm	96 cm	96 cm	96 cm	96 cm	48 cm
Vertical Size (mm)	3.1 mm	6.3 mm	5.7 mm	5.5 mm	6.3 mm	3.1 mm